Friedrich-Schiller-University Jena
Institute of Geography
Department of Geographic Information Science

Modeling the Spatial Distribution of Hail Damage in Pine Plantations of Northern Spain as a Major Risk Factor for Forest Disease

A thesis presented to the University of Jena in fulfillment of the thesis requirement
for the degree of *MASTER OF SCIENCE* in Geoinformatics.

presented by
Patrick Schratz

First supervisor:	Prof. Alexander Brenning
Second supervisor:	Dr. Jannes Münchow

Jena, Thuringia, Germany, 2016

Friedrich-Schiller-Universität Jena

> “*Conducting data analysis is like drinking a fine wine. It is important to swirl and sniff the wine, to unpack the complex bouquet and to appreciate the experience. Gulping the wine doesn’t work.*”
>
> Daniel B. Wright, *2003*

DECLARATION

I hereby testify that I have written the whole of this thesis myself and used no sources or aids (including electronic media and online sources) other than those named. All passages taken from a source, whether verbatim or in substance, have been indicated as such.

ACKNOWLEDGEMENT

After intensive six months, today is the day: writing this note of thanks is the finishing touch on my thesis. It has been a period of intense learning for me, not only in science, but also on a personal level. Writing this thesis had a big impact on me. I would like to reflect on the people who supported and helped me so much throughout this time.

I would first like to thank my supervisors, namely Alexander Brenning and Jannes Muenchow. You both supported me greatly and were always willing to help me. Beside your excellent book recommendations, I want to say thank you for your fast replies and especially for the hours you spent with me discussing the concept, the current problems and for sharing your motivation in the field of (geo)statistics with me! A special thanks for providing such excellent working conditions during these months. This fact certainly had a big impact on this work!

Thanks to Marie and Hendrik who spent hours optimizing my English without being afraid of facing advanced statistical topics. Your involvement is highly appreciated!

I would especially like to thank my parents for providing me the opportunity to always come home and take some time off when I needed to recharge my batteries. Thanks for your warmhearted support during the last five years of my studies. This work is dedicated to you, Mom & Dad! *[Ich möchte vor allem meinen Eltern Danke sagen, die mir jederzeit die Möglichkeit gegeben haben, nach Hause zu kommen und meine Batterien wieder neu aufzuladen. Danke für eure warmherzige Unterstützung mein ganzes Studium über! Diese Arbeit ist euch gewidmet, Mama & Papa!]*

Thank you Mecki for all the challenges we faced throughout our studies and at all places we have been together around this world! My studies will always be associated with you. Thank you for just being yourself. I could not have wished for a better classmate/friend!

Thanks to all my friends in Jena and at home for your understanding of my dedication to this work and for sometimes having to say "I am sorry, I have no time right now, we have to postpone our plans". The next one is on me ;)

Patrick Schratz
Jena, September 2016.

ABSTRACT

Hail storms are able to cause severe damages to all kind of goods. While mostly economic damages of hail events are considered, damages to vegetation are more complex to quantify due to their complexity and hetereogenity regarding species and types. Few research exists on this topic which relies on the complexity of hail as a phenomenon itself: Due to its small-scale characteristics only few in situ measurement systems exist, making it problematic to gather long time series of reliable data. Furthermore, almost no research has been done undertaken yet on the follow-up effects of hail damage to plants. This work aims to contribute to this science field by analyzing the spatial distribution of hail damages in pine plantations in northern Spain.

For this purpose, binomial statistical learning methods (Generalized Linear Mixed Model (GLMM) and Generalized Additive Mixed Model (GAMM)) were applied to surveyed "hail damage to trees" distributed across the Basque Country. Climate variables like precipitation, temperature and Potential Incoming Solar Radiation (PISR), extracted from a long term climate data set with a spatial resolution of 200 m, were used as predictors in the models to explore the relationship between them and the response. Age of the surveyed trees was used as a biological component in the model. Underlying grouping structures (spatial autocorrelation and random effects) in the data were investigated and accounted for in the models. Additionally, the synoptic weather situation of hail occurence was analyzed using long term weather station data for the cities Bilbao, San Sebastian and Vitoria.

The prime time for hail occurence was found to be between November and April. The analysis of the weather station data revealed non-linear relationships between hail occurence and climatic variables. The GAMM, accounting for the underlying spatial autocorrelation, did not converge. Hence, these results have to be treated with caution due to a violation of the independence assumption of the residuals. Different risk areas were carried out with the result of the northeast of the Basque Country being most susceptible of "hail damage to trees" (for both models). A considerably decrease of "hail damage to trees" susceptibility was observed along the Cantabrian Range with very low estimated probabilities of "hail damage to trees" for areas located further south. This finding runs contrary to the absolute occurence of hail events which is highest in areas with estimated low probabilities, inferring that most of the hail events in this region happen with a low destructive energy. A substantial increase of "hail damage to trees" probability was observed in the Generalized Additive Model (GAM) for the top third range of the predictor range of precipitation and minimum temperature with examplary odds ratios of 7.9 (0.125 m/mm^2 - 0.14 m/mm^2) and 3.99 (5°C - 6°C), respectively. Estimated probabilities range between 0%-50% for the GLMM and 0%-100% for the GAM. The latter revealed high uncertainties in areas with low precipitation and/or temperature values pointing to a likely overfitting of the model which is also confirmed by the large gap between the (100 repetitions, ten fold) spatial cross-validation result of the training set (0.87) and the test set (0.62).

Further research using more environmental variables explaining hail occurence (e.g. wind speed) is suggested. Also, the outcomes of this work (risk areas, estimated probabilities) need to be compared to analyses using direct hail observations (in contrast to derivated observations like in this work) in the Basque Country.

TABLE OF CONTENTS

LIST OF FIGURES

LIST OF TABLES

LIST OF APPENDICES

LIST OF ACRONYMS

AIAG	International Association of Agricultural Production Insurers
AIC	Akaike Information Criterion
ANELFA	Association Nationale d'Etude et de Lutte contre les Fléaux Atmosphériques
AMSR-E	Advanced Microwave Scanning Radiometer-EOS
AUROC	Area Under the Receiver Operating Characteristic Curve
CAPE	Convective Available Potential Energy
CAPPI	Constant Altitude Plan-Position Indicator
CCN	Cloud Condensation Nuclei
CI	Confidence Interval
CV	Cross-Validation
DEM	Digital Elevation Model
ESWD	European Severe Weather Database
GAM	Generalized Additive Model
GAMM	Generalized Additive Mixed Model
GLM	Generalized Linear Model
GLMM	Generalized Linear Mixed Model

GSC	Geoscience Consultants
GSOD	Global Summary of [the] Day
IN	Ice-forming Nuclei
IPCC	Intergovernmental Panel on Climate Change
IQR	Interquartile Range
LiDAR	Light Detection and Ranging
LM	Linear Model
LOESS	Locally Weighted Scatterplot Smoothing
LOOCV	Leave-One-Out Cross-Validation
MCS	Mesoscale Convective Systems
MESHS	Maximum Expected Severe Hail Size
NCDC	National Climate Data Center
NEXRAD	Next-Generation Radar
OR	Odds Ratio
OT	Overshooting Cloud Tops
PCA	Principal Component Analysis
PISR	Potential Incoming Solar Radiation
POH	Probability of Hail
POSH	Probability of Severe Hail
PPI	Plan-Position Indicator
RMSE	Root Mean Square Error
ROC	Receiver Operating Characteristic Curve
SHI	Severe Hail Index
SI	Site Index
SYNOP	Synoptic Weather Stations
TORRO	Tornado and Storm Research Organization
TPRS	Thin Plate Regression Splines
TSD	Tree Survey Dataset
WMO	World Meteorological Organization
VIF	Variance Inflation Factor
VIL	Vertically Integrated Liquid

CHAPTER 1

INTRODUCTION

The phenomenon hail causes not only serious damage to material goods such as buildings or automobiles but also to natural ones like crops or forest stands (Punge & Kunz, 2016). Hailstorms occur all over the world and their dynamics are very hard to understand due to their small-scale appearance and high variability in both spatial and temporal aspects (García-Ortega et al., 2014; Sánchez, López, García-Ortega, & Gil, 2013; J. Webb, Elsom, & Meaden, 2009). According to Vinet (2001) more than 150 million Euros related to hail damage were paid to policyholders by insurance companies in 1997 in Spain and France, respectively, not including crop and forest damages. Mallafré, Ribas, del Carmen Llasat Botija, and Sánchez (2009) assume up to 700 million Euros of loss due to hail in the agrarian sector in Spain per year. Only summer hail is capable of damaging crops in most parts of Europe, since before May crops are not yet affected by hail and in October most yield has already been stored (Vinet, 2001). Looking at hail events on a global scale, a hailstorm in Buenos Aires caused damages up to 15 million US dollars in 2010, mostly damaging cars. Moreover, agrarian losses of US$ 50 million and US$ 30 million (wine and fruit production, respectively) on average per year are reported from the western part of Argentina (Mezher, Doyle, & Barros, 2012). Analyzing data from the International Association of Agricultural Production Insurers (AIAG) (formerly known as the 'International Association of Hail Insurers'), Spain has been declared as the country facing the highest losses related to hail damage every year. It is assumed that the damage exceeds 150 million Euros for Spain in total whereat 20 - 30 million Euros are assigned to the Northeastern part of the Iberian Peninsula (Sánchez et al., 2013). Yet damage cost estimations related to hail differ greatly. With respect to Mallafré et al. (2009), 650 - 700 million Euros of costs in the agrarian sector of Spain are related to hail damage. However, the authors did not provide a temporal reference period for this estimation. As cited by Punge and Kunz (2016), Porras, Sairouni, and Aran (2013) estimated the annual loss in the Spanish agrarian sector to be around 240 million Euros for the years 2001 - 2009.

Damages related to hailstorms depend on two fundamental points: Kinetic energy of precipitation and maximum hailstone size (Sánchez et al., 2013; Hohl, Schiesser, & Aller, 2002). Applying atmospheric theories of hail storm genesis, an increase in the surface temperature leads to a growth in uplift power which results in more severe hail intensity (Dessens, 1995). Severe convection can be described as a vertical transfer of heat and humidity coupled with buoyancy. This causes several weather phenomena like tornadoes, hail, strong precipitation or intense winds (García-Ortega et al., 2014). On the other hand, this uplift also favors hailstone melting in the atmosphere and in turn lower hail severity (B. Xie, Zhang, & Wang, 2008). Taking these two opponent effects into account, the final net impact of hailstorms is assumed to rely highly on regional attributes (Dessens, Berthet, & Sanchez, 2015). Thunderstorms containing hail are by experience "highly-organized convective systems in terms of multicells, Mesoscale Convective Systems (MCS), or supercells" (Punge & Kunz, 2016). Topography is one of the key drivers of hail genesis as it controls heat transport and induces convection. However, its influence is often neglected in hail analysis (Changnon, Changnon, & Steven, 2009; Suwala & Bednorz, 2013).

With hail being a rare phenomenon, data availability and quality on hailstorm characteristics such as frequency and severity varies greatly. With the existence of only a few thousand hailstorm occurrences per year in Europe, "an average frequency of much less than one hail event per year at any location" is observed (Punge & Kunz, 2016). Studies by Changnon (1970, 1977) have investigated large numbers of hail-streaks in the U.S. The result was that

80% of all observed cases affected areas with a spatial extent of less than 40 km² while the median was even smaller (20.5 km²). A detailed understanding of the local landscape characteristics is needed to apprehend the non-trivial connection of multiple processes causing the formation of thunderstorms and hail. These processes can be used to infer possible explanations of the spatial variability of hail frequency (Punge & Kunz, 2016). This spatial property of hail can be adopted to Europe as well.

A number of points exist why more knowledge on hail attributes such as frequency, intensity and caused damage is highly asked for. In meteorology, information on hail leads to a better understanding of atmospheric processes leading to hail genesis and this in turn improves the overall insight of atmospheric processes. Geographers investigate the leverage of local-scale features and properties affecting hail genesis. In the economy it is important to estimate hail risk as precisely as possible to provide specific insurance offers for different locations. Some construction techniques (e.g. solar thermal systems) may need to be adapted in certain regions with a high hail severity to ensure resistance. People owning crops or vineyards often rely on long term hail information when deciding whether or not to invest in protection systems or even hail suppression methods (Punge & Kunz, 2016).

Hail analysis is often limited to certain areas due to a lack of widely distributed and standardized observing systems. Since it is uncommon to install hail monitoring devices at Synoptic Weather Stations (SYNOP), hail events are only tracked on manned stations during daytime, often conducted using differing acquisition standards. For example, not all observers follow the World Meteorological Organization (WMO) guideline of only counting hail if the observed diameter is larger than 5 mm and thus may count ice pellets as hail. Hence, hail observations from SYNOP are often not able to capture the local-scale variability of hail or to fulfill quality standards accordingly. This fact makes studies based on such data highly questionable (Punge & Kunz, 2016). Since a few decades, the most common methods utilize radars to relate environmental to atmospheric conditions (Stumpf, Smith, & Hocker, 2004) aiming to improve knowledge of hail genesis and possible changes of hail dynamics in times of climate change.

While climate change is unequivocal and proved by the latest reports of the Intergovernmental Panel on Climate Change (IPCC) (IPCC, 2007, 2013), its consequences on hail are hard to measure. Due to the lack of widespread monitoring systems, missing historical data and the fact of hail being a rare phenomenon on a small-scale, long term changes related to climate change are difficult to measure and hence to predict (García-Ortega et al., 2014). Nevertheless several studies have investigated a possible relationship between climate change and thunderstorm/hail events. Kunz, Sander, and Kottmeier (2009) looked at building damage reported by insurance companies in Germany over a time span of 30 years (1974 - 2003). While no significant increase in thunderstorm events (both frequency and severity) was found, hailstorm events revealed an increment in hailstorm days and associated reported damage. For the Netherlands it was concluded that predicted climate change may increase damage associated with hailstorms (Botzen, Bouwer, & van den Bergh, 2010).

1.1. Scope of the thesis

This work aims to (i) explore the synoptic weather situation of hail occurrence in the Basque region, northern Spain and (ii) to use linear and non-linear statistical learning methods to relate surveyed "hail damages to trees" to climatic variables to estimate probabilities of hail damage to trees and to distinguish between different risk areas of possible hail damage to trees within the Basque country.

The findings of this work aim to support the scientific process of analyzing the infections of pine trees by pathogenic agents in the Basque region in northern Spain (Iturritxa, Mesanza, & Brenning, 2014).

1.2. Outline of the thesis

The theoretical background of hail genesis and its impact is presented to the reader in chapter 2. Basic information about the composition of hail and its measurement methods are given in section 2.1. To understand the dynamics of hail, the underlying micro-physical processes and the influence of large- and small-scale atmospheric flow conditions are explained in detail in section 2.2. Different scales used in practice to measure the impact of hail are given in section 2.3.

The Basque region, representing the study area of this work, and the available data are shown in chapter 3. After an exploratory analysis of the study areas properties (section 3.1), a descriptive overview of each available data set is given in section 3.2.

In chapter 4 theories of the statistical models (GLMMs and GAMMs) used in this work are introduced and information about the conducted data preprocessing and modelling steps is provided. Underlying grouping structures, their influences and how to account for them are described in section 4.4 in combination with mathematical model definitions. The various model setups used in this work and their detailed specifications are given in section 4.5. Theoretical and practical information about the setup used to validate the models are provided in section 4.6 followed by section 4.7 which presents details about the undertaken spatial prediction.

The results of all undertaken analyses are listed in chapter 5. It starts with section 5.1 showing the findings of the synoptic weather situation related to hail occurrence. Results of the statistical modelling approaches are given in section 5.2, followed by the validation analysis in section 5.3 and the spatial prediction and risk area classification (section 5.4).

The discussion starts with a note about the previously discarded concept of this work (section 6.1). Data availability and quality is discussed in section 6.2. In section 6.3, the methods of this work are critically reviewed and an interpretation of the results of this thesis is given. Major findings are summarized in section 6.4. Finally, the relation of this work to other studies (section 6.5) is discussed and suggestions for future research are provided in section 6.6.

CHAPTER 2

THEORETICAL BACKGROUND

The following chapter presents basic knowledge as well as state of the art research in the context of hail research. In section 2.1 basic terms of hail science are introduced. Micro-physical processes and other environmental influences affecting hail genesis are presented in section 2.2. Hail impact and damage is discussed in section 2.3 by comparing different scales measuring hail severity. Additionally, a closer look at hail impact on forests is taken in subsection 2.3.4. The usage of weather-radar information for hail detection and hail severity assessment is addressed in Appendix B by presenting several algorithms which are used to process weather-radar data.

2.1. Hail Definitions and Properties

Hail is defined as ice crystals with a diameter larger than 5 mm. Smaller ones, ranging from 2 mm - 5 mm are referred to as graupel. Beside size, ice crystals are sub-classified according to their micro-physical origination processes. (Geer, 1997; World Meteorological Organization, 2008)

Several factors have to be considered when speaking about hail seasons: Beside the total number of hailstorms, properties like the area affected by hail including total damage, the size of hailstones as well as local climate conditions such as convective energy and the annual temperature cycle need to be taken into account. Whereas the hail season in Europe differs highly depending on the region and its respective characteristics, the peak months are more precisely defined. Most studies consider May/June as the peak months in terms of counted hailstorms while June and July lead the monthly score regarding damage and hailstone size (Punge & Kunz, 2016).

To obtain hail risk models, hail-streak properties such as width, length and orientation are of fundamental importance. However, only few studies have investigated these aspects in detail. Limitations are simply based on data availability: To obtain substantial results in terms of width and length one would need to constantly monitor large areas using radar or other instruments. Insurance company reports showing loss related to hail can also be used since they most often cover large areas. However, such data is limited to insured objects/areas. Nevertheless, studies investigating this issue calculated an average hail-streak length of about 50 kilometers. Hail-streaks with a length of hundreds of kilometers were observed very rarely (Puskeiler, 2013; Punge & Kunz, 2016). Dessens (1986) surveyed (30 major) hailstorms between 1952 and 1981 in SW France obtaining an average length of 86 km and width of 6.3 km, respectively. For Hungary, a study by Horvath, Seres, and Nemeth (2015) has shown an average length of 70 km with a distribution mode of around 50 km.

2.1.1. Measurement of Hail

Three methods exist for observing and measuring hail on the surface: Insurance companies (Holleman, Wessels, Onvlee, & Barlag, 2000), observer networks (Changnon, 1971b, 1971a) and hailpad networks. A hailpad is a meteorological device on the ground which is able to measure properties of hailstones falling onto it, originally developed by Schleusener and Jennings (1960). In detail, hailpads "consist of a metal stem attached to a polystyrene pad designed to absorb the impact of hailstones" (Vinet, 2001). Due to its ability to provide several numerical variables of hailstones like number, weight, kinetic energy and diameter, hailpads are most exact and most often used method among the three. However, to avoid overlappings of multiple hailstorms in data logging, it is common practice to replace hailpads after every hailstorm. This leads to high maintenance costs which in turn limits the number of existing hailpad networks and their extension. According to Sánchez et al. (2013), "some of the largest operating hailpad networks are located in the province of Mendoza, Argentina (800 hailpads installed in a grid of 5 km × 5 km) and the province of Zaragoza in Spain (with a total of 100 hailpads installed every 4 km × 4 km)". Due to the high maintenance costs and the limited observable area, hailpads serve mainly as in situ reference data for hail detection methods covering larger areas such as weather-radar, first proposed by Battan (1973). This hail observation technique is explained in more detail in Appendix B.

2.1.2. Hail Size

A study carried out by Punge, Bedka, Kunz, and Werner (2014) found that hailstone sizes exceeded a diameter of 20 mm in nearly every fourth report stored in the European Severe Weather Database (ESWD). In about 3.5% of the observations the reported hailstone size was larger than 40 mm. The authors assumed an exponential relationship between number of hail events and size. However, this assumption may be biased towards large hail since such entries are more likely to be made in a voluntary database due to attractiveness reasons for both media and storm addicted people.

Regarding the size distribution of hailstones, it is assumed that it follows either a power law or an exponential function (Ludlam & Macklin, 1959; Fraile, Castro, & Sánchez, 1992) though investigations on variations in hail size distributions in literature, which result in statistically significant outcomes, are rare (Sánchez et al., 2009).

2.1.3. Hail Frequency

Most often, hail frequency is defined as the number of hail days per year for a specific area (where 'specific area' refers to a region smaller than a complete hail-streak but a large enough to be seen as a unique area to be hit by a storm). Therefore, according to Punge and Kunz (2016), it is recommended to count hail days over an area with a fixed size (e.g. hailpads).

Since hail is a small-scale phenomenon, there are only few studies which have tried to assess hail frequency on a global scale. The first map going beyond the regional level was produced by Frisby and Sansom (1967) and covers the tropics. The authors used hail data from various monitoring stations. The latest global map was produced by Cecil and Blankenship (2012) using the passive microwave instrument Advanced Microwave Scanning Radiometer-EOS (AMSR-E) on-board of the Aqua mission. Their approach utilized cloud top temperatures as a proxy for hail derivation. Nevertheless, the coarse spatial resolution of such global maps makes them unfeasible for analysis on hail probability on a regional scale. However, numerous studies exist addressing the question of hail probability on a national and regional scale with some of them being presented in Appendix B. In such studies, seasonal and daily characteristics are taken into account to obtain precise modelling results (Punge & Kunz, 2016).

While direct hail observations (with the idea to estimate hail frequency) are hard to acquire and only available in regions where hailpads or other measurement systems are installed, linking hailstorm occurrences to large-scale atmospheric flow conditions is one possibility to overcome this limitation (though it has to be ensured that for the specific area a time series produced by regional climate models is available). Besides the importance of small-scale conditions, "mesoscale thermal instability in combination with large-scale atmospheric circulation patterns" (Punge & Kunz, 2016) also have a big impact on hail origination. This topic is covered in more detail in subsection 2.2.4.

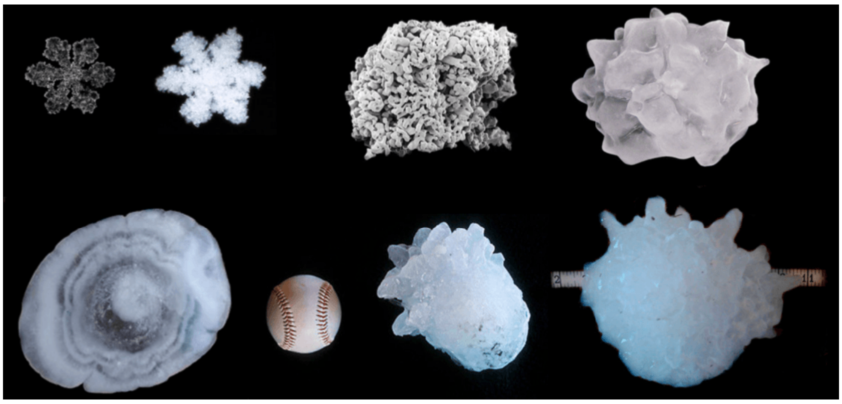

Figure 2.1.: Different ice crystals as they appear in thunderstorm cells: (up, from left to right): Ice crystal, frosted ice crystal, graupel, hail. (Low, from left to right): layer structure of hail, baseball as a reference, conical hailstone and largest ever detected hailstone with a diameter of approximately 20 cm (found in Vivian, South Dakota on 23/07/2010) (Puskeiler, 2013)

2.2. Hail Genesis

Hail consists of frozen water interspersed by small air inclusions. Depending on atmospheric conditions, hailstones vary in their shape and density (Figure 2.1). According to Pruppacher and Klett (2010), density ρ of hailstones ranges from 0.7 g/cm^{-3} to 0.9 g/cm^{-3} (pure ice: ≈ 0.9 g/cm^{-3}). Hail evolution is driven by various processes sharing different scales, both temporal- and spatial-wise. Up to now, the exact interaction of all those processed has not been fully understood.

Whilst the presence of MCS, supercells or multicells, both ice crystals and sub-cooled water drops have to be present in a recent amount in the updraft sections of such cells. Micro-physical processes (subsection 2.2.1) are then able to produce big ice crystals which are referred to as hailstones in the end (Puskeiler, 2013).

2.2.1. Micro-Physical Processes

A high number of aerosols exist in convective clouds, which usually feature a bright temperature range throughout including temperatures lower than 0°C. Important for hail and cloud genesis are the so-called Ice-forming Nuclei (IN) and Cloud Condensation Nuclei (CCN), respectively (Knight & Knight, 2001). The important micro-physical processes (Figure 2.2), which are passed through when going from aerosols to hailstones, will be explained in the following and refer to Knight and Knight (2001):

- **Deposition:** Ice crystal genesis directly from vapour phase due to ice saturation.
- **Coalescence:** Collision and merging of two water drops.
- **Accretion:** Sizable ice particle collection of either super-cooled water droplets or small ice crystals.
- **Riming:** Accretion of super-cooled cloud droplets on ice in a low-density deposit.

Whether an aerosol is capable of functioning as an IN or CCN depends on various points. According to Pruppacher and Klett (2010), aerosols have to be highly water-insoluble. If not, the aerosol structure, which sets the base for ice aggregation, would not be suitable anymore after water contact. Furthermore, aerosols need to have a minimum diameter in order to be able to serve as one of the two mentioned nuclei. This minimum

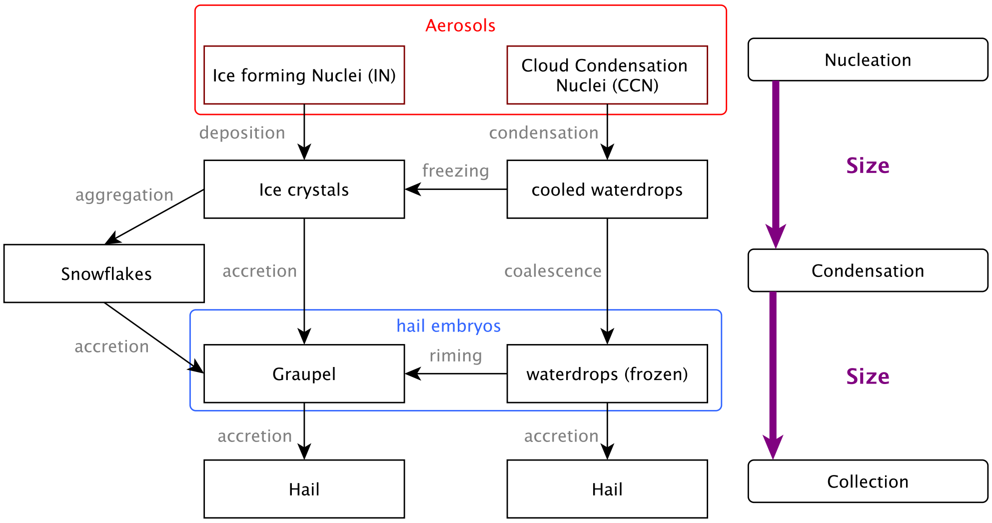

Figure 2.2.: Micro-physical processes and primary hydro-meteor growth processes of hail genesis, adapted from: Puskeiler (2013); Knight and Knight (2001)

size again depends on the cloud's temperature: For example, at -5°C an aerosol diameter of at least 0.035 µm is needed while at -20°C a value of 0.0092 µm is sufficient. Additionally, it is important that the chemical properties of the aerosols are similar to the ice crystal ones. Preferred are molecules with OH - or NH_2 groups to simplify binding processes with H_2O molecules. Last, the aerosol grid structure needs to be similar to the lattice structure of the ice crystal, too. Since the process of accretion can be seen as a structured overlay of (ice-)grids, fitting grid structures help to receive stronger bindings between layers.

Aerosols which match these conditions are very rare. At temperatures of -20°C , on average, one possible nucleus exists per liter air. The relationship between aerosols suitable for hailstone creation and all existing aerosols is roughly 10^{-6} (Bigg, 1990). The higher the concentration of such nuclei in a thunderstorm cell, the higher the probability of a spontaneous freezing of super-cooled water drops.

The method of intentionally shooting up possible nuclei into clouds (e.g. silver iodide) to prevent severe hailstorms works similarly: Since these ions are suitable nuclei (Gravenhorst & Corrin, 1969), a large number of hail embryos arise. Due to the vast amount, each hailstone becomes smaller as the water in the storm cell distributes over all nuclei. In turn, the damage potential of such hailstones is much lower compared to less but bigger hailstones.

2.2.2. Hail Genesis in Different Cloud Environments

Micro-physical processes as mentioned in subsection 2.2.1 occur most often in large thunderstorm cells. There, nuclei are able to stay long enough to accumulate many ice crystal layers which then results in large hailstones.

2.2.2.1. Supercell

Supercells are the most favorable cloud environment to support hail genesis (Figure 2.3). Since the updraft winds rotate as they move up, nuclei take quite some time to rise up. During this time, they accumulate large amounts of ice crystal layers resulting in large hailstones (Puskeiler, 2013).

On the rear side of the updraft a high number of hail embryos exist which collide with many super-cooled

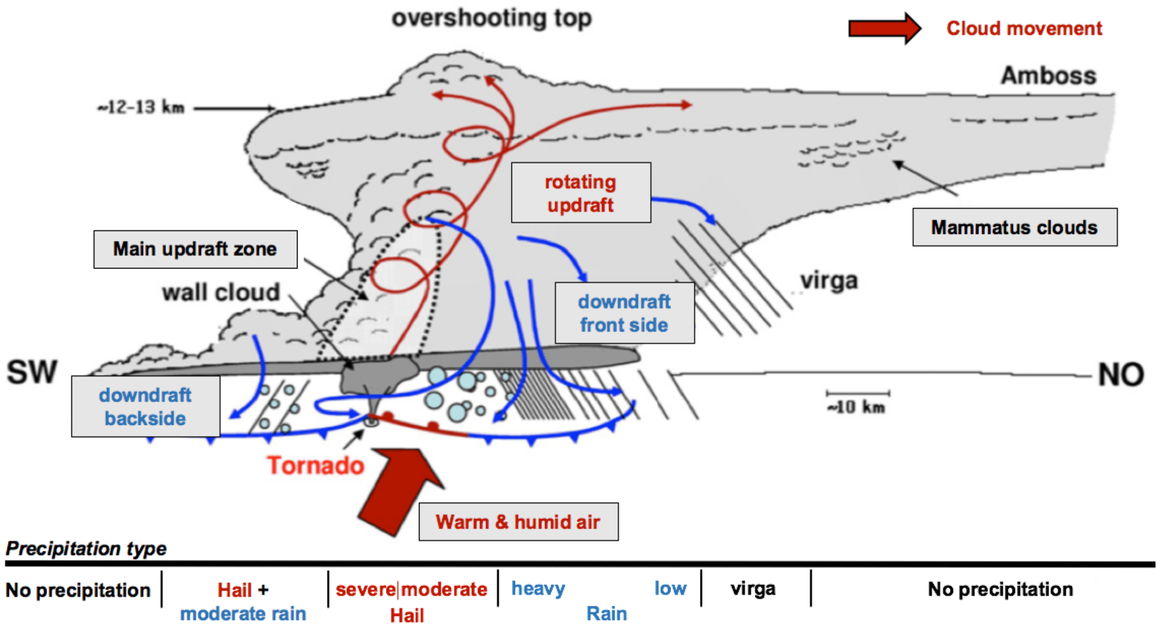

Figure 2.3.: Schematic profile of a thunderstorm supercell showing hail genesis, adapted from: Puskeiler (2013); Bluestein and Parks (1983)

water drops from the middle updraft section. Both groups clash at the border area of the updraft winds. The micro-physical process of accretion then transforms both groups into hailstones with large diameters. Due to the vertical imbalance of the updraft corridor, hailstones get slightly moved to the front section. At some point, hailstones become too heavy for the upwinds or may get rotated out of the upwind corridor. When this happens, large hailstones fall down to the ground causing a (most often) severe hail event (Browning et al., 1976; Puskeiler, 2013).

2.2.2.2. Multicell

While hail distribution in a supercell spreads over a large area with the highest intensity near the front section of the updraft winds (Figure 2.3), multicells behave differently in terms of hail genesis and distribution. Multicells are a combination of multiple cells with different development stages. In Figure 2.4 these cells are distinguished using different symbols and labels (e.g. "n - 2", "n + 1", etc.). According to Browning et al. (1976), nuclei start at the far right cell (here "n + 1") and accumulate water as they move through all cell environments. Upon reaching the point at which hailstone weight exceeds updraft power, hailstones fall to the ground in the area of the central cell (here "n - 1"). This less widely spread distribution of hail marks one difference of multicells to supercells besides the different origination process of hailstones. The concept of hailstone evolution and movement in multicells is also explained in Grenier and Zair (1983) and Heymsfield, Jameson, and Frank (1980).

2.2.3. Small-Scale Atmospheric Flow Conditions and Orography

Wind flow deflections caused by mountain ranges or hilly landscape characteristics can be an important trigger for thunderstorm and in turn hailstorm origination. Due to the importance of horizontal and vertical orography effects, many studies have investigated the influence of flow anomalies in relation to hailstorm genesis. While de la Torre et al. (2015) provided the most recent discussion on this topic addressing the local scale topography of the Southern Andes, other studies have concentrated on finding possible relations between hailstorm frequency, orography and atmospheric flow conditions in Europe (Morgan, 1973; Giaiotti, Nordio, & Stel, 2003; Kunz & Puskeiler, 2010). However, all small-scale (orography) characteristics appear to be highly complex for their specific region and no transferable statement can be made.

Generally speaking, orography is a quite obvious factor for hail frequency. Many hotspots in Europe are surrounded by mountains or located directly at such. Examples are the northern and southern pre-alpine regions of the Alps, the northern foothill region of the Pyrenees and the Massif Central in France, the Apuseni range in Romania, the Black Forest range and the Swabian Jura in Germany as well as the Ebro Valley in Spain (Punge & Kunz, 2016). The dominant flow characteristics are then determined specifically by the characteristics of these mountain(s) (-ranges), meaning their exposition, length and height, in combination with atmospheric conditions such as wind speed and direction, temperature and many more (R. B. Smith, 1979).

de la Torre et al. (2015) found out that hailstorm origination mainly occurs in downstream areas of hilly terrain (or very close by). Hail events directly over mountains, however, occur only infrequently and depend on complex interactions between different atmospheric mechanisms, further discussed in the given paper. Another hypothesis claims channeled air masses among mountain ranges to be responsible for higher hail frequency observations, like García-Ortega et al. (2007) for the Ebro Valley in Spain while Mallafré et al. (2009) showed the influence of convergence caused by the wake of the Iberian system to be a main trigger for hail in this region.

2.2.4. Large-Scale Atmospheric Flow Conditions

Local-scale flow conditions as explained in subsection 2.2.3 are not only affected by local characteristics but also by large-scale flow conditions. These are responsible for thermal instabilities causing origination and persis-

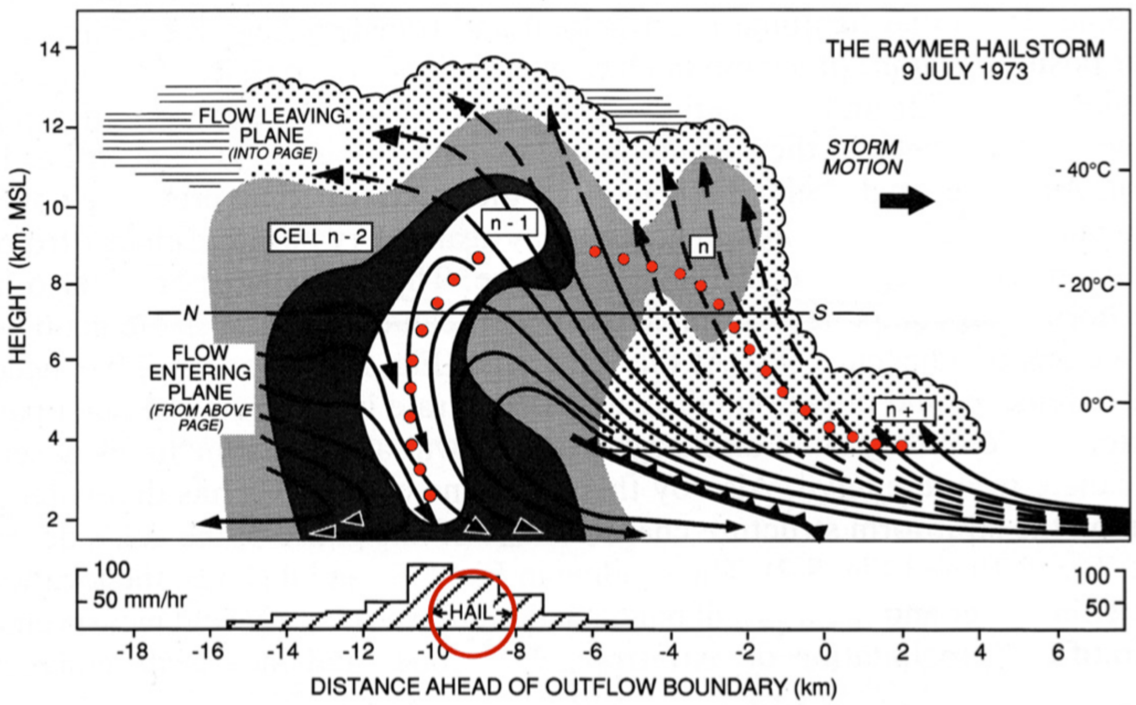

Figure 2.4.: Hail origination in a multicell. Red dots mark a possible path of a hailstone moving throughout different cell development stages starting from the most right cell (n + 1), adapted from: Puskeiler (2013); Browning et al. (1976)

tence of intense thunderstorms. Maintenance of such events relies on reinforcement of cold air advection at higher levels of altitude together with advection of moist and warm air at lower altitudes. Addressing western and central Europe, the prevailing meteorological situation of severe hail events can be described "by an extended trough with its center over the West European Basin or the Bay of Biscay, and a ridge downstream near or over the Mediterranean" (Punge & Kunz, 2016). This results in warm and moist air being transported to central Europe due to winds coming from the southwest. This is the most often occurring and observed meteorological scenario during hail events in various European regions, proved by several studies in France (Vinet, 2001; Berthet, Wesolek, Dessens, & Sanchez, 2013), the Ebro Valley in Spain (García-Ortega, López, & Sánchez, 2011), Switzerland (Schiesser, 2003), Germany (Kunz et al., 2009; Kapsch, Kunz, Vitolo, & Economou, 2012) or Poland (Kolkowska & Lorenc, 2012).

Other studies have proved the relationship of more hail occurrences being associated with a higher Convective Available Potential Energy (CAPE) in combination with vertical wind shear (= difference in wind speed/direction over a relatively short distance) (Laing & Fritsch, 2000; Brooks, Lee, & Craven, 2003) while Mohr, Kunz, and Keuler (2015) assumed the combination of the Liftex Index (= difference in temperature of a parcel lifted to the tropopause and the temperature of the surrounding air in the tropopause), minimum and maximum temperatures as well as large-scale weather patterns to be the main predictors for hail genesis in Germany.

On the synoptic scale (= horizontal scale of around 1000 kilometers), Europe is influenced by pressure systems and their fronts moving from west to east due to the west-wind zone in these latitudes. The lows and highs develop over the North Atlantic causing severe hailstorms to occur mainly over Western and Central Europe. Hail events occur either "at a distance ahead of cold fronts by low-level flow convergence or at the front due to a combination of increased instability in case of cold air advection aloft and convergence by cross-circulation" (Punge & Kunz, 2016). The assumption of fronts being an important trigger of deep convection and hail events was investigated in Spain (García-Ortega et al., 2007), France (van Delden, 1998), Poland (Kolkowska & Lorenc, 2012), Bulgaria (Simeonov & Georgiev, 2003) and in Cyprus (Michaelides et al., 2008).

2.2.5. Geographical Influence: Moisture Availability and Solar Radiation

As mentioned in subsection 2.2.4, an unstable thermal environment is required for hail origination. Subsequently, warming of surface layers due to solar radiation combined with a cooling aloft favors convective flows and in turn thunder-/hailstorm development. If such heating effects of surface layers are missing, severe storms cannot develop. This is generally the case during winter in Europe. The summer conditions in Europe with its long daytime favor thunderstorm genesis with hail larger than 4 cm in diameter up to regions with a latitude of 68 °N. Since temperature and solar radiation decrease with higher latitudes, the decreasing distance to the north pole is the main reason for a low number of hail events in Northern Europe (Punkka & Bister, 2005; Tuovinen, Punkka, Rauhala, Hohti, & Schultz, 2009).

Referring to Waldvogel, Federer, and Grimm (1979), for hailstorm originiation it is essential to have a cold middle and upper troposphere layer. The warmer these layers are, the more hailstones get melted during their way down to the ground, resulting in small or no hail at all. This state occurs mainly in areas with high solar radiation and explains the relatively low number of hail events in Southern Europe during midsummer (Camuffo & Sturaro, 2001) and the increase of the hail/thunderstorm ratio during nighttime (Manzato, 2007).

The presence of sufficient amount of moisture is an important prerequisite for the development of intense convective cloud formations. This is the reason why severe storms are mainly formed by latent condensation processes over seas (Markowski & Richardson, 2010). In some regions hail frequency increases during spring time, like in Scotland and England (UK Met. Office, 2015) or Greece (Sioutas, 2011). The phenomenon of latent condensation usually appears in areas located along coasts due to the influx of moist air coming from the sea. However, the type of precipitation of such events is limited to small hail or graupel in the majority of cases as the air temperature values are too low during spring.

2.3. Impact and Damage of Hail

Central Europe, in particular Germany, Switzerland, Austria and France, and Mediterranean Europe (i.e. Spain, Portugal) is highly affected by hazardous hail events. This is due to the fact that hail frequency and severity decreases from west to east and south to north. Moisture availability and contingency of weather fronts decreases as continentality increases which leads to more unfavorable conditions for hail genesis. Thus, the most hazardous hail events which occurred over the last hundreds of years took place in these European countries (Punge & Kunz, 2016).

Keeping in mind that damage estimations of hail events are very complex and that the severity of a hail event cannot always be determined just by the maximum observed hailstone size, the hail event occurring on the 12/07/1984 in Munich was one of the first largest reported hail events in Germany, causing an estimated damage of 3000 million Euro (Table 2.1). With a maximum observed hailstone size of 8 cm, the hail event named after the front "Andreas", which occurred on the 28/07/2013 in Germany had a lower observed maximum diameter than the one in Munich (9.5 cm) but a higher reported economical damage (~3600 Euro). One of the largest reported hail events in terms of hailstone size (12 cm) was caused by the front "Felix" in Belgium and France on the 26/05/2009. However, it only caused moderate economical damage (~700 Euro), taking hailstone size and other hail events with similar size into account.

Table 2.1.: Most substantial and costly hailstorm events in Europe (Punge & Kunz, 2016)

Name	Regions	Date	Max. hail size (cm)	Economic damage million EUR (2015)	Insured damage million EUR (2015)	Reference
France 1788	France: Ille de France, Picardie, Pays de la Loire	13 July 1788	8	250		Lachiver (2000) Tessier, Buache, and Leroy (1790)
England 1843	UK: Gloucester, Oxfordshire, Northampton, Cambridge, Norfolk	9 August 1843				J. D. C. Webb and Elsom (1994)
Munich Hailstorm	Germany: Southern Bavaria	12 July 1984	9.5 / 14	1500	3000	Heimann and Kurz (1985) Höller and Reinhardt (1986) Kaspar and Mueller (2009)
Felix	Belgium: Western Belgium France: Picardie, Nord	26 May 2009	9 12	700	580	Hamid and Buelens (2009), ESWD, Keraunos (2009)
Wolfgang	Austria, Salzburg, Upper Austria, Lower Austria, Switzerland: Berne, Lucerne	23 July 2009	10		833	Willis[1]
Andreas	Germany: Baden-Würtemberg, Lower Saxony, NRW	27-28 July 2013	8 / 7	3600	2800	Kunz et al. (2015), Munich Re
Ela	France, Ille-de-France Centre, Western Belgium	8-10 June 2014	12.5		2300	Willis[1]

[1] Willis Research Network (WRN)

Table 2.2.: The ANELFA scale of point hailfall intensity (Dessens et al., 2007)

Class	Maximum hailstone diameter (cm)	Largest hailstone equivalence	Energy range (J m^{-2})	Typical damage
A0	< 1	Pea	0 - 30	Road accidents tree flowers cut
A1	1 - 1.9	Grape, marble, cherry	30 - 100	Damage to vineyards orchards, tobacco
A2	2 - 2.9	Pigeon´s egg	100 - 400	Serious damage to cereals vegetable, trees
A3	3 - 3.9	Walnut, ping-pong ball	400 - 800	Complete damages to all crops windows cut, cars damaged
A4	4 - 4.9	Hen´s egg, golf ball	> 800	Winter landscape, animals killed people injured, grounded aircraft damaged
A5	>= 5	Orange, peach apple, tennis ball		Extreme dangerous event unprotected persons killed

The class number is followed by a + or - sign if the ground is more less than half-covered by hailstones respectively

2.3.1. The ANELFA Scale

Several scales exist which categorize hail damage. Most of them rely either on the kinetic energy measured, size of hailstones or maximum observed damages. One is the ANELFA scale (Dessens et al., 2007). It relates hailfall to a small area, similar to the size of a hailpad (~0.1 m^2). The intention of this scale is to measure the size of hailstones at a small location, resulting in a detailed overview of hail intensity if a dense network of hailpads is available.

It is based on the "Fujita scale for tornadoes" (Fujita, 1971) and has therefore six classes, labeled from A0 to A5. Here, *A* refers to ANELFA but also to the standard coding sign "A" traditionally used in aviation weather observations for hail (Glickman, 2000). The intensity value (A0 = lowest, A5 = highest) refers to the value of the largest measured hailstone diameter (in cm). Class A5 includes all hailstones bigger than 5 cm. If more than 50%

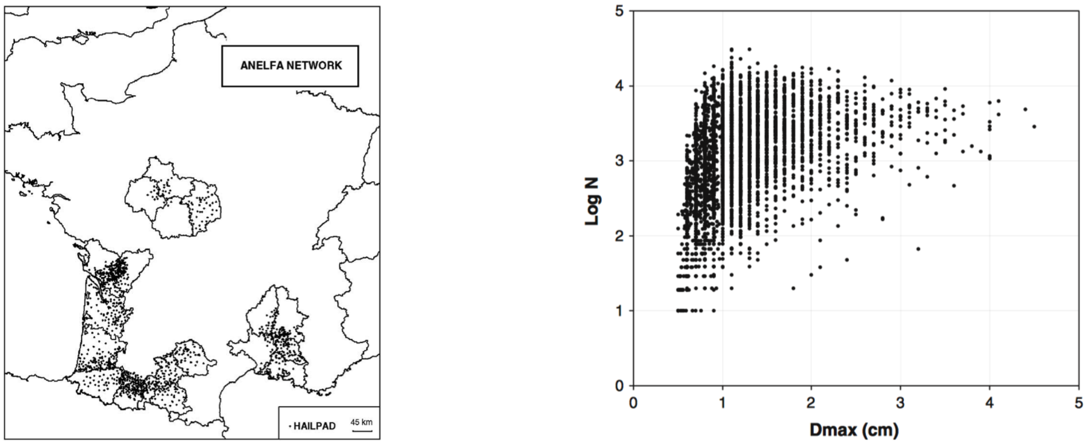

(a) Map of France with the ANELFA hailpad stations

(b) Log of total number of hailstones vs. diameter of largest observed hailstone (Dmax) for 3611 point hailfall observations (Log N)

Figure 2.5.: ANELFA station distribution and observed hailstone diameter as a function of total number of hailfalls (Dessens et al., 2007)

of the measured area (e.g. hailpad) is covered by hailstones, a plus sign is attached to the class label. Values lower than 50% are followed by a minus sign.

The ANELFA scale was used in Southern France from 1988 - 2003, where a dense hailpad network exists (Figure 2.5a). During this time, 3611 point hailfalls were recorded, distributed over 926 stations (= mean number of installed hailpads over the years). The records show a spherical relationship of the observed maximum hailstone diameter against the log of the total number of hailfalls (Figure 2.5b) (Dessens et al., 2007).

2.3.2. The TORRO Scale

The Tornado and Storm Research Organization (TORRO) has proposed a hailstorm intensity scale with ten classes (placed in Appendix C due to its large size), specifying hailstone diameter size as well as their damage effects to the environment (J. Webb, Elsom, & Meaden, 1986). The scale was named after TORRO itself. Originally, the aim was to increase consistency for hailstorm damage reports in Britain. It was developed on the base of several hundred hailstorm observations starting from 1866 (100 year streak). Referring to J. Webb et al. (1986), hail events of scale *H0* are called "non-damaging/moderate hailstorms", *H1* - *H4* "damaging hailstorms", *H5* - *H8* refer to "destructive hail events" and *H9* - *H10* are classified as "super hailstorms".

Although the TORRO scale also refers to point hailfall observations, wind speed is taken into account when classifying damages of hail events. Thus, a hail event with a marble-like hailstone size (1.6 cm - 2 cm) can be classified either as H1, H2, H3 or H4 depending on its damage effects. Damages are more severe with stronger wind speeds (J. Webb et al., 1986). The TORRO scale is similar to the ANELFA scale in the first five classes. Class *A5* of the ANELFA scales comprises classes *H6* - *H10* of the TORRO scale which spans more sub-classes for severe hail events.

2.3.3. The GSC Scale

According to Dessens et al. (2007), another hail scale exists which was first proposed by Moisselin and Guillande (2004) and resembles the ANELFA scale. It was developed under the leadership of the Geoscience Consultants (GSC) in partnership with *Météo-France* and the French *Centre national du machinisme agricole du génie rural, des eaux et des forêts* (CEMAGREF). The scale relies on a combination of maximum observed hailstone diameter and observed damage "at the scale of a French *commune*" (Dessens et al., 2007). The GSC scale only differs in one class compared to the ANELFA scale as it consists of five classes instead of six.

Table 2.3.: Correspondences between hailfall intensity scales (Dessens et al., 2007)

Name	Class					
ANELFA	A0	A1	A2	A3	A4	A5
TORRO	H0	H1	H2	H3	H4 - H5	H6 - H10
GSC	1	2	3	4	4	5

ANELFA: Association Nationale d’Etude et de Lutte contre les Fléaux Atmosphériques
TORRO: Tornado and Storm Research Organization
GSC: Geosciences Consultants

2.3.4. Hail Impact on Forest Stands

Requirements of a tree getting wounded by hail depends on its species and hailstone size. However, direct consequences of hail damage on forests are relatively small compared to indirect ones. Follow-up infections of wounds through pathogenic agents most often result in the tree having to be cut down. With an areal plantation coverage of at least 2.8 million hectares, the Monterey Pine (Pinus radiata) is the most widely spread tree species worldwide. While it is the most cultivated species in Chile, Australia, New Zealand and Spain, it also has a high importance in Uruguay, South Africa, and Kenya (Iturritxa et al., 2014).

Depending on the country and its climatic conditions, several fungal agents exist which infect hail wounds of *P. Radiata*. These are namely *Diplodia Pinea* (= *Sphaeropsis Sapinea*), *Fusarium Circinatum* (teleomorph = *Gibberella Circinata*), and *Mycosphaerella* spp.: *Dothistroma Pini*and *Mycosphaerella Dearnessii* (synonym *Scirrhia Acicola*, anamorph *Lecanosticta Acicola*) (Iturritxa et al., 2014; Zwolinski, Swart, & Wingfield, 1995; H. Smith, Wingfield, & Coutinho, 2002; Minko, 1979).

Direct damages observed on *P. Radiata* stands near Myrtlefold, Victoria (Australia) manifested in "open and occluded scars on the limbs and trunk", "death of original tree top" up to "hail imprints on the bark [which] often indicate the presence of seperation of wood between growth rings" (Minko, 1979). Other types of tree degredation showed up as "cankers on the tree trunk, faulty knots, and accumulations of resin which caused staining when softened during seasoning". Furthermore, tree crowns got defoliated, and partially or completely barked of limbs and trunks. The described damages were caused by large hailstones featuring a diameter size of golf balls in combination with strong winds. Mainly trees aged from 8 to 13 years were affected, although the complete stand (ranging from 4 to 13 years) was equally hit by the storm (Minko, 1979).

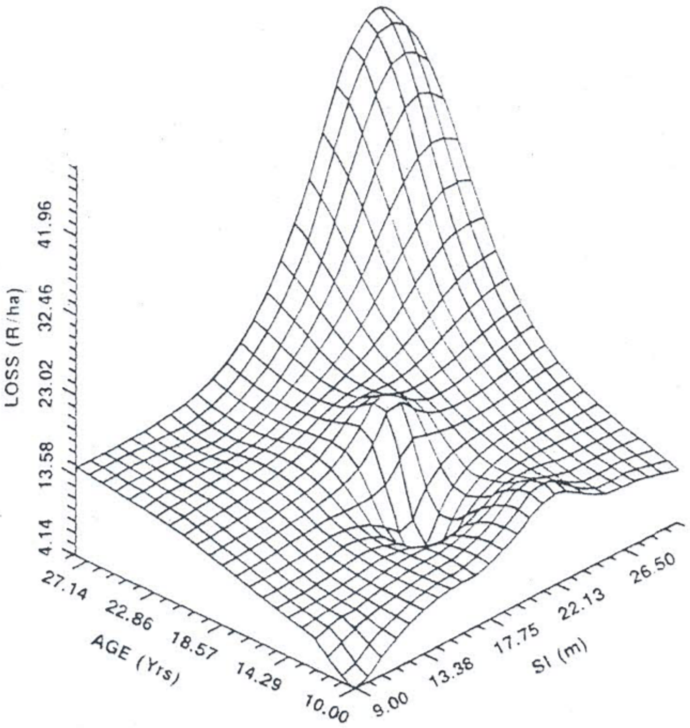

Figure 2.6.: The effect of site index (SI) and age of stands on the loss of value of timber utilized from *P. Radiata* stands prematurely clear-felled due to *S. Sapinea* infection at Kruisfontein State Forest. Loss in Rand/ha (1€ ~16,8 Rand (July 2016)), Zwolinski et al. (1990)

After the occurrence of a severe hailstorm on 3 February 1986 at Kruisfontein (South Africa), Zwolinski et al. (1995) observed the effects of an *S. Sapinea* outbreak on a 13-year old *P. Radiata* stand. The relationship of fungus and host is complex and involves different factors interacting with each other. Examples are environmental (temperature, precipitation) and physical (slope, terrain height, etc.) conditions (Swart, Wingfield, & Knox-Davies, 1987). Observed consequences on trees after a *S. Sapinea* infection are physiological stress (Wright & Marks, 1970; Marks & Minko, 1974), most often combined with visible damage on the specific tree due to hail or pruning (Swart et al., 1987; Zwolinski et al., 1995). The authors of the study also concluded a relationship between *P. Radiata* infection by *S. Sapinea* and a follow up colonization by *Pissodes Nemorensis*, which aggravate the *S. Sapinea* infection and in turn forces the die-back of *P. Radiata* trees (Zwolinski et al., 1995).

In a prior study, (Zwolinski et al., 1990) estimated the economic damage of *P. Radiata* die-back in relation to tree age and Site Index (SI). The SI is defined as "[t]he average age of dominate and/or co-dominate trees of an even-aged, undisturbed site of intolerant trees at a base age" (Nyland, 2002) and is used in forestry to assess productivity of a forest stand as it measures the tree height of a stand at base ages such as 25, 50 and 100 years (Avery & Burkhart, 2002). The biggest losses were attributed to high quality sites (= high SI) in combination with older trees (Figure 2.6). Old trees are more susceptible getting infected by *S. Sapinea* and have a higher economic value of timber.

Due to the vast amount of *P. Radiata* die-back after *S. Sapinea* infections, planting of this tree species was stopped in the early stages of the 20th century in South Africa. By 1925, most of *P. Radiata* stands had been replaced by *P. Patula* stands which were believed to be resistant against *S. Sapinea* infections (H. Smith et al., 2002). However, beginning in the early 1930s, infections of *P. Patula* were observed occasionally. They steadily increased so that by 1940, P. Patula was affected by *S. Sapinea* in the same manner as *P. Radiata*. If a tree is affected by hail, "the colonization of branch pith tissue by *S. Sapinea* changes" (H. Smith et al., 2002). The authors found that the "discoloration of the branch pith" of a tree damaged by hail was extensive. It was concluded that hail stressed the trees so much that the *S. Sapinea* pathogens were activated and spread throughout "the pith tissue of the branches" (H. Smith et al., 2002).

CHAPTER 3

DATA AND STUDY AREA

The following chapter gives an overview of the characteristics of the study area, the Basque region in northern Spain (section 3.1) and describes the data that were used within this work (section 3.2).

3.1. Study Area (Basque Region, Spain)

The study area of this thesis is the Basque region in northern Spain. It covers an area of 7355 km^2 and is located between 42°34’ and 43°31’ N and 1°47’ E and 3°29’ W (Figure 3.1). While the northern part is characterized by a temperate maritime climate due to its exposition to the sea, the southern part shows an increasing Mediterranean influence. Precipitation decreases towards the south while summer drought time increases. The mean annual precipitation covers a range from 600 mm to 2000 mm with a yearly mean temperature from 8°C up to 16°C (Ganuza & Almendros, 2003).

While the cities Bilbao and San Sebastian represent the climatic situation of the study area´s northern part, the climate of Vitoria is not only influenced by its more southern location but also by its altitude lying 513 m above mean sea level. Vitoria´s long term mean annual temperature (11.9°C) is about three degrees C lower than Bilbao´s and San Sebastian´s (15.1°C and 15.4°C, respectively) (Figure 3.2). The highest precipitation values for all stations are observed during winter time (November - April) with the peak month being November and the

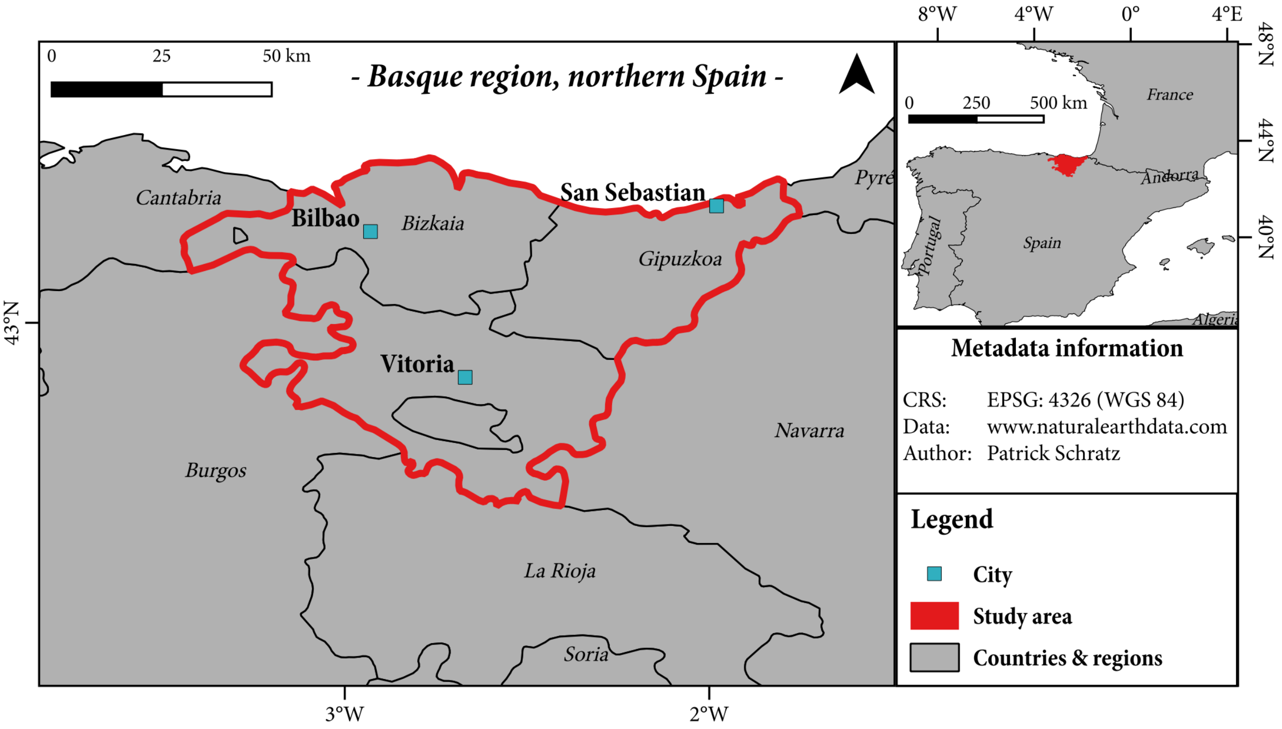

Figure 3.1.: Study area, Basque Country (northern Spain)

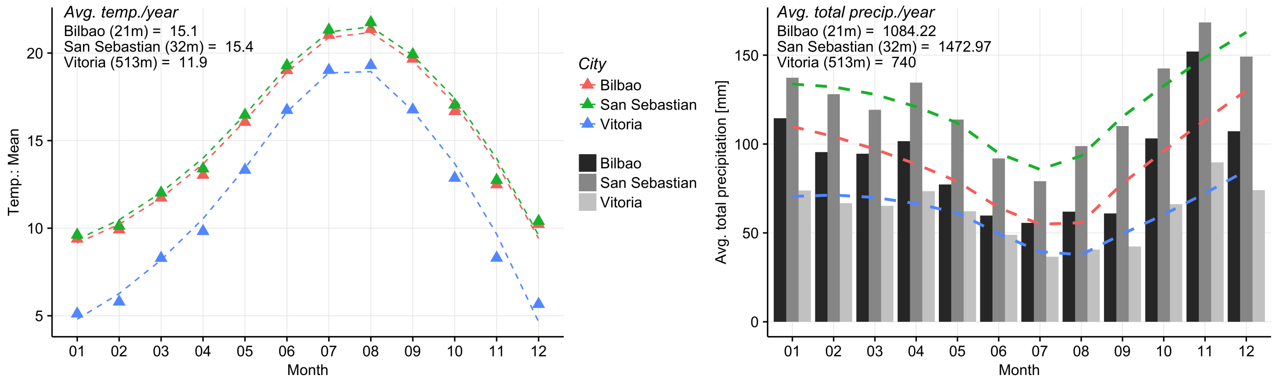

Figure 3.2.: Long term climate diagrams (1973 - 2015) of Bilbao, San Sebastian and Vitoria (Spain) showing mean temperature (°C, left) and total precipitation (mm/m^2, right) by month. Data source: World Meteorological Organization (2016)

month with the lowest precipitation being July. The month with the highest monthly average temperature for all stations is August. According to climate classification after Köppen, the Basque region is declared to have a "Cfb" climate (= marine west coast-mild) (Borja & Collins, 2004).
The climatic differences in combination with the sophisticated orography, featuring several mountain ranges across the region in an east-west direction, makes the Basque region highly diverse regarding its environmental conditions. A high range of land cover spans across the region including deciduous forest, evergreen forest, shrub and pastures. With a percentage of 59%, forest areas are the most widely spread land use class in the Basque Country, followed by pastures claiming 26%. Shrub and urban occupy 7% each, leaving 1% of cultivated land (Ganuza & Almendros, 2003; Borja & Collins, 2004).

Roughly 67% of the forest areas are plantations with coniferous trees, mainly being located in the northern part of the Basque region. The remaining 33% consist of broad-leaved forests, mostly being found in the southern, mountainous areas.

Two atmospheric conditions occur very often in the Basque region: A mesoscale storm event called *Galernas* and the Foehn effect. The first manifests as an abrupt change in both wind speed and direction. It occurs mainly in summer in combination with hot and moist air. *Galernas* are supported by southern winds and do not occur

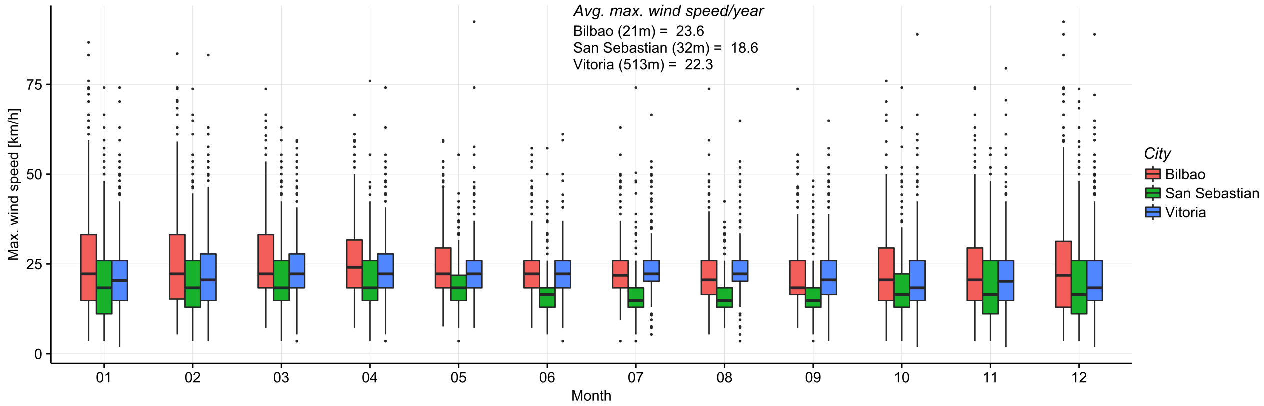

Figure 3.3.: Boxplots showing maximum wind speed distributions by month of Bilbao, San Sebastian and Vitoria. Data source: World Meteorological Organization (2016)

in combination with northern winds. On a synoptic scale, a high pressure gradient is often observed. The phenomenon results in strong winds and rain, with mean wind speeds higher than 80 km/h. If the wind speed does not exceed 50 km/h, the phenomenon is called *galernilla* instead of *galerna*. Temperature values can decrease to 12 degree C in a short time and the relative humidity rises up to levels at which condensation processes take place. *Galernas* disappear after a short time and the previous weather situation reoccurs (Borja & Collins, 2004). *Galernas* are sub-classified into two types, the "typical" and the "translation" one. "Typical" *galernas* are a small-scale phenomenon, normally showing up around the north coast. They have a mesoscale extent and do not infer storms and cause only slight depressions. "Typical" *galernas* do not develop in higher altitudes. On the other hand, "translation" galernas are colligated with "frontal perturbations, energetic secondary depressions or squall lines" (Borja & Collins, 2004). They affect the whole northern Spanish coast as well as nearby land areas. Moving eastwards, they start to create storms and showers. Bilbao and San Sebastian are situated in the area influenced by *Galernas*. This most likely contributes to the higher Interquartile Range (IQR) regarding maximum observed wind speeds of these two cities compared to Vitoria (Figure 3.3), which is located in the mountainous south of the Basque region (Figure 3.4).

The "Foehn Effect" is a common atmospheric phenomenon in areas with a high relief intensity like the Alps (south to north), the Jura or the Rocky Mountains (west to east) (Barry & Chorley, 1998). In the case of the Basque region, very warm and dry air comes from the south (northern Africa). The mountain range around Vitoria (Figure 3.4), which is referred to as the eastern part of the *Cantabrian range*, induces the ascent of the warm air from the south due to its orographical situation. During this procedure, the air cools down. Additionally, rain may occur if condensation processes take place during this ascent, eliminating the moisture content of the air masses. After passing the mountain range, the air descents and heats up again, resulting in higher temperatures in the northern part of the Basque country (Figure 3.2) (Borja & Collins, 2004).

A gradient along the *Cantabrian range* can be observed for precipitation and mean temperature values across the year (Figure 3.4). Yearly mean precipitation values of around 1200 mm/m^2 are observed for the northern and northeastern part of the Basque region while in the southwest, rainfall amounts often do not exceed 800 mm/m^2. Mean temperature values stay below 11°C for most parts located south of the Cantabrian range while yearly mean values between 12°C - 15°C are reached in the northern exposed part. PISR shows a spatially homogeneous distribution for the whole Basque country ranging around 2000 kW/m^2.

3.2. Data

3.2.1. LiDAR based 25 m Digital Elevation Model

Euskadi (2013) used point cloud information with a density of 2 points/m^2 to derive height information for the Basque country. Data sets with a spatial resolutions of 1 m, 5 m and 25 m are available at `ftp://ftp.geo.euskadi.net/lidar/MDE_LIDAR_2013_ETRS89/`. For this work, the 25 m data set was sufficient.

3.2.2. The "Global Surface Summary of [the] Day" product

The Global Summary of [the] Day (GSOD) data set is based on data exchanged under the WMO program "World Weather Watch". The National Climate Data Center (NCDC) is responsible for product maintenance. The input data used for the daily summaries is based on the "Integrated Surface Data" (ISD), which includes global data retrieved from the USAF Climatology Center. The recording of the database started in 1929, with more than

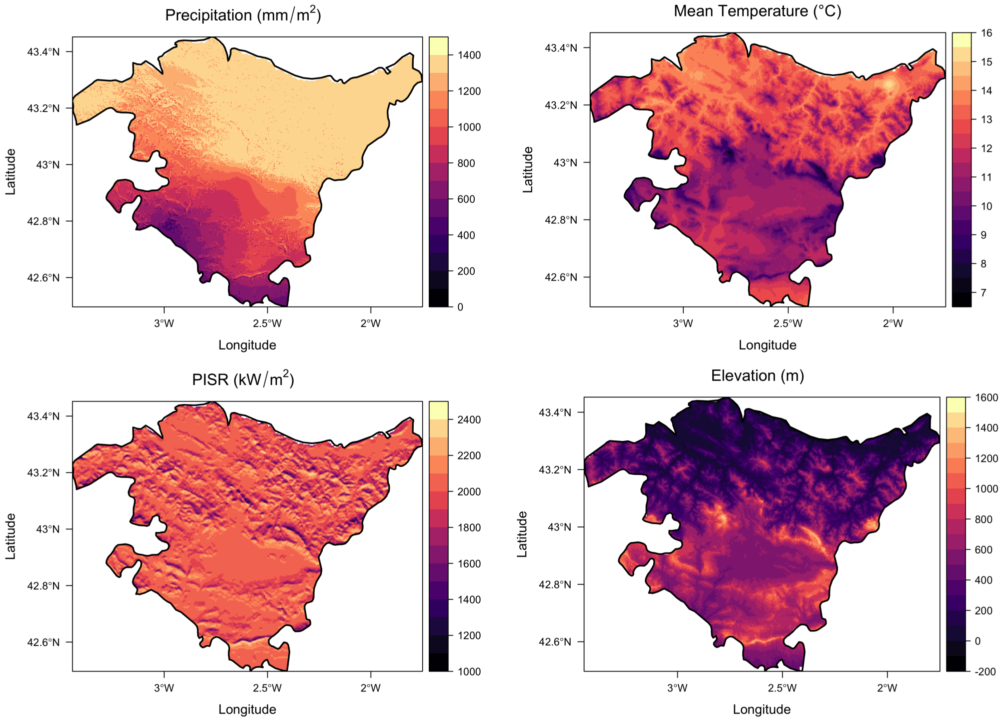

Figure 3.4.: Yearly spatial mean values of precipitation, mean temperature and PISR. Additionally, elevation information of the Basque region with a spatial resolution of 25 m. DEM data source: Euskadi (2013), others: Ninyerola et al. (2005)

9000 available stations today worldwide (World Meteorological Organization, 2016). The contents of the daily data sets are as follows:

- minimum temperature (.1 Fahrenheit)
- mean temperature (.1 Fahrenheit)
- maximum temperature (.1 Fahrenheit)
- mean dew point (.1 Fahrenheit)
- mean sea level pressure (.1 mb)
- mean station pressure (.1 mb)
- mean visibility (.1 miles)
- mean wind speed (.1 knots)
- maximum sustained wind speed (.1 knots)
- maximum wind gust (.1 knots)
- precipitation amount (.01 inches)
- snow depth (.1 inches)
- indicator for occurrence of:
  - fog
  - rain or drizzle
  - snow or ice pellets
  - hail
  - thunder
  - tornado/funnel cloud

The data is derived from hourly observations. At least four hourly reports per station/day must be present to record a daily value in the summary, otherwise the value is set to "NA". Although historical data exist since 1929, stable data summaries can only be retrieved starting 1973. Daily extreme and total values (e.g. maximum wind gust, precipitation amount and snow depth) "will only appear if the station reports the data sufficiently to provide a valid value" (National Climatic Data Center, 2016). Regarding quality control of the data set, the

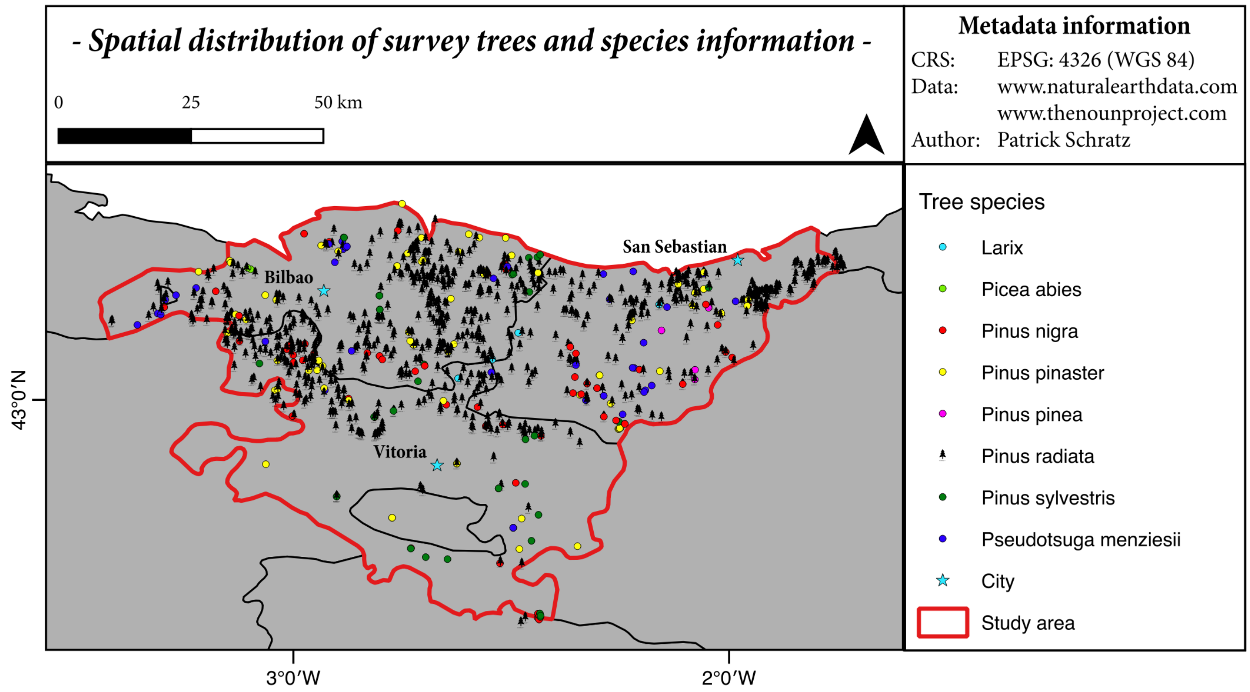

Figure 3.5.: Spatial distribution of survey trees and species information

product description states that "the input data undergo extensive automated QC to correctly 'decode' as much of the synoptic data as possible, and to eliminate many of the random errors found in the original data" (National Climatic Data Center, 2016). For the occurrence of hail and other weather phenomena, there is no additional information available for the binary response acquisition (i.e. whether checked manually or automatically).

3.2.3. Atlas Climatico Data

The *Atlas Climatico* data set is based on long term observations (1951-1999) of meteorological stations across the Iberian Peninsula. A total of "3528 meteorological stations for thermometric measures and 7293 stations for rain gauge measures" (Ninyerola et al., 2005) were available. To guarantee robustness in temporal and spatial aspects, stations were narrowed down to 286 thermometric, 1217 rain gauge and 782 pluviothermometric stations. For temperature observations 15 or more years of data were used and for precipitation at least 20 years of station information. A Digital Elevation Model (DEM) with a spatial resolution of 200 m was used during data set production. The interpolation approach is further explained in Ninyerola, Pons, and Roure (2000). The data set consists of monthly and yearly averages of the following variables:

- minimum temperature (.1 °C)
- mean temperature (.1 °C)
- maximum temperature (.1 °C)
- precipitation amount (.1 mm/m^2)
- PISR amount (kW/m^2)

3.2.4. Tree Survey Data set

This data set contains tree survey data from 14/01/2009 to 28/02/2012. Two evaluators inspected hail damages on trees and infections of pathogenic agents such as *Fusarium Circinatum*, *Mycosphaerella spp.*, *Diplodia Pinea* and *Dothistroma Pini*. Furthermore, latitude and longitude information of the surveyed trees, tree age and species are provided. The Tree Survey Dataset (TSD) consists of 1170 unique observations:

- Hail damage [True/False]
- Latitude, Longitude
- Tree age [years]
- Tree species
- Year of acquisition
- Evaluator information
- Pathogenic agent [True/False]

CHAPTER 4

METHODS

This chapter introduces and explains the methods used in this work to derive probabilites of "hail damage to trees" and in turn identify risk areas in the Basque Country. Preprocessing of the data sets is presented concisely in section 4.1. The the synoptic weather situation related to hail occurrence is examined in section 4.2. Statistical models (GLMMs and GAMMs) were used to model the response *hail*. Hence, basic model theories are presented in section 4.4, followed by the respective practical model specifications used in this work (section 4.5). Validation theory of the models and its application are described and section 4.6 while the prediction approach is explained in section 4.7.

4.1. Data Preprocessing

4.1.1. GSOD Data

The GSOD data set was cleaned from rows containing missing values (995 out of 47377 observations). Unnecessary columns were removed from the data set (e.g. "visibility in km"). Column names were changed to descriptive ones (e.g. "TempMean" instead of "TEMP"). Units of specific columns were changed: Fahrenheit to degrees Celsius (Temperature), inches to millimeter (Precipitation) and knots to km/h (Wind Speed). Hail information was extracted out of a column giving information about special weather phenomena (like fog, thunderstorm, hail etc.) and other information beside hail was dropped. Finally, the data was gathered by month for the years 1973 - 2015.

4.1.2. Atlas Climatico Data

Data was unzipped and read in as "ESRI ASCII" files, converted into .tif format and the projection "WGS84 UTM Zone 30N" was applied. After subsetting the data to the study area extent, the Spanish file names were changed into English ones.

4.1.3. Tree Survey Data set

The data was already available in a clean state. Climatic information (temperature, precipitation, PISR) from the Atlas Climatico data set was added to TSD using a zonal statistics approach. Elevation information from the Light Detection and Ranging (LiDAR) DEM was extracted and attributed to TSD data set.

4.2. Synoptic Weather Situation Related to Hail Occurrence

Since the GSOD data (subsection 3.2.2) is only available at three locations (Bilbao, San Sebastian and Vitoria), this data cannot be used to train models predicting a hail-damage on trees probability map of the Basque region. Instead, it was used for exploratory analysis to gain more knowledge of the dynamics associated with hail on a synoptic scale. Due to the low number of missing values and the long time period of 43 years (1973 - 2015), the data retrieved from each station serves as a good base to explore long term hail occurrences.

To explore the synoptic weather situation associated with hail for the time period between 1973 - 2015, hail events were plotted against time (subsection 5.1.1) and versus temperature, precipitation and wind speed, all retrieved from the GSOD data set (subsection 5.1.2). Findings of inner-yearly hail occurrence distribution help to set a more suitable time range of the predictors used for modelling. If hail only occurs during a certain time period of the year, predictors can be adjusted to this time range.

To gather a deeper insight into the response/predictor relationships, the variables "Temperature (min/mean/-max)", "Precipitation amount" and "Wind speed (mean/max)" were plotted against the binary response (Hail/No Hail). Conditional density plots were used for visualization. They are also known as "mosaic plots" or "spinograms" (in this particular case with y being categorical and x numerical). First, x, the continuous variable, gets discretized (based on its empirical histogram distribution) followed by the calculation of empirical relative frequencies of y for every group x. A probability value ranging from 0-1 is returned for every group of x. The histogram grouping is important as it reveals the underlying distribution of x which influences the following probability calculation. Probability estimations for a group x with low number of observations (shown as small bins) are more vague than those for groups with more observations of x (wider bins).

Vitoria was chosen to serve as an example station for conditional density plots of hail against various climatic variables due to the fact that it shows the highest total number of hail events for the time period November - April of all three stations. This has the positive effect of a more balanced Hail/No Hail ratio which makes the spinograms easier to interpret owing to a better plot visualization than for Bilbao and San Sebastian (which are provided in Appendix A.

4.3. Selection of Predictors

To create probability maps of hail-damage on trees for the Basque region, the TSD data set was utilized. The modeled response was *hail*. Predictor selection in statistical models is crucial for various reasons: A statistical model should consist of predictors explaining the response variable which do not introduce (multi-) collinearity into the model. This may lead to over-smoothing of the model (Zuur, Ieno, Walker, Saveliev, & Smith, 2008).

Often predictor selection is limited due to restricted data availability or data gaps. For this work, temperature (min, mean, max), PISR, precipitation (sum) and elevation were available to represent the climatic situation of hail occurrence. Age of the surveyed trees (*age* from here onwards) was included into the model as an indicator of tree healthiness representing a biological component. Since different types of temperatures (min, mean, max) are highly correlated and Dessens (1995) found a strong relationship of hail events and minimum temperature, it was decided to only use temperature (min) in this work.

Predictors will be referred to from here on as follows: Temperature (min) as *temp*, Precipitation as *precip*, PISR as *srad*, tree age as *age* and elevation as *elevation*.

To check for high correlation within the predictors, the Pearson correlation coefficient was calculated for all predictor pairs. For more information, scatterplots of each variable pair and the histograms of each predictor were carried out. Additionally, the VIF was calculated for each predictor. The VIF is calculated iteratively by

$$VIF = \frac{1}{1 - R^2} \tag{4.1}$$

for each predictor variable. R-squared (R^2) returns the amount of variance explained by a model in a range from 0-1 (De Veaux, Velleman, & Bock, 2011). The concept behind the VIF calculation is the following: In each iteration a different predictor is set as the response variable in the calculated regression. Assuming a high correlation between variable x_1 and x_2, R^2 of the regression analysis will be high resulting in a high VIF value. Although in statistics there is no hard threshold at which a variable should be dropped, VIFs exceeding a value of 5 are often considered too high (Zuur, Ieno, & Smith, 2007).

When facing fairly high Pearson correlation coefficients (i.e. > 0.8) (Figure 5.4) and VIF values for predictors (Table 5.1), one solution is to drop a variable from the list of predictors and recheck on the VIF values. After dropping *elevation* from the list of predictors, lower VIF values were observed for each predictor (Table 5.1). Therefore it was decided to drop $elevation$ from the list of predictors for all further analyses.

A descriptive statistical overview of the final predictors (*temp*, *precip*, *srad* & *age*) is provided in subsection 5.2.2. Uncommon units for *precip* (m/m^2) and *srad* (hW/m^2) were chosen to reduce convergence errors in the statistical models (especially in GAMMs). Categorical variables *year* and *evaluator* were not chosen as predictors because they represent grouping structures in the surveyed data. These were included as random effects into the model and are further evaluated in subsection 4.4.4.

4.4. Statistical Model Theory

4.4.1. Linear Models

Although simple linear models are not suited to model binary responses, they set the base for all further statistical models used in this work. This section introduces concepts which are extended by Generalized Linear Model (GLM)s and GAMs.

Linear Model (LM)s attempt to draw the best straight line throughout data points with the attempt of minimizing the residuals (difference between predicted points and actual data points) at every location (De Veaux et al., 2011). In mathematics, a straight line equation is expressed as

$$y = mx + b \tag{4.2}$$

In statistics, this equation is written slightly differently:

$$\hat{y} = b_0 + b_1 x \tag{4.3}$$

Here, $\hat{y}$ means that all values which form the specific formula coefficients (b_0 and b_1), are predicted values and not real data points. The better the predicted points of the model, the closer the actual data points will lie around them. The terms b_0 and b_1 represent the y-intercept and the slope of the predicted line, respectively (De Veaux et al., 2011; Wood, 2006).

A LM assumes the relationship of two variables to be perfectly straight. As this only applies to special cases in practice, Equation 4.3 can also be written as follows:

$$Data = Model + Residual \tag{4.4}$$

$$Residual = Data - Model \tag{4.5}$$

$$\epsilon = y - \hat{y} \tag{4.6}$$

Residuals (ϵ) represent the difference of the predicted model points to the actual data points. In other words, residuals show what the model missed and how good/bad it describes the underlying data. Hence, residuals are used to measure the model fit using measures like R^2 or Root Mean Square Error (RMSE). Residuals are also used to check if grouping trends exist in the data (e.g. autocorrelation, random effects) (De Veaux et al., 2011; Wood, 2006). This topic will be covered in more detail in subsection 4.4.5 (Spatial Autocorrelation) and subsection 4.4.4 (Random Effects).

4.4.2. Generalized Linear Models

GLMs, as introduced by Nelder and Wedderburn (1972) as an extension of LMs, "allow for response distributions other than normal, and for a degree of non-linearity in the model structure" (Wood, 2006). GLMs are defined as

$$g(\mu_i) = X_i\beta + \epsilon \tag{4.7}$$

where g is a smooth monotonic "link function", μ_i is the predicted value, "X_i is the i^{th} row of a model matrix and β is a vector of unknown parameters" (Wood, 2006). GLMs make the assumption of the response values being independent and following "some exponential family distribution" like Poisson, Binomial, Gamma, Bernoulli, geometric or Normal distribution (Zuur et al., 2008). Zuur et al. (2008) break GLMs down to three essential parts:

- an assumption on the distribution of the response variable,
- specification of the systematic part as a function of the explanatory variables,
- the relationship between the mean value of the response and the systematic part, also called "link function".

Due to the fact that GLMs inherit from LMs, the general concepts and assumptions also apply to GLMs with a slight modification. While the general model formula is similar to LM, a link function g and a distribution of the response variable have to be defined. However, generalization comes with some cost: Model fitting is not done in one run but needs to be undertaken iteratively. Also, the distributional results which are used to make inferences are not exact anymore but rather approximate and "justified by large sample limiting results" (Wood, 2006).

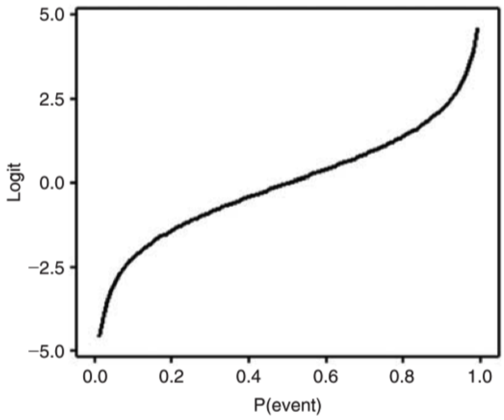

Figure 4.1.: Logit transformation of $P(event)$ of a logistic regression

In this study, the "binomial" link function will be used since the response variable "hail" is binary. In the case of a binary response variable, the specific GLM type is referred to as "logistic regression". In a case where the response variable has only two possible outcomes, methods returning possible numerical values from $[-\infty, \infty]$ do not make sense. Instead, the predicted values range between zero and one, inferring from the probability of case x to occur (Fielding, 2007). Logistic regression allows the predictors to be a mix of categorical and numeric ones. The statistical expression is written as

$$P(event) = \frac{1}{1 - e^{-z}} \tag{4.8}$$

where z is $b_0 + b_1x_1 + b_2x_2 + ...b_px_p$ and $P(event)$ is the probability that an event occurs. In this particular formula, the relationship of the response to its predictors is non-linear. To meet the condition of a linear model, the logistic equation can be transformed into a linear form using the binomial link function. Here, the probability is converted into "log odds" or "logit", where $logit[P(event)] = log[P(event)/P(noevent)]$ (Fielding, 2007). In the middle part of $P(event)$, roughly between 0.3 and 0.7, the relationship is linear (Figure 4.1). However, when $P(event)$ is located outside of this range, the response-predictor relationship turns into a non-linear one.

In the logit transformation, each one-unit change from a predictor is not directly associated with a change in $P(event)$ but first with a change in *log odds*, meaning $logit(P(event))$. This fact makes logistic regression outcomes more difficult to interpret than results from standard linear models such as multiple-linear regression. The probability of an event to occur is defined as the *odds ratio* $(odds/(1 + odds))$, where *odds* are calculated through the transformation of the *log odds* result of the coefficients of each predictor variable. An example is given in Fielding (2007), where the *log odds* of a random case study are

$$log\ odds = -2.7 + 2.5A - 3.7B + 1.8C \tag{4.9}$$

where A, B and C are assumed to be 1 in this example. The outcome of the *log odds* (here: -2.1) is then transformed to *odds* (= $e^{-2.1}$), resulting in a value of 0.1225. Following, the probability of an event to occur would be 0.1091 (= 10.91%) $(0.1225/(1 + 0.1225)$, following the logic of transforming odds to probabilities (probability = odds / (1 + odds)). The Odds Ratio (OR) is simply the ratio of two *odds* values. Such are often derived for one predictor while holding all others constant. ORs smaller than one refer to decreases in the *odds* as the predictor increases whereas ORs exceeding one correspond to an *odds* increase. If the OR is nearly one, changes in the predictor, which is not held constant and allowed to vary, does hardly affect changes in $P(event)$. The same applies for a *log odds* outcome of zero, since $e^{-0} = 1$. In summary, any one-unit change of a predictor (e.g. from 49 kg to 50 kg) will change the *log odds* outcome by its specific predictor coefficient and hence change the probability of an event to occur (Fielding, 2007).

As GLMs carry over the independence assumption of the observations from LMs, there might be cases where this assumption is violated. Examples for such cases are spatial or temporal autocorrelation of observations or underlying random effects in the data (e.g. different persons who acquired the data). While such phenomena are discussed in more detail in subsection 4.4.5 and subsection 4.4.4, it shall be noted that GLMs are referred to as GLMMs in the case when "correction factors" are put into the model formula to account for these effects in the data (Wood, 2006; Zuur et al., 2008).

When comparing different estimates of either odds or probabilities, odds are preferred since they are defined from $(0, \infty)$ while probabilities range between $(0, 1)$. Hence, when comparing different estimates of probabilities (also referred to as relative risk), cases may occur where specific ratios end up in probabilities > 1. Doing the same with odds would mean to calculate the OR, which is much more convenient for interpretation (especially for high ratio outcomes) due to its definition range (Zuur et al., 2008).

4.4.3. Generalized Additive Models

A GAM is an extension of a GLM which allows for non-linearity of predictors utilizing smooth functions. It was first introduced by T. Hastie and Tibshirani (1986). GAMs provide the ability to account for non-linear relationships of predictors which makes them highly flexible (Wood, 2006). The model formula is similar to the one for the GLM:

$$g(\mu_i) = X_i\theta + f_1(x_{1i}) + f_2(x_{2i}) + f_3(x_{3i}, x_{4i}) + \ldots + \epsilon \tag{4.10}$$

where:

g – smooth monotonic link function,
μ_i – response variable of some exponential family distribution,
X_i – row of the model matrix for any strictly parametric model components,
θ – the corresponding parameter vector,
ϵ – the residuals,
f_j – smooth functions of the covariates x_k

Smooth functions can be specific for every single predictor (e.g. $f_1(x_{1i})$) or for a group of predictors (e.g. $f_3(x_{3i}, x_{4i})$). It is also possible to define no smoothing function for a predictor. In this case, the relationship between response and predictor is assumed to be linear. When setting up a GAM, the type of smooth function (also referred to as "smooth class") and its degree (i.e. how smooth/non-linear the function is allowed to become) have to be set for every predictor. Additionally, each smooth class needs a specific penalty term, which is either single, multiple or quadratic, to control the degree of smoothness throughout the fitting process (Wood, 2006).

In this work the GAM implementation after Wood (2006) is used. There, four different smooth classes exist: *s*, *te*, *ti* and *t2*. The definition of a smooth class "is the basis used to represent the smooth function and quadratic penalty (or multiple penalties) used to penalize the basis coefficients in order to control the degree of smoothness" (Wood, 2006). The smooth classes *te*, *ti* and *t2* belong to the group of *tensor product smooths*. These classes are used when predictors, which use the same smooth type, exist in fundamentally different units. For example, if one predictor is measured in meters/hour and another one in light-years/nanoseconds. One option to solve this problem would be to use *tensor product smooths*. However, this case does not apply to the current study. Therefore, *tensor product smooths* will not be covered in more detail here (Wood, 2006).

All smoothing classes implemented by Wood (2006) are based on splines. Other approaches of GAM smoothing classes rely on *running mean smoother*, *B-spline smoother* (T. J. Hastie, 1992) (used in the *gam* function in R), *Locally Weighted Scatterplot Smoothing (LOESS)* or *Gaussian kernel smoother* (Zuur et al., 2008). Since there are even more mathematical ways of smoothing functions, this list does not claim to be complete.

As introduced above, the behavior of the smoothing function (when using penalized regression splines) is controlled by (i) the basis dimension and (ii) the smoothing base. The basis dimension of a smoothing function basically helps to reduce the computation time in comparison to full spline methods. The basis dimension can also be fixed, which in turn speeds up the modelling process a lot. However, then the artificial a priori assumption is made that the best degree of smoothing is ranging closely to the fixed value which will not end up with the best smoothing result in most of the cases (Wood, 2006). For the smoothing base, several options exist for practical convenience:

- thin plate regression splines
- duchon splines
- cubic regression splines
- splines on the sphere
- random effects
- markov Random Fields
- gaussian process smooths
- soap film smooths
- adaptive smoothers
- factor smooth interactions

While the offer of spline methods seems to be overwhelming at a first glance, Wood (2003) states that "there is a defined sense in which they (= thin plate regression splines) are the optimal smoother of any given basis dimension/rank". The details and properties of Thin Plate Regression Splines (TPRS) are covered in detail in Wood (2006). For practical use, the most important properties are outlined: TPRS have the ability to (i) work with any number of covariates, (ii) do not rely on 'knots' as many other spline methods do, (iii) are of isotropic character (= unaffected by the rotation of the coordinate system of the predictors) and (iiii) are 'low rank', which means that "they have fewer coefficients than there are data to smooth" (Wood, 2006).

A GAM is referred to as a GAMM if it accounts for underlying grouping effects such as autocorrelation or random effects (the same logic also applies to GLM/GLMM) (Zuur et al., 2008).

4.4.4. Random Effects

Random effects extend the models introduced in subsection 4.4.3 and subsection 4.4.2 (GLM and GAM) by a random component, which accounts for possible underlying trends in the observations. Taking the GLM formula as an example, the equation is written as

$$g(\mu_i) = X_i\beta + Zb + \epsilon \tag{4.11}$$

where b is a random vector containing the random effects and Z is a model matrix for the random effects (Wood, 2006). This model formulation including the random effects (with additional assumptions on the model parameters) goes back to Laird and Ware (1982).

In general a random effect can be characterized as a grouping structure inside a variable which is assumed to rely on randomness. This randomness can, for example, be introduced by different persons who collected survey data (some survey person may have introduced wrong measurements) or by different acquisition locations of data of the same type (air pollution measurements in a city). Sometimes it is possible to detect such grouping structures by investigating the variable closely (e.g. boxplots of each group), sometimes (e.g. for variables with thousands and more observations) it is hard to reveal a possible underlying grouping structure.

4.4.4.1. Random Intercept Model

When fitting a model with fixed predictors and one random effect, it is also referred to as a **random intercept model**. In the model output, a "random effect" and a "fixed effect" part is returned. The latter refers to the normal predictor output of the model. The "random effects" consists of "intercept" and "residual value". The latter refers to the residual variance of the random effect while the first value gives the variance of the random intercept. Referring to the example in Zuur et al. (2008), if a standard deviation value of 2.94 is returned, this results in

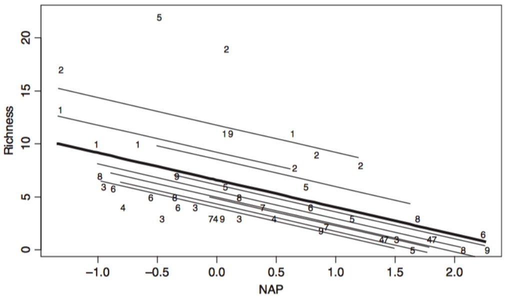

Figure 4.2.: Example of the variation of a *random intercept model*. *Richness* is the response and *NAP* the predictor. The thick line represents the fitted regression line while the labeled lines represent the variation introduced by a random effect with 9 levels. Source: (Zuur et al., 2008)

a random effect intercept variance of 8.64 (variance = (standard deviation)^2). This means that the intercept returned from the fixed effect part (= the predictors part) varies in both ways, positive and negative, by 8.64 due to the grouping structure specified by the random effect. This value is calculated by fitting the model for each grouping structure of the random effect. While the slope remains the same for all groups, the intercept varies by the random effect variable (Figure 4.2).

4.4.4.2. Random Intercept and Slope Model

While the *random intercept model* only changes the intercept but not the slope of the relationship (and by this implies that the relationship between the response and the predictor is the same for all random effect groups), this can be accounted for by using a **random intercept and slope model**. However, if there is a difference between the response and a categorical variable (here the random effect) this can also be accounted for by directly putting this variable into the model as a predictor instead of a random effect. Though, for variables with many groups, this would increase the degrees of freedom (and in turn the complexity) used by the model a lot. By setting this variable as a random effect, the model is able to account for the variation in intercept and slope but preserves a single slope value for the relationship (Zuur et al., 2008). The variance in intercept and slope can be visualized (Figure 4.3) and compared to the *random intercept model* using model evaluation measures such as the Akaike Information Criterion (AIC).

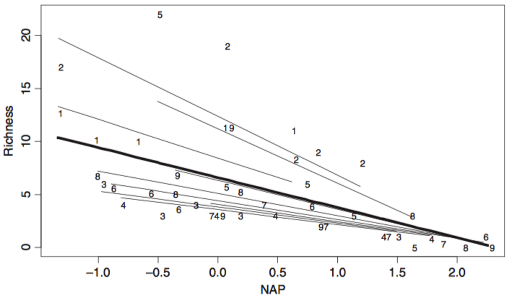

Figure 4.3.: Example of the variation of a *random intercept and slope model*. *Richness* is the response and *NAP* the predictor. The thick line represents the fitted regression line while the labeled lines represent the variation introduced by a random effect with 9 levels in interaction with *NAP*. Note that here the slope and the intercept of the "grouping regressions" differ compared to the thick line (while for the *random intercept model* in Figure 4.2 only the intercept is allowed to vary. Source: (Zuur et al., 2008)

4.4.4.3. Random Effects Model

If β is dropped from Equation 4.11 and the model only contains an intercept and a random component, the model is called a **random effects model** (Equation 4.12).

$$g(\mu_i) = \alpha + b_i + \epsilon_i \tag{4.12}$$

Here, the predictor is modeled as an intercept α and a random term b_i which is allowed to vary according to the number of its levels. Yet, this model is not used in this work and is therefore not explained in more detail (Zuur et al., 2008).

4.4.4.4. Induced/Intraclass correlation

While the standard deviation of the intercept and the residuals of the random effect are known and returned from the model output, the correlation between the different random effect groups is still unknown. By definition, the so called induced correlation (or co-variance) structure of the random effect is calculated as $\frac{d^2}{d^2+\sigma^2}$ where d is the intercept standard deviation and σ the standard deviation of the residuals of the random effect. This calculation applies to the *random intercept model*. The *induced correlation* is also called *intraclass correlation* and goes back to Snijders and Bosker (1991).

To keep this thesis concise, further details on *induced correlation* and *random effects* are not covered here. Calculation of the induced correlation for the *random intercept and slope model* goes back to Fitzmaurice, Laird, and Ware (2004) and takes the slope of the respective random effects into account. More details can be found in Zuur et al. (2008); Fitzmaurice et al. (2004). Standard error calculation of the intraclass correlation while accounting for the effective sample size (total sample size / number of groups of the random effect) is covered in more detail in Snijders and Bosker (1991); Zuur et al. (2008).

4.4.5. Spatial Autocorrelation

One of the most popular quotes goes back to Tobler (1970), stating that "everything is related to everything else, but near things are more related than distant things". This quote perfectly introduces one part of autocorrelation, namely the spatial case. If observations were collected from different spatial locations, the independence assumption of the data might be violated. Another case of autocorrelation is the temporal case. For example, running speed of people participating in a marathon are highly similar at the beginning of an event while the variance of this value increases over time up to certain maximum at which variance might decrease again. Accounting for such effects is essential in statistical model theory since otherwise the applied model is not modelling the relationship but rather an underlying trend in the data (Zuur et al., 2008). As the data in this work is not affected by temporal autocorrelation, this topic will not be covered in more detail. Methods to detect spatial autocorrelation will be presented in the following.

A possible violation of the independence assumption of observations can be checked by plotting the model residuals against their respective coordinates (Figure 4.4a). If the observations and in turn the residuals are independent, the plot should show no pattern of grouping between positive or negative residuals. However, this example shows a clear grouping which points to the assumption of an underlying spatial autocorrelation. To further investigate this issue, the empirical semivariogram of the model residuals can be calculated and visualized (Figure 4.4b). In a semivariogram, the semi-variance is plotted against distance. The semi-variance is calculated with the following equation (O'Sullivan & Urwin, 2010):

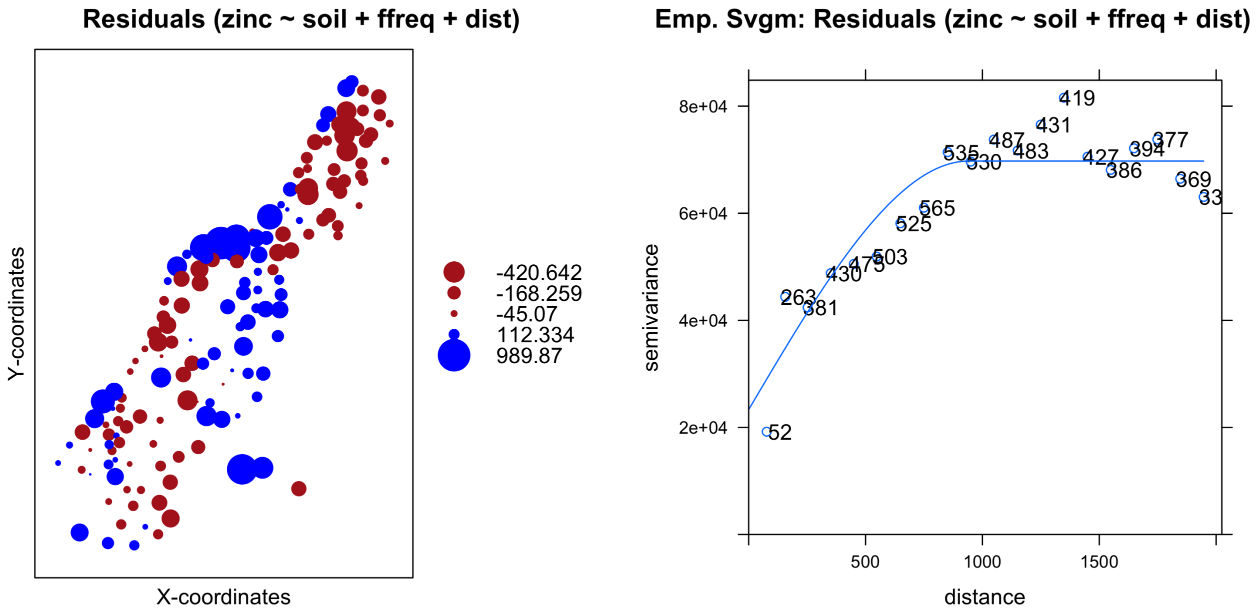

(a) Standardized residuals obtained by the linear regression model plotted versus their spatial coordinates. Red dotes are negative residuals, and blue dots are positive residuals

(b) Empirical semivariogram of the residuals of the linear regression model: Semi-variance against distance (m)

Figure 4.4.: Spatial autocorrelation check-plots. Response and predictors were chosen randomly for this example and no inferences should be made on their selection. Data source: R built-in 'meuse' data set (Rikken & van Rijn, 1993)

$$2\hat{y}(d) = \frac{1}{n(d)} \sum_{d_{ij}=d} (z_i - z_j)^2 \tag{4.13}$$

where:

$n(d)$ – number of observations per distance d,
z – observation.

In simple words, the sum of squares of all observation pairs (z_{ij}) for a given distance d is calculated and divided by their respective observations count for this distance (= labels in Figure 4.4a). The resulting semi-variance $\hat{y}$ is returned for the respective distance d. The "hat" denotes that the semi-variance is an estimate and not a real data point. The "two" in front of $\hat{y}$ goes back to the original geostatistical publication of Matheron (1963).

Several parameters describe a semivariogram: *range*, *sill* and *nugget*. The latter name originally goes back to the gold mining industry where it was common to find gold nuggets near a location where gold had already been discovered before. In statistics, "the nugget effect" describes the errors of measurement which are lying under the shortest sampling distance of which the semi-variance was calculated on. It is the semi-variance at which the fitted function crosses the y-axis (d = 0) (O'Sullivan & Urwin, 2010). The range is defined as the distance at which the semivariogram levels off. This means, at which distance d the semi-variance starts to saturate. In the example semivariogram (Figure 4.4a) the range is roughly located at a distance of 900 m. The *sill* is simply the semi-variance value at which the semi-variance levels off/saturates. A simple semivariogram as in Figure 4.4a assumes the spatial variation to be isotropic (i.e. equal in all directions). Yet, this is not always the case. Spatial autocorrelation sometimes only exists in one/multiple direction(s) or changes its behavior for different directions (e.g. spherical, Gaussian, exponential etc.). Although this case will not be covered in more detail here, it should be kept in mind when dealing with spatial autocorrelation (O'Sullivan & Urwin, 2010).

4.5. Model Specification

4.5.1. Generalized Linear Mixed Model

The general GLMM setup modelling hail as a function of temperature, precipitation, PISR and tree age while accounting for random effects (*year*, *eval*) was as follows:

$$g(hail_j) = b_{0j} + m_1 precip + m_2 temp + m_3 srad + m_4 age + \epsilon_j \tag{4.14}$$

$$b_{0j} = b_0 + v_{0j} \tag{4.15}$$

where:

g – Logit link function,

m_{1-4} – Slope coefficient

b_{0j} – overall mean intercept varying across random effect level (v_{0j})

b_0 – Fixed effects intercept

v_{0j} – Random intercept variation

ϵ_j – Residuals as a function of the respective random effect

While the inclusion of random effect structures in a model setup can be justified by the way the data is arranged/was collected, the need to account for grouping structures related to spatial autocorrelation can only be checked using the residuals of a model. Therefore, a simplified GLM was set up with the aim of checking on the residuals for possible spatial autocorrelation structures (Table 4.1). Visualizing the residuals ϵ of this GLM revealed a spatial autocorrelation up to a reported range of 1911 m (Figure 5.5). Hence, a spatial correlation structure using this range and a nugget effect of 0.03 was set up. Another GLMM was run to check on the residuals again and verify the effect of the inclusion of the spatial autocorrelation structure in the model (Figure 5.6). All further GLMMs were set up with the specific random effects while accounting for spatial autocorrelation (Table 4.1).

Year, *eval* (evaluator) and evaluator in every year (*year/eval*) were used as random effect structures in the models. Models 3-5 were evaluated regarding their magnitude of random effects while model setups (1-2) were just used to evaluate the need to account for spatial autocorrelation to ensure that the independence assumption of the residuals is not violated.

Table 4.1.: Overview of GLM & GLMM model setups

Index	**Type**	**Random effect**	**Spatial Autocorrelation**
1	GLM	-	-
2	GLMM	-	+
3	GLMM	Year	-
4	GLMM	Eval	-
5	GLMM	Year/Eval	-
6	GLMM	Year	+

Due to the findings of the reported magnitudes of intraclass correlation values of each random effect (Table 5.4), the final model setup GLMM (6) accounts for the strongest underlying grouping structure (*year*) and spatial autocorrelation. The model summary is reported in Table 5.5.

Using the model coefficients of GLMM (6), ORs corresponding to meaningful increases of each predictor (including 95% confidence intervals) and their change in odds were calculated (Table 5.6). For *precip*, *temp* and *srad* the meaningful increments correspond to 1/10 of their respective range. As this logic cannot be applied to *age* without rounding because the smallest increment step is one year, the increment step was set to ten years.

4.5.2. Generalized Additive Mixed Model

The same concept used for the GLMM setup (subsection 4.5.1) was used for the GAMM model setups. After checking for spatial autocorrelation in a GAM without random effects and autocorrelation structure (Figure 5.8), GAMMs with the observed autocorrelation structure (range: 5024 m, nugget: 0.25) were set up. The difference in model formulation compared to the GLM formula is the replacement of the linear slope coefficients by a smooth function for each predictor:

$$g(hail_j) = b_{0j} + f_1(precip) + f_2(temp) + f_3(srad) + f_4(age) + \epsilon_j \tag{4.16}$$

$$b_{0j} = b_0 + v_{0j} \tag{4.17}$$

where:

g – logit link function,

f_{1-4} – Smoothing function

b_{0j} – overall mean intercept varying across random effect level (v_{0j})

b_0 – Fixed effects intercept

v_{0j} – Random intercept variation

ϵ_j – Residuals as a function of the respective random effect

However, models containing random effect and autocorrelation structures (3-5) did not converge (Table 4.2). Therefore, GAMMs with random effects not accounting for the underlying spatial autocorrelation structure were fitted and evaluated (6-8).

Table 4.2.: Overview of GAM & GAMM model setups

Index	**Type**	**Random effect**	**Spatial Autocorrelation**	Note
1	GAM	-	-	
2	GAMM	-	+	
3	GAMM	Year	+	*DNC
4	GAMM	Eval	+	*DNC
5	GAMM	Year/Eval	+	*DNC
6	GAMM	Year	-	
7	GAMM	Eval	-	
8	GAMM	Year/Eval	-	

*DNC = Did Not Converge

Although the highest intraclass correlation was observed for the nested random effect *year/evaluation* (0.6) (Table 5.7), nearly all variation of this nesting contributes to random effect *year*. Hence, the decision was made to use GAMM (6), which only accounts for *year* as a random effect, to simplify the model setup by having only one random effect (*year*) instead of a nested random effect structure (*year/evaluation*).

Since GAMMs are non-linear, ORs corresponding to a continuous increment step are not feasible. Subsequently, ORs between selected predictor values were calculated while holding all other predictors constant at the same time (using the mean value of each predictor distribution). In detail, predicted log odds for two specific variable values were calculated (e.g. temp = 5°C and temp = temp = 6°C) while holding all other variables at their respective mean value. This ensures that the resulting difference in log odds only corresponds to the specified variable difference (Figure 5.9). Since logarithm usage converts multiplication to division, calculating the exponential value (reversal usage of logarithm) of the log odds difference results in OR. The same result can be achieved calculating probabilities for both setups and converting these into odds (odds = prob. / (1 - prob.)). Next, OR of both odds estimates can be calculated (Figure 5.9).

Additionally, ORs for continuous percentage intervals (20%) of each predictors distribution were calculated. The results provide an overview of the OR change across the whole value range of each predictor (Table 5.8).

4.6. Model Validation

Model validation is a big field in statistics and can be subdivided in (i) validation approaches and (ii) error measures. Due to the large amount of existing methods, only the validation approach used in this thesis, (spatial) Cross-Validation (CV), in combination with Area Under the Receiver Operating Characteristic Curve (AUROC) as the error measure will be presented.

4.6.1. (Spatial) Cross-Validation

The basic aim behind a statistical model is the ability to perform well on new observations, i.e. being generalizable. If a model adapts very well to a specific data set (either having very few misclassifications (classification case) or a small relative errors of predicted vs. data values (e.g. RMSE)), the model is said to be overfitting and will most likely perform poorly on a different data set. To test the performance of a model and compare it to many cases of "new observations", CV is often utilized. Here, the initial data set is split into k folds (most common: 5-10 folds). In every run, one fold is used as the validation set while all others are used for model training (Figure 4.5). The final error returned refers to the mean error of all fold runs. This procedure is repeated i times, usually 100 times and can be expressed as follows: (James, Witten, Hastie, & Tibshirani, 2013; T. Hastie, Tibshirani, & Friedman, 2009).

$$CV_{(k)} = \frac{1}{k} \sum_{i=1}^{k} error.measure_i \tag{4.18}$$

where $error.measure$ is either qualitative (e.g. AUROC) for classification cases or quantitative (e.g. RMSE) for models with a continuous response.
One famous special case of cross validation is to take all observations for training instead of one. This approach is called Leave-One-Out Cross-Validation (LOOCV). K-fold CV has computational advantages compared to LOOCV since considerably less folds are computed for the k-fold approach. Beside this fact, k-fold CV is known to give results which are more accurate due to a bias-variance trade-off. The more observations are devoted to the training set, the better the model will adapt to the specific data set. This leads to a higher chance of overfitting which would apply more to LOOCV. However, these estimates will only contain a low bias whereas k-fold CV

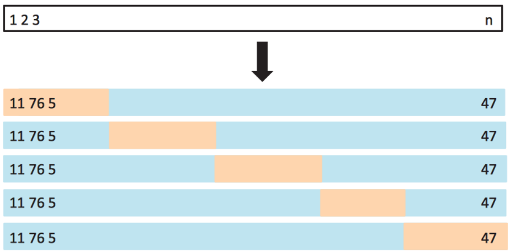

Figure 4.5.: Schematic display of 5-fold CV. Each fold serves as a validation set (beige) while all other folds are used for model training (blue). Source: James et al. (2013)

will show a higher bias in its estimates. Therefore, from the bias point of view, LOOCV is preferred (James et al., 2013; T. Hastie et al., 2009).

On the other hand, the low bias of each model run of LOOCV will result in outputs that are highly correlated with each other since the training set is almost identical (besides one observation). For k-fold CV, the training sets are more different in every run and the estimates will be less correlated. As a fact, highly correlated sets have higher variances than those who are not. This means that LOOCV estimates will have a low bias but a high variance whereas k-fold CV estimates will have a lower variance but a higher bias. To use a good trade-off, most often k-fold CV with k ranging from 5-10 is used in practice (James et al., 2013; T. Hastie et al., 2009).

When dealing with spatial data, autocorrelation of the observations is often present. When using the common CV approach, possible overfitting of the classifier to the training/calibration set will not be noted if the test/validation set is not independent (here: spatially correlated) of the training set. To tackle this issue, Brenning (2012) implemented the concept of spatial CV in the R-package 'sperrorest'. This approach splits the observations into sub-regions using clustering methods like "spatial k-means clustering" (Russ & Brenning, 2010). CV is then performed using these sub-regions. This ensures that training and validation sets are independent of each other.

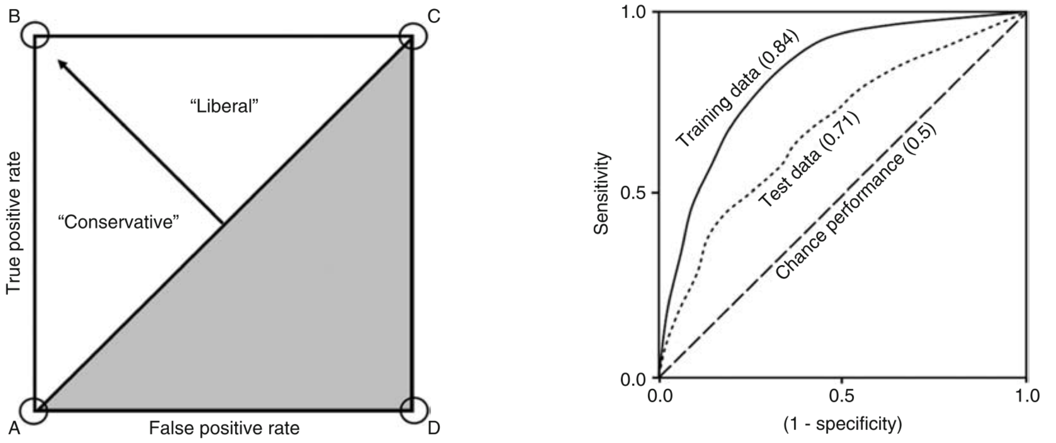

(a) Interpretation of ROC space. Source: Fawcett (2003); Fielding (2007)

(b) Example ROC curves (AUROC values in parentheses). Source: Fielding (2007)

Figure 4.6.: Interpretation of ROC space (a) and practical example (b)

4.6.2. AUROC

AUROC is a single value ranging between zero and one describing the ability of a classifier to distinguish between truly or falsely classified cases. It relies on the Receiver Operating Characteristic Curve (ROC) plot which shows the "trade-offs between the ability to identify correctly true positives and the costs associated with misclassifying negative cases as positives (false positives)" (Fielding, 2007). An important property of ROC plots is that they are robust to proportion changes of either positive or negative cases. Other abilities of ROC plots are listed in Fielding (2007) as follows:

- the effect of varying a decision threshold, i.e. the score used to split positive and negative cases,
- the variation in performance of a single classifier over a range of data sets,
- the relative performance of different classifiers on the same data set.

Point A and C represent extreme classifiers classifying all cases as either negative (A) or positive (C) (Figure 4.6a). Classifier B is the perfect classifier without any misclassifications. Point D is the opposite of Point B, classifying all cases exactly wrong. The diagonal line stands for the chance performance: In the long run, tossing a coin on the class belonging would result in a classifier with such a performance. Hence, any classifier ranging left from the diagonal is performing better than randomly guessing the classes. In summary: The closer a classifier is to point B, the better its performance (Fielding, 2007).

Classifiers which are closer to the "True positive rate" axis are of type "conservative", meaning they only do positive classifications if the evidence is high (Figure 4.6a). This results in very few cases which are classified positive but are in fact negative (false-positive errors) but also in many misclassifications of positives as negatives (if the evidence was too low to classify positives as a positive). Classifiers are called "liberal", if they perform the other way round as "conservative" ones: Classifying positive cases with weak evidence, resulting in a high false-positive rate (positive cases which are in fact negatives) (Fielding, 2007).

A classifier traditionally performs better on the training data than on the test data. The better it fits the training data, the worse will the fit be to other data sets. This trade-off can be visualized in ROC plots and compared using the AUROC values (here: 0.84 for the training set and 0.71 for the test set) (Figure 4.6b).

4.6.3. Validation Setup

To ensure comparability and show differences between spatial and non-spatial CV, for both models GAM and GLMM a spatial and non-spatial CV with ten folds and 100 repetitions was performed (Figure 4.7). The GLMM accounts for spatial autocorrelation and *year* as a random effect (Table 4.3). The inclusion of a spatial autocorrelation structure heavily increases model computation time. To be able to run the CV setups of the spatial models in an acceptable time, the R implementation of the 'sperrorest' package after Brenning (2012) was parallelized.

Although *year* was included in the model setup of the GLMM as a random effect, prediction was performed using the population mean intercept. For the GAMM setup, no spatial autocorrelation structure was included due to too high computation times and convergence problems. Also, *year* was not included as a random effect into the model but as a predictor to perform as an indicator variable (Table 4.3). Subsequently, *year* was fixed to "2009" for the prediction on the test set.

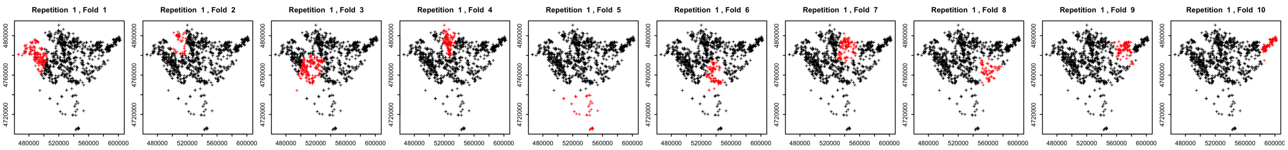

Figure 4.7.: Example of a spatial CV fold setup of the Basque region). Red colored observations represent the test set while model training is performed on the black colored observations, respectively.

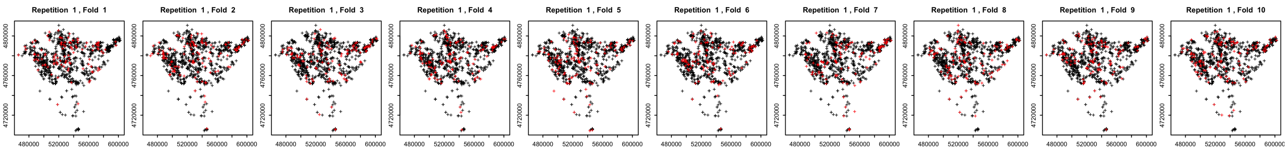

Figure 4.8.: Example of a non-spatial CV fold setup of the Basque region). Red colored observations represent the test set while model training is performed on the black colored observations, respectively.

Table 4.3.: Simplified (spatial) CV model setup of GLMM and GAM

Model	Formula	Grouping Structures
GLMM	hail ~precip + temp + srad + age	Sp. Autocorrelation (Range: 5024 m, Nugget: 0.25) Random Effect: *year*
GAM	hail ~precip + temp + srad + age + year	None

4.7. Prediction

Spatial prediction was performed on the selected GLMM and GAM models which were also used during validation (section 4.6). The following variables with a spatial resolution of 200 m were available from the Atlas Climatico data set (subsection 3.2.3) for the desired prediction area (Basque region): *Precip*, *temp* and *srad*. Since variable *age* was not available for the prediction data set, it was fixed to a value of 20 years for all raster cells. Subsequently, *year* was also fixed to "2009" for the prediction data set.

To evaluate the predicted probabilities, each predictor was plotted against the computed probabilities of each model (GLMM, GAM), respectively (Figure 5.13) (Figure 5.14) (Figure 5.15). Additionally, the predicted area (Basque region) was classified into four risk areas, representing different risk levels of occurring hail damage to trees ("very low", "low", "high", "very high") (Figure 5.16) (Figure 5.17). The base of this classification are the quantiles of the calculated probabilities. Descriptive statistics of probabilities and their variables were calculated and compared for every risk level (Table 5.11) (Figure 5.18). ORs between all risk classes were calculated to get an impression of the increase in odds of hail damage to trees between the classified risk areas.

All statistical analyses and preprocessing steps were conducted using the statistical software R (Version 3.3.1 - "Bug in your Hair") (R Core Team, 2016) and the following packages (alphabetic order): *cowplot* (Wilke, 2016), *dplyr* (Wickham & Francois, 2016), *ggplot2* (Wickham, 2009), *gridExtra* (Auguie, 2016), *gstat* (Pebesma, 2004), *MASS* (Venables & Ripley, 2002), *mgcv* (Wood, 2006), *nlme* (Pinheiro, Bates, DebRoy, Sarkar, & R Core Team, 2016), *plyr* (Wickham, 2011), *raster* (Hijmans, 2016), *rasterVis* (Perpiñán & Hijmans, 2016), *rgdal* (Bivand, Keitt, & Rowlingson, 2016), *sp* (Pebesma & Bivand, 2005), *stringr* (Wickham, 2015), *pacman* (Rinker & Kurkiewicz, 2015) and *tibble* (Wickham, Francois, & Müller, 2016). This thesis was written using LaTeX with the support of *knitr* (Y. Xie, 2016) and *rmarkdown* (Allaire et al., 2016) in RStudio (Version 0.99.903) (RStudio Team, 2015).

CHAPTER 5

RESULTS

5.1. Synoptic Weather Situation Related to Hail Occurrence

5.1.1. Hail by Time

The long term trend for the three stations shows that in Vitoria (mean = 11.9), on average, roughly three to four times more hail events per year occur than in Bilbao (mean = 4.4) and San Sebastian (mean = 3), respectively (Figure 5.1). Starting in 1973, a decreasing trend until 1994 can be observed for Vitoria. After reaching the low in 1994, hail occurrences increase again up to a value of 14 events until 2010 and stabilize afterwards.

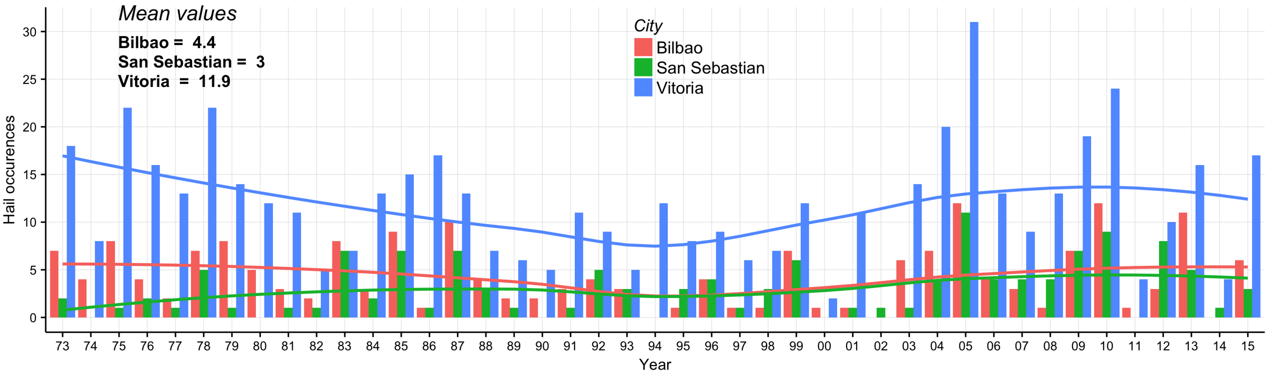

Figure 5.1.: Hail occurrences of Bilbao, San Sebastian and Vitoria for the years 1973 - 2015

For Bilbao, a very slight decline is observed from 1973 to 1994, followed by a slight increment of hail events up to a value of six for 2015. The trend after 1994 can be attributed to San Sebastian as well as the difference of showing a positive trend before the year 1994 rather than a negative one like for Bilbao.

Looking at the long term distribution of hail events by month for the three stations, the winter season (November - April) shows the highest values for all stations (Figure 5.2). Generally, all stations show an equal hailstorm-

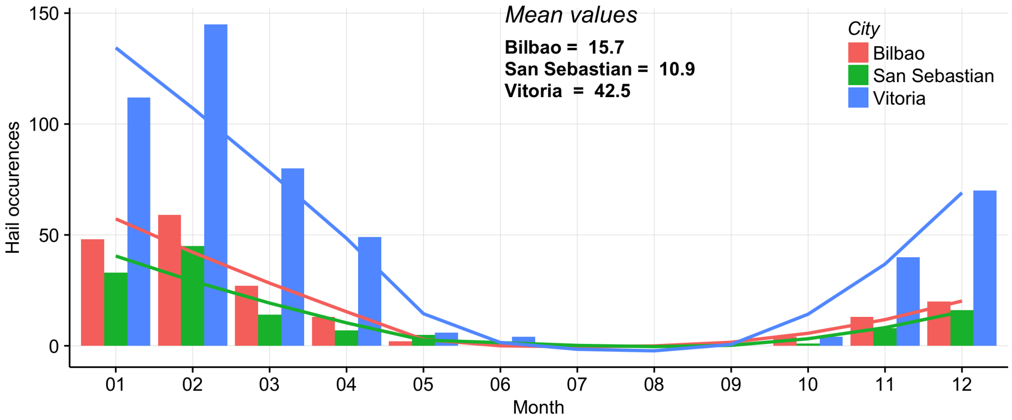

Figure 5.2.: Hail occurrences of Bilbao, San Sebastian and Vitoria by month for the time period 1973 - 2015

by-month distribution over the year, differing mostly in the absolute number of hail events. As already observed in the distribution of hail events by year (Figure 5.1), Vitoria shows the highest amount of hail events for all months, followed by Bilbao and San Sebastian. The peak month for all stations is February. During summer time, from June to September, almost no hail events are tracked for the years 1973 - 2015.

5.1.2. Hail Versus Climatic Variables

Non-linear relationships of hail occurrence versus all temperature variables are observed (Figure 5.3). Specifically, $TempMin$ shows a Gaussian-like distribution while $TempMean$ and $TempMax$ show an inverse variation function character.

The distribution of $PrecipTotal$ is highly skewed to the right due to the presence of many values ranging around 0-20 mm/m^2 precipitation. This results in a wide bin for the range for this class, ending up with three groups in total. An increase in hail probability with an increase of precipitation amount can be observed.

Regarding $WindSpeedMean$ and $WindSpeedMax$, roughly equal probabilities for all groups of x are observed, with a very slight hail probability increase towards higher wind speeds. However, these x groups consist of relatively few observations according to their bin width and should be treated with caution.

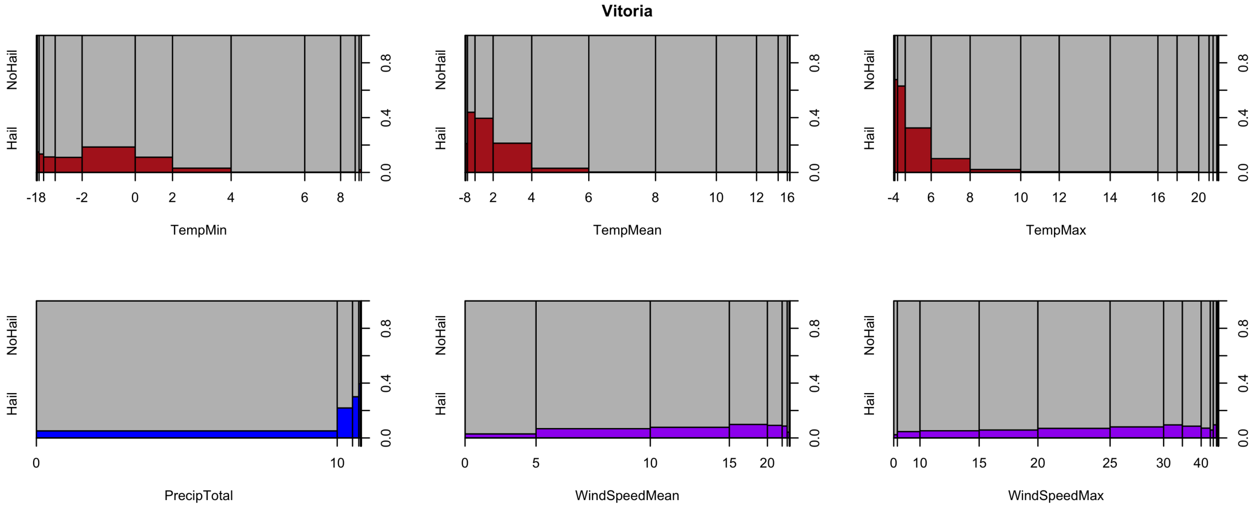

Figure 5.3.: Conditional density plots (spinograms here) of hail occurrence in relation to various climatic variables (daily observations) for the time period of 1973 - 2015 (November - April) of Vitoria. Y-axis shows the probability of hail occurrence for a given group of x. X-axis grouping according to histogram distribution of x. Temperature in °C, Precipitation in mm/m^2, Wind Speed in km/h

5.2. Statistical Modelling

5.2.1. Collinearity Analysis of Predictors

Variables *temp*, *srad* and *elevation* show a Gaussian distribution shape while the distribution of *precip* is skewed to the left (towards higher precipitation values) (Figure 5.4). *Age* shows a bi-modal distribution which is slightly skewed to the right, i.e. more observations ranging below the mean of 17.7 years (Table 5.2). A high Pearson correlation value between *Tmin* and *elevation* was observed (0.88) while all other predictor pairs showed correlation values of 0.42 (precip ~ elevation) and lower (Figure 5.4). High VIF values were returned for *temp* and *elevation*

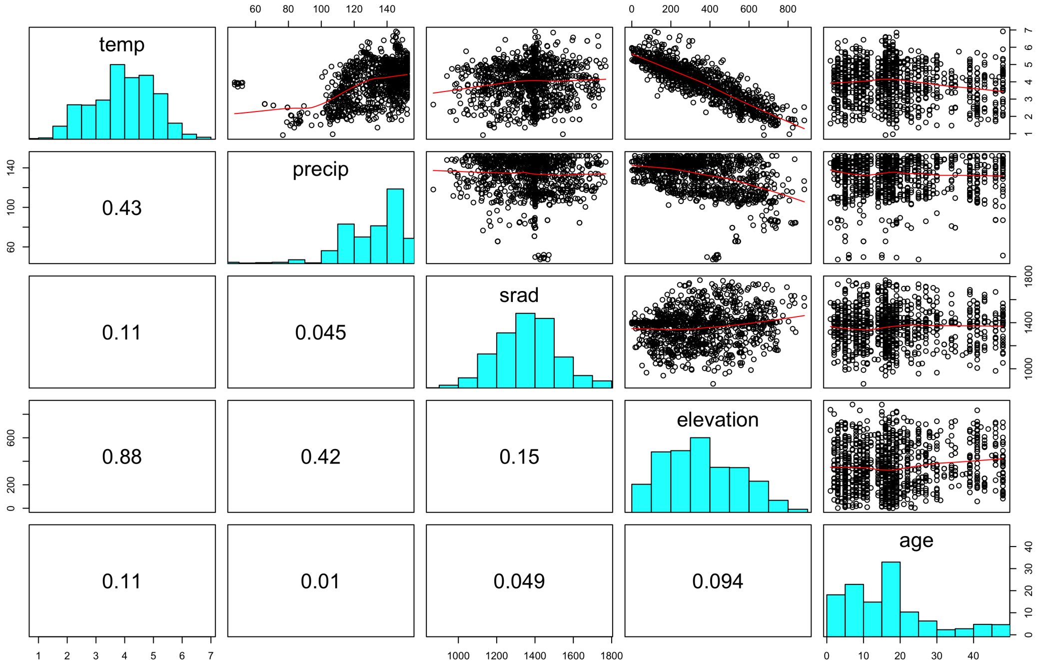

Figure 5.4.: Pearson correlations, histograms and scatterplots of predictors: Temperature (minimum), Precipitation amount, potential solar radiation, elevation and tree age.

(4.11 and 3.96). *Precip*, *srad* and *age* showed negligible small VIF values. After dropping *elevation* from the list of predictors, the VIF value of *temp* was reduced substantially (from 4.11 to 1.07) (Table 5.1).

Table 5.1.: Variance Inflation Factors (VIF) of all predictors (with and without *elevation*)

	temp	precip	srad	age	elevation
VIF (with elevation)	4.11	1.04	1.38	1.00	3.96
VIF (without elevation)	1.07	1.03	1.04	1.00	-

5.2.2. Descriptive Summaries of Numerical and Non-Numerical Variables

Table 5.2.: Descriptive summary statistics of numerical variables. Precipitation in m/m², Temperature in °C, PISR in hW/m², Tree Age in years. Statistics show Sample Size (**n**), Minimum (**Min**), 25% Quantile ($\mathbf{q_1}$), Median ($\tilde{\mathbf{x}}$), Mean ($\tilde{\mathbf{x}}$), 75% Quantile ($\mathbf{q_3}$), Maximum (**Max**), Inner-quartile range (**IQR**) and NA Count (**#NA**).

Variable	**n**	**Min**	$\mathbf{q_1}$	$\tilde{\mathbf{x}}$	$\bar{\mathbf{x}}$	$\mathbf{q_3}$	**Max**	**s**	**IQR**	**#NA**
precip	1168	0.047	0.119	0.138	0.132	0.146	0.152	0.019	0.028	0
temp	1168	0.917	3.250	3.983	3.964	4.783	6.917	1.080	1.533	0
srad	1168	0.009	0.012	0.014	0.014	0.014	0.018	0.002	0.002	0
age	1168	1.000	9.000	16.000	17.732	22.000	48.000	11.752	13.000	0

Sample counts of random effect variable *evaluation* show that 90% of all observations were surveyed by one person while the other 10% were acquired by "evaluator 2". Most observations were surveyed in year 2009 which corresponds to 42% of all observations (1168). Observations counts for the year 2010, 2011 and 2012 are 330, 143 and 210, respectively. Response variable *hail* shows a 20/80 (positives/negatives) ratio corresponding to surveyed hail-damages on trees (Table 5.3)

Table 5.3.: Descriptive summary statistics of non-numerical variables

Variable	**Levels**	**n**	%	∑ %
year	2009	494	42.3	42.3
	2010	330	28.2	70.5
	2011	143	12.2	82.8
	2012	201	17.2	100.0
	all	1168	100.0	
evaluation	1	1048	89.7	89.7
	2	120	10.3	100.0
	all	1168	100.0	
hail	0	929	79.5	79.5
	1	239	20.5	100.0
	all	1168	100.0	

5.2.3. Generalized Linear Mixed Model

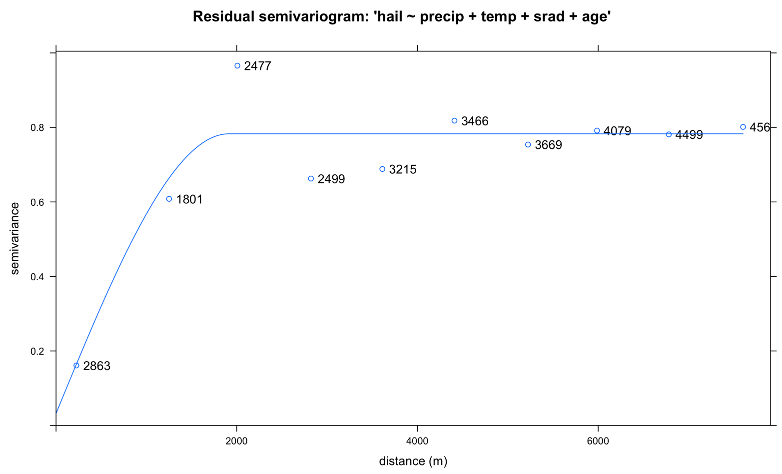

Figure 5.5.: Residual semivariogram of GLM (1)

Spatial autocorrelation up to a range of 1911 m was reported with a nugget effect of 0.03 for GLM (1). After accounting for spatial autocorrelation in the model, the Pearson residual semivariogram of GLMM (2) shows a higher nugget effect (0.4) with a reported range of 83000 m (Figure 5.6). The check for spatial autocorrelation was also made using spline correlograms and Morans I as the measure for autocorrelation. The closer Morans I is to the value of zero, the smaller the reported autocorrelation. A decrease in autocorrelation, especially in the range of 0-2000 m, was observed after accounting for it in the model (GLMM (2)) (Figure 5.7).

Standard deviation of intercept and residual of each random effect structure are shown in Table 5.4. Intraclass correlation is calculated as $\frac{d^2}{d^2+\sigma^2}$ where d is the intercept standard deviation and σ the standard deviation of the residuals of the random effect (see also subsubsection 4.4.4.4). While the intraclass correlation is (negligibly) small for *evaluation* and *year/evaluation* (0.11 and 0, respectively), a moderate value of 0.27 is reported for *year*.

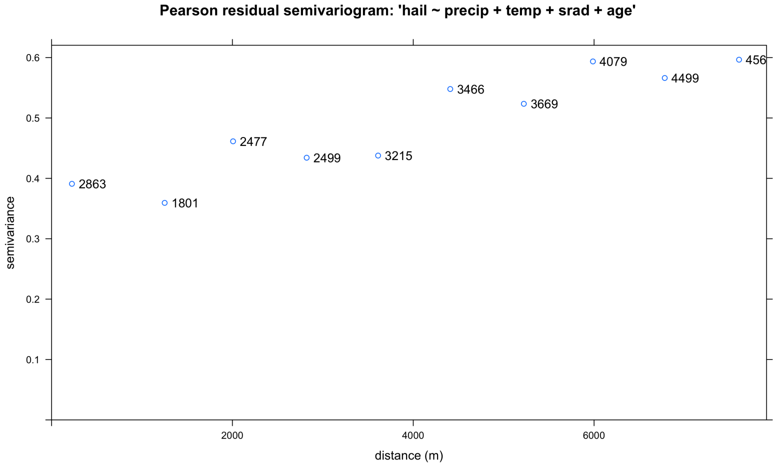

Figure 5.6.: Pearson residual semivariogram of GLMM (2)

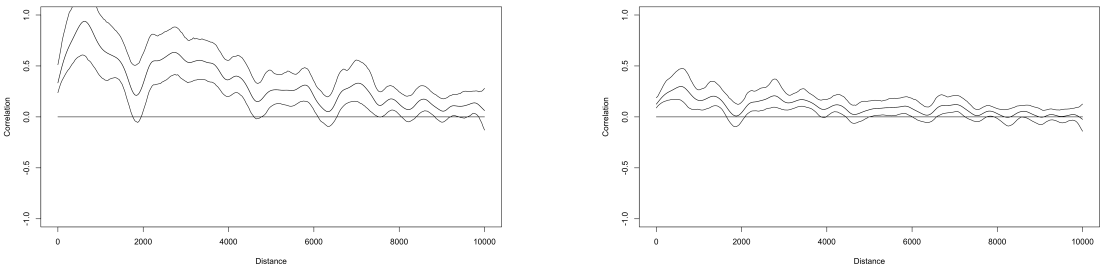

(a)

(b)

Figure 5.7.: Spline correlograms without (a) (GLM (1)) and with (b) (GLMM (2)) accounting for spatial autocorrelation in the model. Correlation of y-axis refers to Morans I autocorrelation measure. The closer the line is to zero, the lower the spatial autocorrelation for the respective distance. Upper and lower lines represent the 95% confidence interval.

Table 5.4.: Magnitude of random effects of GLMMs (3-5)

	year		evaluation		year/evaluation	
	Intercept	Residual	Intercept	Residual	Intercept	Residual
StdDev	1.13	1.84	0.44	1.23	0.00	1.84
Intraclass correlation	0.27		0.11		0	

Estimated model coefficients of fixed effects showed significance of predictors *precip temp* for a significance level of 5% (Table 5.5). *Srad* and *age* showed very high p-values (0.62 and 0.65, respectively) and did not come close being significant for the model. A very high standard error was reported for *srad* (58.16) in comparison to the respective slope estimate of *srad* (28.37). The reported intraclass correlation (0.45) was higher than for all models using only random effects and no spatial autocorrelation (3-5) for which the highest reported value was 0.27 (Table 5.4). Year 2012 was reported to have the highest negative intercept shift (-1.7) while year 2009 showed the highest positive shift (1.26). Years 2010 and 2011 had only small positive influences on the intercept shift (0.21 and 0.23 respectively). Eight degrees of freedom were used by the model.

Highest OR was reported for *precip* with 91% increase in odds for an increment of 0.0105 m/m^2 (Table 5.6).

Predictor *temp* showed an increase in odds of 16% for hail-damage on trees based on an increment of 0.6°C. Non-significant predictors *srad* & *age* showed negligibly small increases in odds (3% & 4%) in combination with an increment of 0.0009 hW/m^2 and 10 years, respectively.

		Value	Std.Error	DF	p-value
FE[a]	Intercept	-11.7769	1.5721	1160	<0.001
	precip	61.5651	8.4844	1160	<0.001
	temp	0.2502	0.1066	1160	0.0191
	srad	28.3710	58.1599	1160	0.6258
	age	0.0035	0.0080	1160	0.6596
RE[b]		StDev (intercept)	StDev (resid.)	Intraclass correlation	
		1.1069	1.2278	0.45	
		2009: 1.2583	2010: 0.2130	2011: 0.2296	2012: -1.7010
SA[c]		Range		Nugget	
		329.0935		0.2517	

[a]FE = Fixed effects, [b]RE = Random effects, [c]SA = Spatial Autocorrelation

Table 5.5.: Estimated model coefficients, standard errors and p-values of fixed effects; Calculated intraclass correlation of random effects from standard deviation of intercept and residual and spatial autocorrelation structure of final GLMM (6) model.

Table 5.6.: Estimated odds ratios corresponding to meaningful increases in each of the predictor variables and 95% confidence intervals of estimated odds ratios for GLMM (6).

	Increment	Odds Ratio	Increment in odds	95% OR Confidence Interval (2.5% | 97.5%)
precip	0.0105 m/m^2	1.909	91%	1.746 | 2.087
temp	0.6 °C	1.162	16%	1.09 | 1.239
srad	0.0009 hW/m^2	1.026	3%	0.974 | 1.081
age	10 years	1.036	4%	0.956 | 1.122

5.2.4. Generalized Additive Mixed Model

The semivariogram of GAM (1) showed an reported autocorrelation range of 5024 m and a nugget effect of 0.25. Standard deviation of intercept and residual of each random effect structure are shown in Table 5.7. The intercept value of *year/evaluation* (1.23) is a combination of both single random effects (year & evaluation): While evaluation contributes only 0.0002, almost all variation is devoted to *year* (1.230). Although the intraclass correlation coefficient is small for *evaluation* (0.1), fairly high values of 0.58 and 0.6 are reported for random effect *year* and *year/evaluation*.

Predictors *precip*, *temp* and *age* showed a non-linear relationship to the response *hail* with all being significant at the 5% level (Figure 5.9, Table 5.8). The highest non-linearity was observed for *age* with estimated degree of freedom of 5.50. Predictor *srad* was estimated to be non-significant for the model with a linear relationship to *hail*.

Uncertainty of smooth estimates was observed to be relatively high for *precip* in the range of 0.05 m/m^2 to 0.10 m/m^2 and for *temp* between 1°C and 2°C while all other smooth parts were estimated with a high safety, especially

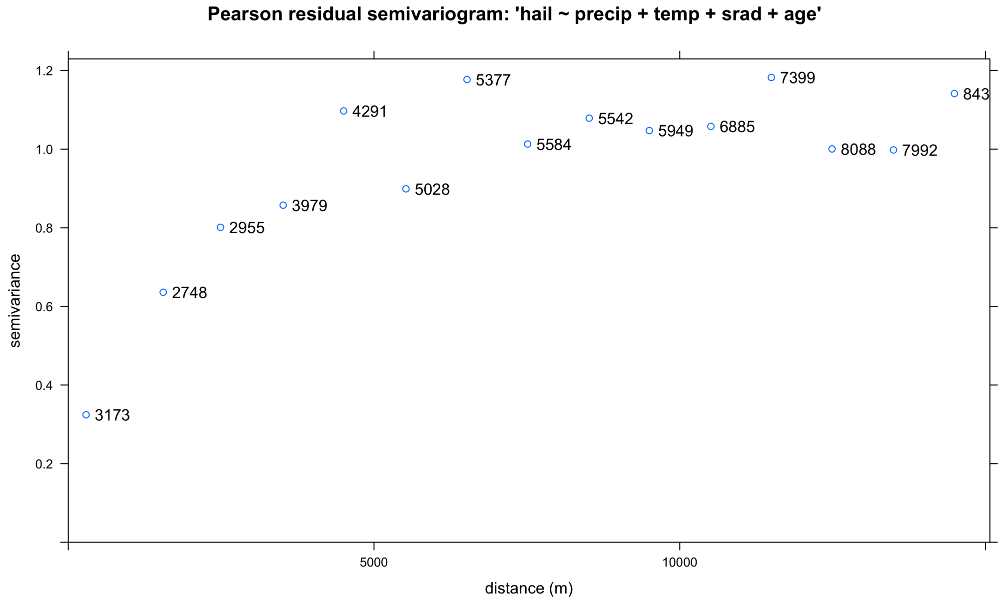

Figure 5.8.: Pearson residual semivariogram of GAM (1)

predictor *age* (Figure 5.9). Exemplary high ORs were observed for *temp* (OR = 13.43 for an increase from 5°C to 6°C) and *precip* (OR = 12.11 for an increase from 0.125 m/m^2 to 0.14 m/m^2). While *age* showed a small increase in odds (63%) from 10-year old to 20-year old trees, odds ratio of *srad* shows almost no change in odds (0.95) regarding a change from 0.012 hW/m^2 to 0.016 hW/m^2.
Highest OR increases were observed for the top end range (80%-100%) of *precip* (OR = 5.43 for an increase from 0.131 m/m^2 to 0.152 m/m^2) and *temp* (OR = 17.67 for an increase from 5.72 °C to 6.92 °C) (Table 5.8). ORs of *srad* showed a stable value of 0.98 throughout the calculated 20% intervals. A mixture of increases and decreases of ORs (min. OR = 0.44, max. OR = 1.90) was observed for predictor *age*.

5.3. (Spatial) Cross-Validation

Median AUROC values of both models were estimated higher for the non-spatial CV setup (e.g. Train (Spatial CV GLMM) = 0.66, Train (Non-Spatial CV GLMM) = 0.74) (Table 5.10). Highest StDev was observed for the test sets of the spatial CV GLMM setup (0.043) followed by its respective training sets (0.037). The highest training-test set AUROC difference was observed for the spatial CV GAM setup with a magnitude of 0.25 (Table 5.10 (Figure 5.10).

Table 5.7.: Magnitude of random effects of GAMMs (6-8)

	year		evaluation		year/evaluation	
	Intercept	Residual	Intercept	Residual	Intercept	Residual
StDev	1.17	1	0.34	1	1.23	1
Intraclass correlation	0.58		0.1		0.6	

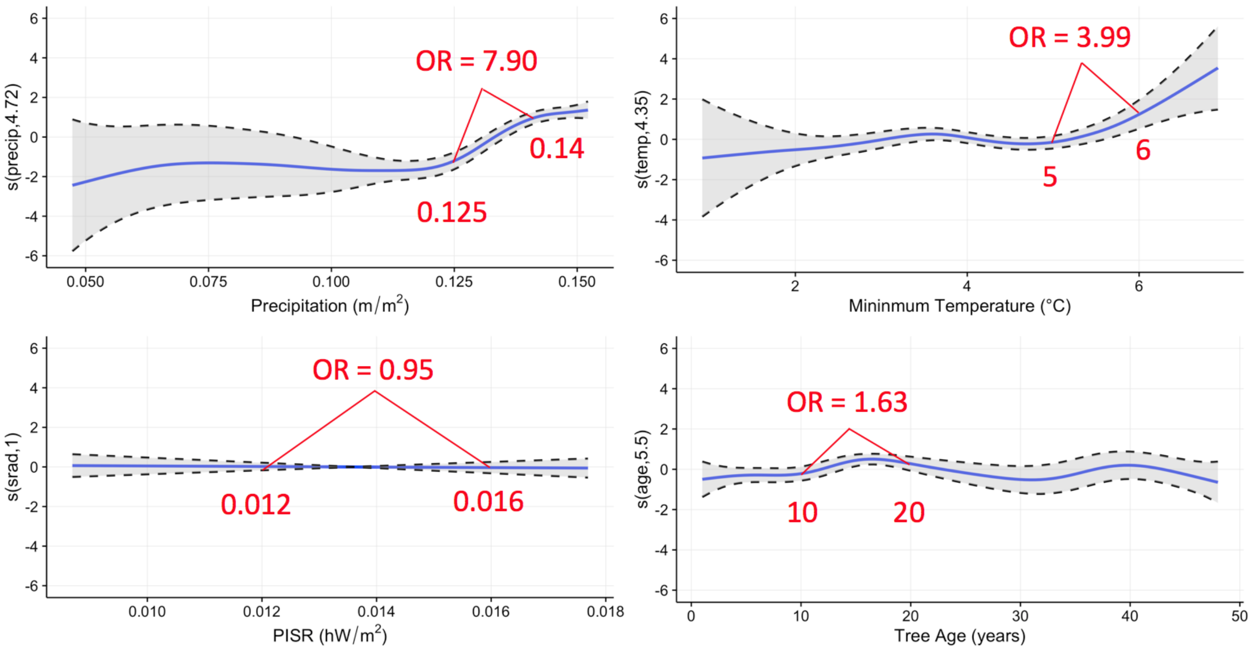

Figure 5.9.: Estimated smooth functions of final GAMM model (6) and their respective 95% confidence intervals. Odds ratios for selected increments of each predictor are given.

Table 5.8.: Smooth estimates and p-values of GAMM (6)

	edf*	p-value
s(precip)	4.72	< 2e-16
s(temp)	4.35	0.00109
s(srad)	1.00	0.80982
s(age)	5.50	0.00464

Table 5.9.: Odds ratios for 20% increase intervals corresponding to the respective distribution quantile values of each predictor

	0% - 20%	20% - 40%	40% - 60%	60% - 80%	80% - 100%
value (precip)	0.047 - 0.068	0.068 - 0.089	0.089 - 0.11	0.11 - 0.131	0.131 - 0.152
OR (precip)	2.92	0.94	0.76	3.98	5.43
value (temp)	0.91 - 2.12	2.12 - 3.32	3.32 - 4.52	4.52 - 5.72	5.72 - 6.92
OR (temp)	1.57	1.93	0.68	2.39	17.67
value (srad)	0.009 - 0.01	0.01 - 0.012	0.012 - 0.014	0.014 - 0.016	0.016 - 0.018
OR (srad)	0.98	0.98	0.98	0.98	0.98
value (age)	1 - 10.4	10.4 - 19.8	19.8 - 29.2	29.2 - 38.6	38.6 - 48
OR (age)	1.37	1.61	0.46	1.90	0.44

Table 5.10.: Descriptive statistics of (spatial) CV (10 folds, 100 repetitions) of GLMM and GAM

	GLMM				GAM			
	Spatial CV		Non-Spatial CV		Spatial CV		Non-Spatial CV	
	Train	Test	Train	Test	Train	Test	Train	Test
AUROC (median)	0.66	0.67	0.74	0.73	0.87	0.62	0.86	0.80
AUROC (StDev)	0.037	0.043	0.022	0.023	0.004	0.036	0.002	0.005

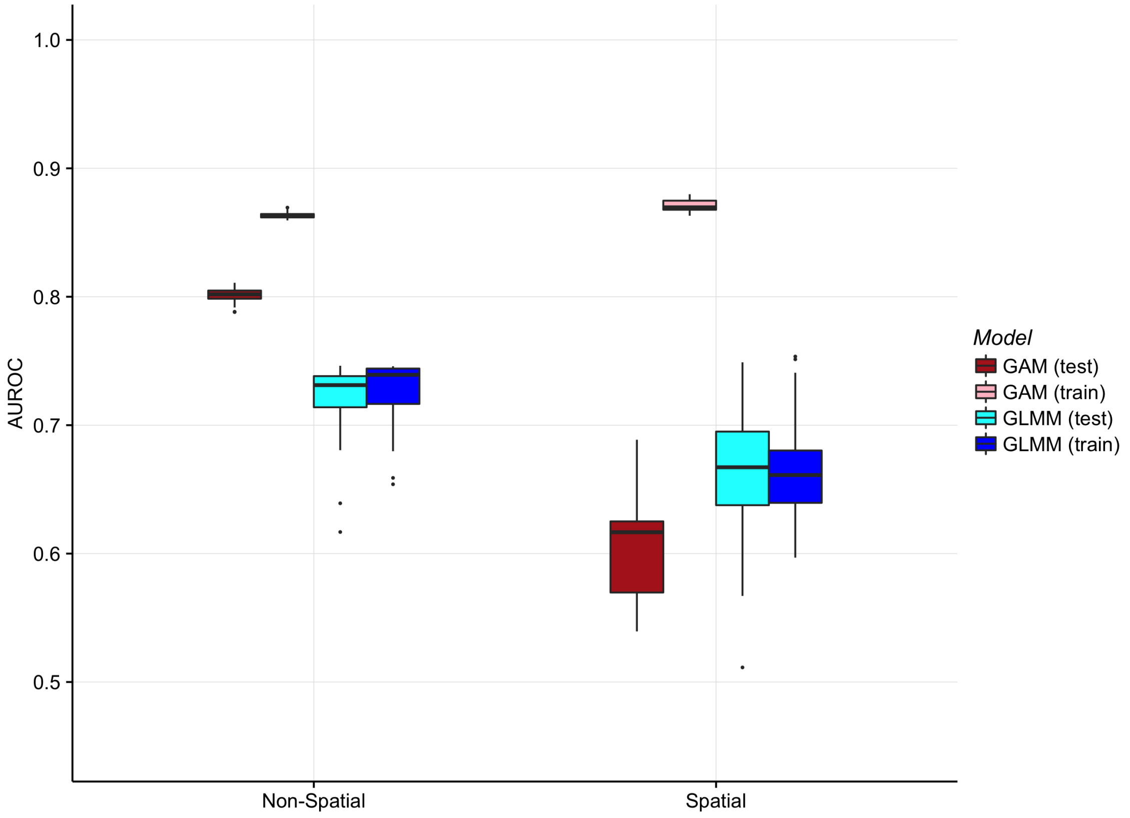

Figure 5.10.: Spatial and non-spatial CV (100 repetitions, 10 folds) AUROC distributions of GLMM and GAM

5.4. Prediction

5.4.1. Probability Estimates

The estimated probabilities of hail damage to trees of the GLMM show a smooth gradient with low values (< 20%) for the southern part of the study area ranging up to medium high estimates for the northeast of the study area (20% - 50%) (Figure 5.11). For the GAM, the diversity of estimated probabilities is higher than for the GLMM, spreading across the complete range of 0% - 100% (Figure 5.12). Highest values are observed for the northeastern part as well, while some regions in the south and western part show fairly high probabilities (~70%).

High Pearson correlation values are reported for precipitation vs. estimated probabilities (0.76 for GAM, 0.83 for GLMM) (Figure 5.13). The GAM shows a high uncertainty of estimated probabilities for low precipitation values. A non-linear trend is observed with a clear relationship of high estimated probabilities for high precipitation values. The GLMM shows mainly zero probabilities for low precipitation values up to 0.10 m/m^2 with a

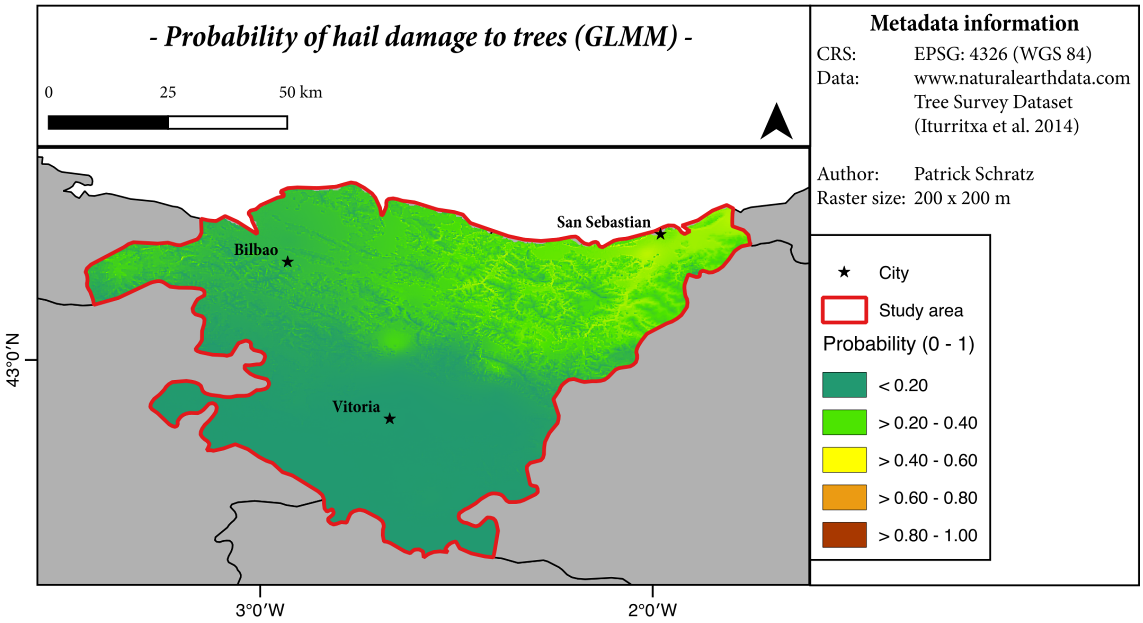

Figure 5.11.: Estimated probability of hail damages to trees of GLMM

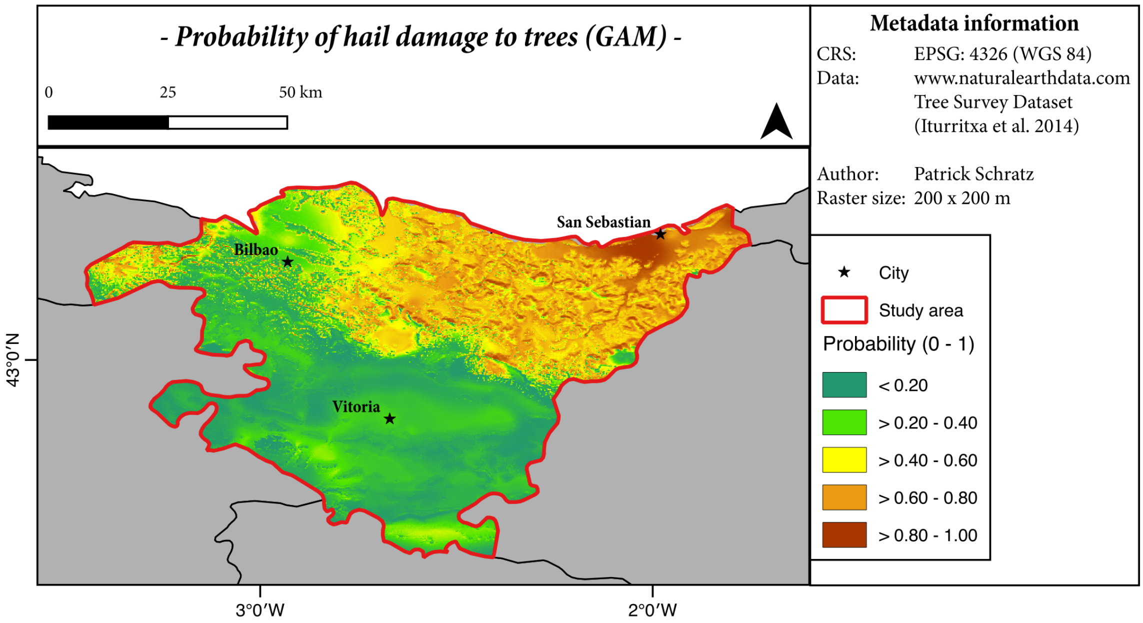

Figure 5.12.: Estimated probability of hail damages to trees of GAM

strong increase of probability for high precipitation values.

A similar trend is observed for temperature vs. probability with somewhat lower correlation values (0.59 (GAM), 0.67 (GLMM)). Here, a non-linear trend towards higher temperature values associated with higher probabilities of hail damage to trees is reported. Regarding PISR and estimated probabilities, the relationship is mainly randomly scattered over the complete PISR range with reported Pearson correlation values of -0.15 (GAM) and 0 (GLMM).

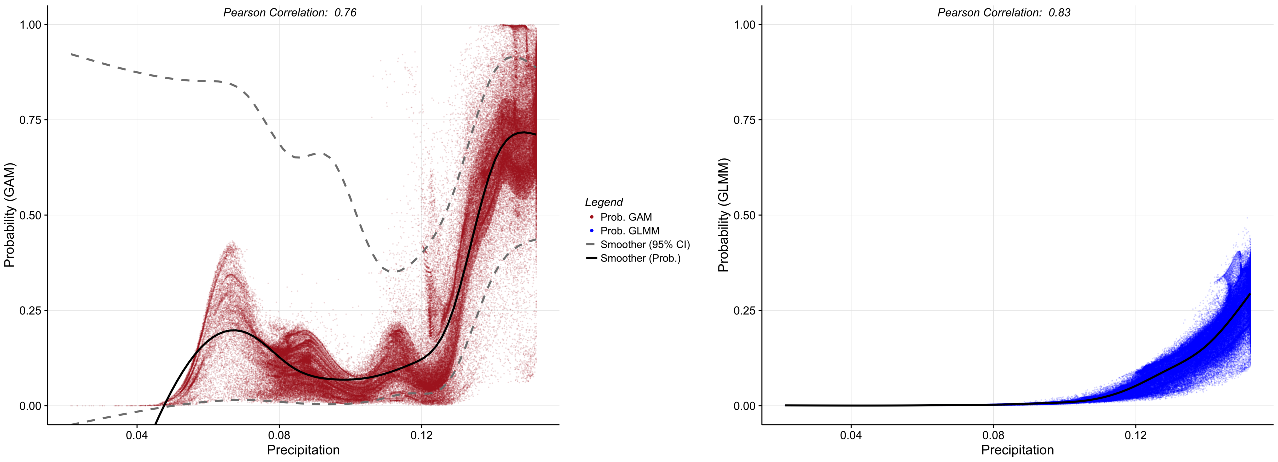

Figure 5.13.: Estimated probabilities of GAM and GLMM by precipitation

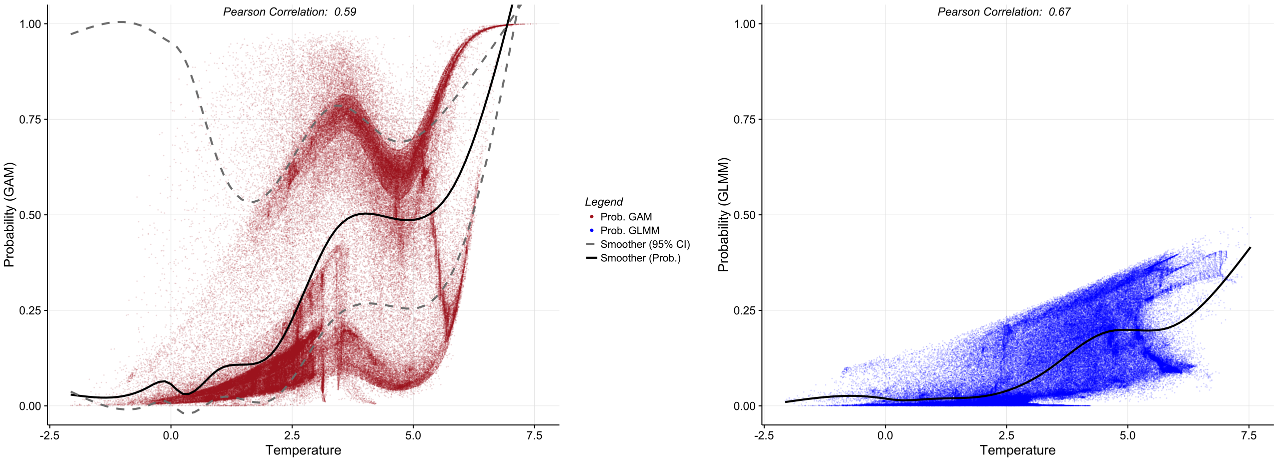

Figure 5.14.: Estimated probabilities of GAM and GLMM by temperature (min)

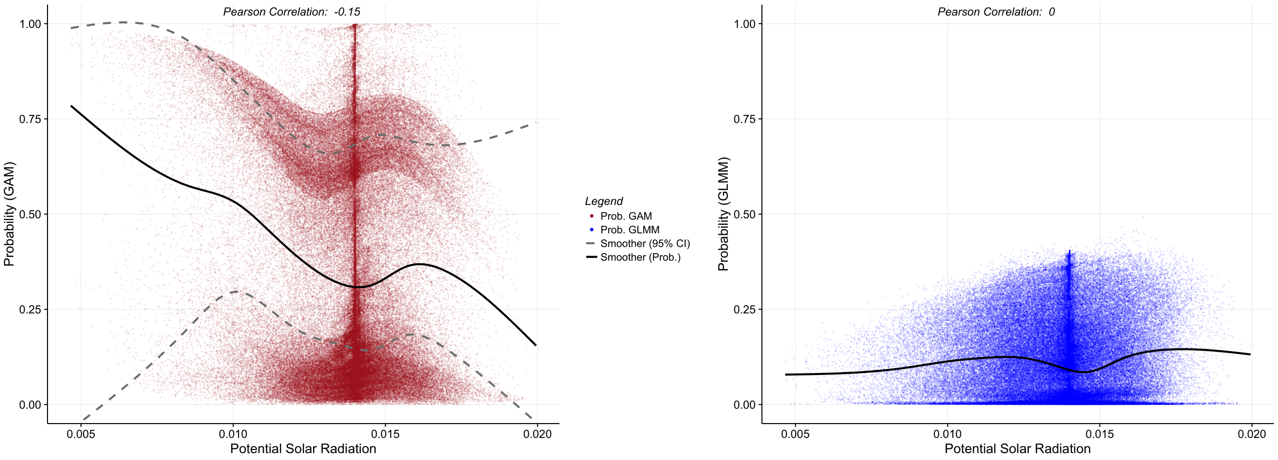

Figure 5.15.: Estimated probabilities of GAM and GLMM by PISR

5.4.2. Risk areas

A smooth gradient with mainly clear borders between the different probability quantiles can be observed for the GLMM (Figure 5.17). Class "Very-low" is located in the southern part of the study area with class "Low" directly adjoining the northern border. High risk areas are revealed in the northwestern part of the study area. The further northeast a region is located, the higher the risk of hail damage to trees becomes according to the GLMM estimate. The spatial distribution of the risk areas is more diverse for the GAM (Figure 5.16). While the general structure of low risk areas in the south up to high risk areas in the northeast can also be observed, the detailed distribution of the risk areas is more heterogeneous and mixed than for the GLMM. Some "high risk areas" are reported in the far southern part regarding the GAM estimate.

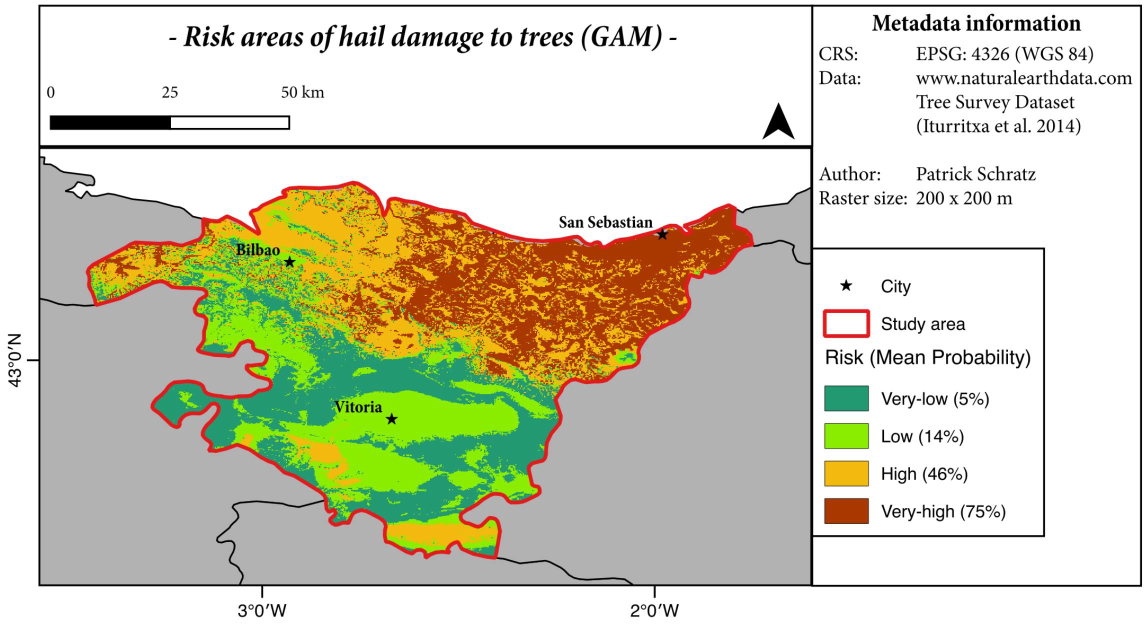

Figure 5.16.: Risk areas of hail damage to trees (GAM)

Besides a higher median of *precip* of class "Very Low" vs. "Low" for the GAM, continuous increases of *precip* and *temp* are observed within the different risk areas (Table 5.11) (Figure 5.18). *Precip* shows a more clear separation regarding its distributions across all risk classes for the GLMM than for the GAM where *precip* values are spread more heterogeneously within the risk areas. *Srad* is spread evenly across all risk areas with a negligible decrease towards higher risk areas (0.014 vs. 0.013 of "High" vs. "Very High") for the GLMM (Table 5.11). Since the risk

Table 5.11.: Descriptive statistics of risk areas for GAM and GLMM

	GLMM				GAM			
Risk area	Very Low	Low	High	Very High	Very Low	Low	High	Very High
Probability (mean, %)	0.2	3	12.5	26	5	14	46	75
Precip (mean, m/m^2)	0.07	0.11	0.13	0.15	0.1	0.1	0.13	0.15
Temp (mean, °C)	2.0	2.5	4.1	4.5	1.9	3.00	4.1	4.3
Srad (mean, hW/m^2)	0.014	0.014	0.014	0.014	0.014	0.014	0.014	0.013

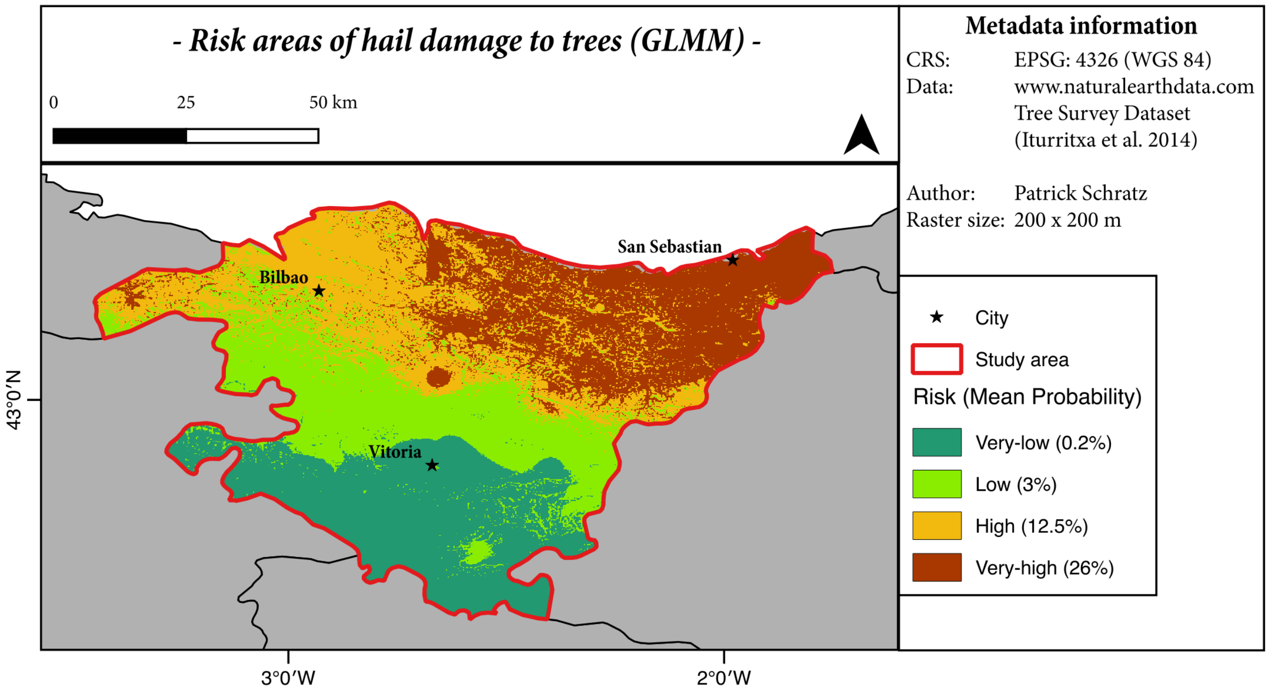

Figure 5.17.: Risk areas of hail damage to trees (GLMM)

area classes are based upon probability quartiles, their distributions are perfectly separated (Figure 5.18d). While both models show their highest distribution densities in regions with a probability < 0.1, the overall range of estimated probabilities is higher for the GAM than for the GLMM.

The highest reported increase in odds (15394%) is reported for the GAM between the risk classes "Very Low" and "Very High" (OR = 154.94). For the same classes, the GLMM estimates an 125 times higher risk of hail damages to trees. Also, the increase in risk of the GLMM between class "High" and "Very-High" (OR = 2.5) is four times smaller than estimated by the GAM (OR = 8.76). The GLMM shows higher increases in risks for class combinations "Very Low" to "Low" (OR = 10.9) and "Very Low" to "High" (OR = 50.22) compared to the GAM (OR = 3.07 and OR = 17.70, respectively).

Table 5.12.: Odds ratios between risk areas for GAM and GLMM. Percentage increase of odds in parentheses.

	GLMM			GAM		
Risk area	Low	High	Very High	Low	High	Very High
Very Low	10.90 (990)	50.22 (4922)	125.36 (12436)	3.07 (207)	17.70 (1670)	154.94 (15394)
Low	-	4.60 (360)	11.50 (1050)	-	5.77 (477)	50.47 (4947)
High		-	2.50 (150)		-	8.76 (776)

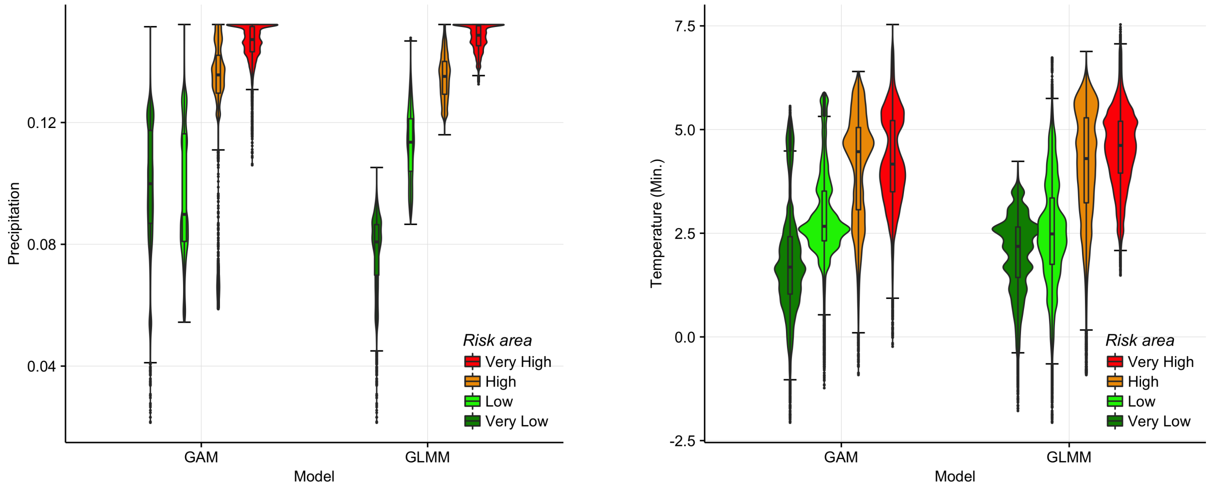

(a) Precipitation

(b) Temperature (min)

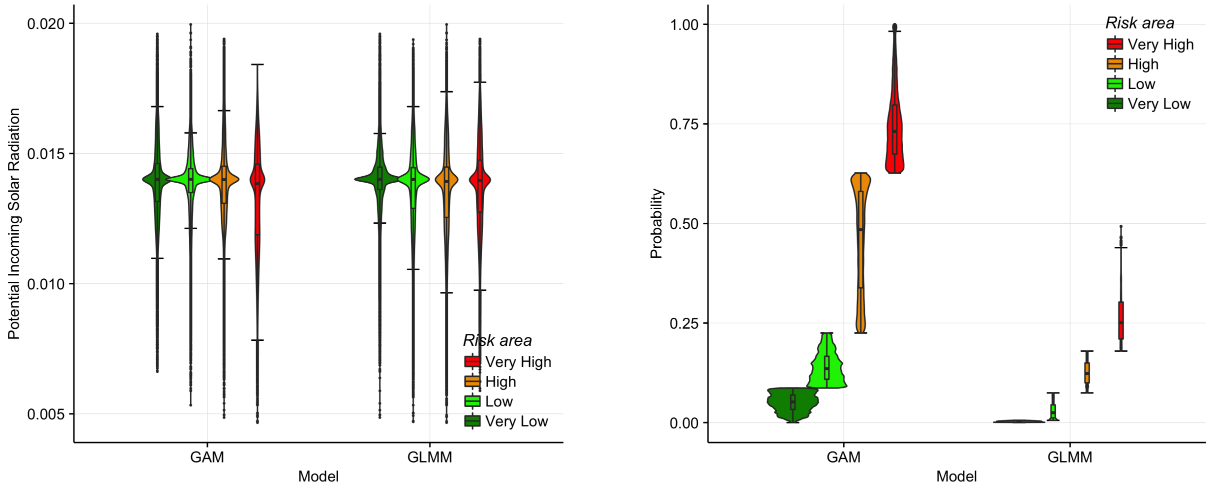

(c) PISR

(d) Probability

Figure 5.18.: Box- and violin plots showing areal statistics of precipitation, temperature, PISR and probability within the respective risk areas

CHAPTER 6

DISCUSSION

In this chapter, limitations in the undertaken steps of analysis are discussed and an interpretation of the results is given.

6.1. Note on Discarded Thesis Concept

The initial attempt of this work was to create probability maps of hail occurrence for the Basque region which then should have been compared to the actual hail damages tracked within the "Tree Survey data set" (subsection 3.2.4). The idea was to derive hail information from weather-radar data. Different methods to extract hail information from radar data exist. These and more information about scientific studies dealing with this topic are attached in Appendix B. However, the data could not be processed due to (i) a too small coverage time (about one year) with big data gaps for several months and (ii) an unclear preprocessing state of the data set which could not be clarified in a way to be able to safely process the given data. Point (i) would also have introduced high uncertainties regarding comparisons between monthly derived hail probabilities since possible events may have been missed due to data gaps. With respect to the time limitations of this work, it was decided to go with the hail variable within the "Tree Survey Data set" as the response variable. The mentioned problems with the data may be resolved in the future so that it can be used in future works.

6.2. Data Availability and Quality

While the synoptic situation related to hail occurrence was analyzed for a period of 40+ years using the GSOD data set (section 5.1), the analyses outcomes only represent three point locations within the study area (Bilbao, San Sebastian and Vitoria). As hail is a small-scale phenomenon, the ability to draw conclusions from the results of these three stations to other regions is limited. Nevertheless, to get a basic idea of hail occurrences related to various climatic variables on a synoptic scale, the data is sufficient.

The Atlas Climatico data set was used to extract variable information for the surveyed trees of the TSD. A spatial resolution of 200 m was sufficient for the measured variables used (precipitation, temperature and PISR) as such do not vary much within the given spatial extent of 200 m. The data is based on long term observations from years 1951 to 1999. Due to the impact of the ongoing climate change (IPCC, 2007, 2013), a difference of 17 years between the given data and nowadays introduces some bias compared to existing conditions today. While the influence of this difference is hard to measure, the introduced bias does not apply to all variables with the same magnitude. Unfortunately, no wind speed information was available and therefore the findings of wind speed vs. hail from the GSOD data set could not be integrated into the modelling part which might have improved the modelling result.

The TSD was used for the statistical modelling part. The spatial distribution of the surveyed trees has a higher concentration in the northern, flat part of the study area (Figure 3.5). This results in a fitted model adapting more to the climatic conditions in the north and being more uncertain about predictions for the southern part of the study area. Also, the distribution of species types should be mentioned here which is biased towards "Pinus radiata" (N = 945) with the next type being "Pinus pinaster" with 77 occurrences. Although different tree species should not make a huge difference to the model outcomes, the species component could be included in further studies to have a quantification of its effect. However, with respect to the total number of the most species types (< 50), possible outcomes need to be carefully interpreted. The influence of the different evaluators who surveyed the hail damages to trees and the different years of acquisition were accounted for in the model as random effects (Table 5.4) (Table 5.7). Their outcomes are further discussed in the section dealing with the model outcomes (subsection 6.3.3). Regarding the binary response variable of the data set, no information was given about how the evaluators decided on what classifies an observed damage being caused by hail. Additionally, no information was provided whether this damage occurred just recently or was missed during survey activities in the past years. In summary, no statement about the confidence of the modeled response variable can be made.

6.3. Statistical Modelling

6.3.1. Predictors And Model Setups

GLMs and GAMs with different setups were used to account best for the underlying grouping structures within the data (spatial autocorrelation, random effects). While GLMs assume the relationships between the response and predictor variables to be linear, GAMs were used in this work to explore and account for possible non-linear relationships. Non-linearity was found for predictors *precip* and *temp*, mainly at the higher end of their respective distribution range (Figure 5.9). Also, a non-linear relationship was reported for predictor *age* between 10 years and 50 years: While it could be assumed that older trees might be more suspicious to hail damage, the model reported that trees with an age of 20 years have a slightly higher probability of having hail damage than trees with an age of 10 years (OR = 1.63) or 30 years. Although such findings may be caused by randomness within the surveys, this result should be checked with a higher number of observations in future studies.

When looking at the results of the GAM, it needs to be considered that the model does not account for the underlying spatial autocorrelation (Figure 5.8). This is simply caused by the fact that the model setup which accounts for such did not converge. Various options were tried to reach convergence for the spatial GAMM model: Varying internal function parameters which help to reduce convergence errors, scaling down predictor units (*precip* from mm/m^2 to m/m^2, *srad* from kW/m^2 to hW/m^2) and removing/adding predictors. The author of the R package used (Wood, 2006) points out that convergence errors may occur easily "when explicitly modelling correlation in the data, probably because of the inherent difficulty in separating correlation from trend, when the trend model is itself rather complex". No convergence was reached and it was decided to use the GAMM which only accounts for the random effect structure *year* within the data for further analyses. Hence, the independence assumption of the residuals is violated for this model due to the presence of unaccounted spatial autocorrelation.

Regarding predictor selection of the models, VIFs were calculated and it was decided to drop elevation due to its high correlation with minimum temperature (0.88) (Figure 5.4) (Table 5.1). The decision to use minimum temperature instead of mean/max temperature was based on the findings of Dessens (1995) who detected a strong relationship of hail occurrence and minimum temperature.

Predictor selection in statistical models relies on basic understanding of the mechanics of the response variable. It was assumed that the response variable "surveyed hail damages to trees" (strongly) correlates with hail occurrence. Subsequently, predictor selection was performed on the underlying concepts of hail occurrence. It is known that hail events are related to certain climatic conditions (chapter 2). Subsequently, climatic variables were chosen to serve as predictors to model the response.

6.3.2. Validation and Prediction

While underlying random effect structures were accounted for in the models, a (spatial) cross-validation approach introduces problems with such structures. As the underlying grouping structure does not apply to the sub-regions of the cross-validation setup, it was decided to use the population mean intercept of the GLMM model for the CV approach. Since this is not technically possible for the GAMM model, the random effect variable *year* was fitted as an indicator variable to the model to account for the grouping structure. Subsequently, the value of the indicator class *year* was fixed for the prediction of the test set to "2009". Also, the spatial autocorrelation structure in the model does not apply exactly to each training/test set within the cross-validation setup. When validating models with spatial correlation structures, non-spatial CV approaches tend to introduce overfitting problems of the training set (Brenning, 2012). While this problem is reduced using spatial autocorrelation, the modeled autocorrelation is still different from the existing spatial autocorrelation within a specific CV fold. This bias needs to be considered in the CV results. However, its magnitude is hard to measure.

Similar problems regarding random effect structures arise for the spatial prediction of the trained models. Due to the different estimated intercepts of the random effect levels, a justification would be required why a specific level was taken for prediction. Since an argumentation in favor of one level cannot be given, the population mean intercept was taken for prediction. Additionally, predictor age was not available for spatial prediction. It was fixed to a value of 20 years and subsequently predicted probabilities/odds ratios do not account for the change in the hail/age relationship but assume it to be equal for all areas (age = 20 years). Spatially predicting such a biological variable is always problematic since information can only be gathered by repeated local surveys and not by using remote sensing and/or interpolation techniques.

6.3.3. Interpretation of Results

According to the long term measurements of the GSOD data set, hail mainly occurs during winter (November to April) in the Basque region (Figure 5.2). This is also reported by several other studies which investigated hail frequency along coasts (UK Met. Office, 2015; Sioutas, 2011). The important process is condensation which leads to the formation of severe storms causing hail. The fact that Vitoria shows the highest number of recorded hail events among the three cities (Vitoria, San Sebastian, Bilbao) with a mean hail occurrence of 42.5 events per year (more than twice as many as San Sebastian/Vitoria) contrasts to the estimated risk areas of hail damages to trees (Figure 5.16) (Figure 5.17). Here, Vitoria is located within the "Low" (GAM) and "Very Low" (GLMM) risk areas regarding hail damage to trees. A possible explanation for this is that most of the hail events happening in Vitoria do not cause damage to trees and therefore occur with a low intensity. This is supported by the fact that Vitoria is not located at the coast. Since most severe hail events occur along the coast due to the mentioned condensation processes, Vitoria is less likely to be hit by a severe storm event than San Sebastian or Bilbao. Another explanation could be the lower number of observations of the TSD data set in the region around Vitoria and the resulting higher uncertainty of probability estimates of hail damage to trees. Although this fact was not evaluated in particular, it is supported by the high uncertainties of probability estimates for areas with low precipitation (Figure 5.13) which are mainly located in areas with low number of observations (Figure 3.5). Since precipitation is decreasing from north to south within the study area (Figure 3.4), Vitoria is located within an area that has relatively low precipitation amounts (compared to the northern part of the study area).

Comparing the conditional density plots of the GSOD data (Figure 5.3), which are based on daily mean values of the respective variables against direct tracked hail events, with the calculated probabilities of hail damages to trees plotted against the predictors (*precip* and *temp*) of the TSD (Figure 5.13) (Figure 5.14), has to be done with caution: The response variables are just indirectly related (TSD response variable "hail damages to trees" is just a derivation of real hail events while the GSOD *hail* variables reports real hail events) and the aggregation of the variables is on a different scale (GSOD = daily mean, TSD = monthly mean). However, the trend of having higher precipitation values in combination with hail events can be observed for both setups. Regarding the minimum temperature results, most hail events seem to occur at a temperature range between -2°*C* and 0°*C*. In contrast, the highest probabilities of hail damages to trees were estimated for regions with a monthly minimum temperature of > 5°*C* of both models GLMM and GAM. This leads to the inference that many hail events in the region from -2°*C* and 0°*C* just occasionally cause hail damage to trees while hail events happening with a higher minimum temperature (> 5°*C*) come with a higher destructive energy.

The intraclass correlation reports of the modeled random effect structures (Table 5.4) (Table 5.7) showed a moderate grouping effect for the variable *year* (0.58 - GAM, 0.6 - GLM) giving information in which year the data was surveyed. The reason for such yearly grouping effects may relate to certain hail events which caused damage to trees in areas with similar properties of climatic variables in a specific year while in other years less hail related damages may have occurred. Only minor random grouping effects were reported for the different evaluators (0.1 - GAM, 0.11 - GLM). The reported intraclass correlation of *year/evaluation* for the GAM seems to be rather high (0.6). However, nearly all of its magnitude has to be attributed to *year* (0.58). This is attributed to the somewhat different calculation of the intraclass correlation for the GAM since the residual value is always fixed to a value of 1.

A spatial autocorrelation of the residuals was found in both GLMM and GAMM. Modelling such using semi-variograms, the affected range by spatial autocorrelation was reported to be 1911 m with a nugget effect of 0.03 (GLMM) and 5024 m with a nugget effect of 0.25 for the GAM, respectively. Spatial autocorrelation is common in statistical modelling when dealing with spatial data within certain distances. Revealing the magnitude of the spatial autocorrelation is the base to account for it afterwards in the model specifications to avoid violating the independence assumption of the residuals. However, the model setup of the GAMM accounting for the specified spatial autocorrelation did not converge (see also subsection 6.3.1). Hence all GAMM outcomes are affected by this assumption violation and should be treated with caution.

Significance to the 5% level was reported for predictors *precip* and *temp* for the GLMM (Table 5.5). For predictors *srad* and *age* only significance to the 10% level was achieved. This indication of importance for substantial influence on the model also relates to the estimated ORs for the respective predictors: The better the p-value, the higher the OR/increment in odds (Table 5.6). Since the increment steps of all predictors beside *age* were set to 10% of their respective range, comparisons of odds increments between the predictors are valid. Here, *precip* was clearly estimated to have the highest influence for a 10% change (OR = 1.91 for an increment of 0.0105 m/m^2) while a change 0.6°C was related to an increment in odds of 16% (OR = 1.16). Predictors *srad* and *age* showed negligibly small OR changes.

Direct comparisons between the OR outcomes of the GLMM and the GAMM cannot be drawn since the GAMM does not return coefficients which change the log odds for a specific unit change (like GLMs do). For the GAMM, a significance to the 5% level was reported for predictors *precip*, *temp* and *age*, suggesting an important interaction of tree age to possible hail damages to trees (Table 5.8). This relationship was reported not to be significant to the 5% level for the GLMM (Table 5.5). Also, the non-linear smoothing functions of the GAMM show an enhanced increase in OR for the last third of the predictor range for *precip* and *temp* (Figure 5.9). This indicates a strong relationship of high temperatures/precipitation amount with severe hail events causing hail damages to trees. Such findings corresponding to particular parts of a predictor range cannot be observed for linear models.

The GAMM shows problems when dealing with low *precip* or *temp* values indicated by the high 95% Confidence Interval (CI)s of the smoothing functions and the probability estimates vs. predictors (no CIs estimates are returned by the GLMM model due to the underlying "Penalized Quasi-Likelihood" fitting method) (Table 5.8) (Figure 5.13). This is assumed to be the main reason for the rather large gap between the calculated median AUROC values of training and test set (Table 5.10). The GAMM model overfits on the training set and is hardly able to deal with area properties mainly containing low *precip* or *temp* values. The mentioned gap of training and test set AUROCs (train(median) = 0.87, test(median = 0.62)) is well reported by the spatial CV setup while the non-spatial setup shows an unaccounted overfitting of the test set (median AUROC = 0.80). Overall, both GLMM and GAMM show a "poor" performance discriminating between the response of existing/non-existing hail damages to trees with reported median AUROCs ranging between 0.6 - 0.7 (referencing to the spatial CV test set results).

The resulting probabilities of GLMM and GAM show high distribution differences in their absolute magnitudes as well as in their respective counts. The GAM showed probabilities ranging from 0-1 with a high variation in estimated probability for the same predictor value combined with large 95% CIs (Figure 5.13) (Figure 5.14). Regarding the GLMM probability estimates, maximum values around 0.5 were reported with much lower probability variation per predictor value. A relatively large number of areas was predicted with a susceptibility of 0% of hail damages to trees, e.g. class "Very-Low" (Table 5.11). The difference between the models can be attributed (i) to the overfitting problems of the GAM in combination (ii) with the missing inclusion of the spatial autocorrelation structure in the model.

Hence, the risk areas of the GLMM show a much cleaner distinction for the GLMM as for the GAM (Figure 5.16) (Figure 5.17). Following the different distribution ranges of both models regarding their estimated probabilities, the calculated ORs between the risk areas are also more conservative for the GLMM than for the GAM. The latter reports an OR of 154.94 between class "Very Low" to "Very High" compared to an OR of 125.36 of the GLMM.

6.4. Major Findings

Different risk areas of hail damage to trees were identified. It was found that the northeastern part of the Basque region is most susceptible to possible tree damage (class "Very High"). The area with the second highest classified risk potential (class "High") is located in the northwestern part. Areas with a lower probability of being affected by hail causing tree damage are located starting from the horizontal center of the study area down to the southern end.

According to the calculated ORs of both models (Table 5.12), class "Very High" has at least 150% (GLMM) and up to 776% (GAM) increased odds compared to class "High". An increase in odds between 360% (GLMM) and 477% (GAM) from class "Low" to class "High" was observed. Class "Very Low" has almost no risk of damaged trees caused by hail with average probabilities of 0.2% (GLMM) and 5% (GAM) according to the prediction estimates of the fitted models. In summary, the differences between classes "Very Low" and "Low" and classes "High" and "Very High" are substantial in terms of susceptibility of damages trees caused by hail.

The spatial distribution of the risk areas relates highly to the spatial distribution of precipitation and minimum temperature in the study area. Both were found to be the two most important variables in the performed statistical analysis according to their respective OR changes (Table 5.6) (Table 5.9). A small influence (referring to ORs of both models) on possible damages was found for tree age. However, the relation does not show a stable increase with a higher tree age and needs to be interpreted with caution.

A steep increase was found for predictors *precip* and *temp* within the top third part of their value range (*precip*: 0.12 m/mm^2 - 0.15 m/mm^2, *temp*: 5°C - 6.5°C) of their respective GAMM smooth functions (Table 5.8). This indicates a high increase in probability of hail damage to trees when such climatic conditions appear.

With reported AUROC values of > 65% for the training set, the spatial and non-spatial CV setups indicate that the ability to model the response variable "hail damage to trees" using a GLMM/GAM with the available predictors is limited. Test set AUROCs of around 0.7 show a fair generalization of the GLMM. An AUROC gap of 0.25 between the test (0.62) and training set (0.87) of the GAM reveals overfitting to the training set.

6.5. Relation to Other Studies

When comparing results of this work to other studies, it has to be kept in mind that although the modeled response of many studies is related/derivated to/from hail occurrence/damage, it often differs in detail: In this work, hail damage to trees was analyzed. Almost no studies analyzing effects of hail damage to plants/trees exist. Subsequently, the possibility of comparing the modelling results of this study to others is limited. Most studies investigating hail focus on the atmospheric conditions and/or storm cloud properties to draw inferences on hail severity and frequency (Sánchez et al., 2013; Mallafré et al., 2009; Auer, 1994). Only few studies deal with the climatology of hail events (J. Webb et al., 2009; Piani, Crisci, Chiara, Maracchi, & Meneguzzo, 2005; Saa Requejo, Garcia Moreno, Diaz Alvarez, Burgaz, & Tarquis, 2011; Vinet, 2001). This mostly relates to missing or lacking time series of hailstorm data which makes the development of climatology models very problematic (Saa Requejo et al., 2011). Furthermore, due to the complex small-scale characteristics of hail, such models only apply to certain geographical regions and can hardly be transferred to other studies (chapter 2). However, rough comparisons between the geographical distribution of hail frequency and its inner-yearly occurrence in northern Spain and other countries can be made.

For France, Vinet (2001) found that "the frequency and intensity of hailstorms increase as one rises in altitude". While this finding corresponds with the higher hail frequency found for Vitoria (513 m) compared to Bilbao (21 m) and San Sebastian (32 m), hail intensity was inferred to be higher at the coast side than for the Cantabrian Range in this work (due to more surveyed hail damages at the coast than in the mountainous area). Vinet (2001) also points out that the regions affected most by hail in France relate to large-scale atmospheric circulations.

In Great Britain, J. Webb et al. (2009) observed that most hailstorms occur during summer time (May - August). The authors´ findings of a clustering of severe hailstorm events at the east- and south coast relate to the findings of this study, where highest risk areas of hail damage to trees were attributed to areas near the coastline although more (less severe) hail events occur upcountry

Saa Requejo et al. (2011) calculated an "loss-to-risk hail damage" index from hail insurance data which was compared to minimum and mean temperature values. While for some areas significant relationships between the index and a higher summer temperature were found, the authors point out that the results are mainly affected by the length of the time series and the dynamical characteristics of the studied areas (political provinces in Spain). These results somewhat differ from the results of this work for which a significant relationship between minimum temperature and hail damage to trees was found. However, the difference in response and available data needs to be considered here.

6.6. Future Research

To validate the findings of this work, the idea of linking hail damages of trees/plants to climatic variables like precipitation, temperature and wind speed should be transferred to other study areas and compared to the respective findings of this work. Such comparisons help to better understand and validate the link of regional climatic situations and synoptic weather situations to hail occurrence. Then, those results can be compared to distinct hail modelling using atmospheric variables to explore larger patterns and possible links between regional climate situations and atmospheric flow conditions.

More climatic variables can be used to further improve the models. Here, it was only possible to use precipitation, temperature and PISR. Relationships to variables such as wind speed, wind direction and air pressure could only be investigated in an exploitative way but not be used for modelling since they were not available spatially. Also, variables like PISR showing a similar mean value for the whole study area should be transformed in a way that reveals spatial differences. This may help to get such variables to have a significant impact on the models.

When investigating specific response variables like "hail damage to trees", it is important to not only include climatic variables but also components of the damaged good, here being trees. Revealing possible influences of tree health, tree species and effects like a grouping of trees, which may possibly save certain trees from getting damaged, are a possible way to improve further analyses.

This study provides a setup to explore patterns of hail damages to trees related to climatic variables and relate the synoptic weather situation of the Basque region to hail occurrence. While this is a first step, the results of this work (e.g. the risk areas and its ORs) need to be compared to studies of hail occurrence modelling in the desired area (Basque region, northern Spain). Methods and algorithms how to derive hail occurrence information from weather radar data are attached in Appendix B. It is important to find out at which kinetic energy level hail events have an impact on trees in general and on specific species. As such studies do not yet exist in this area due to the lack of in situ data like hail measurement systems (e.g. hailpads) in combination with surveys on hail damages to trees, it is important to tackle these problems in the future to support the creation of such scientific studies.

CHAPTER 7

CONCLUSION

Different risk areas of hail damage to trees in the Basque region in northern Spain were descried using linear and non-linear statistical learning methods (GLMM and GAMM). Utilizing climatic variables like precipitation, minimum temperature and characteristic tree information like tree age as predictors, a clear relationship of higher risk areas towards higher precipitation and temperature values was observed. Such risk areas help to improve the understanding and the drawing of links between hail damages to trees and infections of trees by pathogenic agents.

The calculated ORs between the risk areas vary for the GLMM and GAMM results. Almost no risk of hail damage to trees (probabilities between 0.2% and 5%) was estimated for risk class "Very Low" for both models while a tremendous increase in odds between this class and the highest risk class "Very High" was estimated (OR (GLMM): 125.36, OR (GAMM): 154.94).

The synoptic weather situation of hail occurrence in the Basque region was investigated using point information of three climate stations (Bilbao, San Sebastian and Vitoria). The long term data availability of 42 years helps to understand inner- and inter-yearly hail occurrence distributions throughout the Basque region. This knowledge also improves the understanding of the statistical model outcomes of both GLMM and GAMM. Due to the fact that hail preferably occurs during winter time in the Basque region, mean values of the predictors corresponding to this time frame were used within the modelling approach. The relationship between higher wind speed and hail occurrence which was found within the GSOD data set could not be included in the modelling and prediction setup because this variable was not available spatially. The inclusion of such could be one possibility to improve the models.

Surveyed hail damages to trees were used as the response variable. The models were trained on 1168 observations which are spatially distributed over the study area. Grouping structures in the data (random effects and spatial autocorrelation) were investigated and accounted for during model specification.

Spatial CV results ranging around 60% to 70% indicate that there is much room for improvement of the models. More variables explaining hail damage to trees need to be incorporated to create models with a higher ability of correctly discriminating between existing hail damage and no hail damage to trees.

The inclusion of the GAMM as a model type able to account for non-linear relationships of the response and the predictors provided the information of a non-linear behavior of predictors precipitation and minimum temperature, especially in the top third of their respective value range. These findings support the understanding of the occurrence of (severe) hail events in the Basque region.

The response of the models is a derivation of severe hail events causing damage to trees. To reveal possible misclassifications of such surveyed information and in turn to improve the statistical models, the results of this work need to be compared to studies investigating risk areas of direct severe hail events. Also, knowledge on a severity threshold of hail storms causing damage to (certain) tree species is highly sought after.

BIBLIOGRAPHY

Allaire, J., Cheng, J., Xie, Y., McPherson, J., Chang, W., Allen, J., … Hyndman, R. (2016). rmarkdown: Dynamic documents for R [Computer software manual]. (R package version 1.0) Retrieved from https://CRAN.R-project.org/package=rmarkdown

Amburn, S. A., & Wolf, P. L. (1997). VIL density as a hail indicator. *Weather and Forecasting*, *12*(3), 473-478. doi: 10.1175/1520-0434(1997)012<0473:VDAAHI>2.0.CO;2

Auer, A. H. (1994). Hail recognition through the combined use of radar reflectivity and cloud-top temperatures. *Monthly Weather Review*, *122*(9), 2218-2221. doi: 10.1175/1520-0493(1994)122<2218:HRTTCU>2.0.CO;2

Auguie, B. (2016). gridextra: Miscellaneous functions for "grid" graphics [Computer software manual]. (R package version 2.2.1) Retrieved from https://CRAN.R-project.org/package=gridExtra

Avery, T. E., & Burkhart, H. E. (2002). *Forest measurement* (5th ed.). New York: McGraw-Hill.

Aydin, K., Seliga, T. A., & Balaji, V. (1986). Remote sensing of hail with a dual linear polarization radar. *Journal of Climate and Applied Meteorology*, *25*(10), 1475-1484. doi: 10.1175/1520-0450(1986)025<1475:RSOHWA>2.0.CO;2

Barry, R. G., & Chorley, R. J. (1998). *Atmosphere, weather and climate* (7th ed.). Routledge, New York. Retrieved from http://samples.sainsburysebooks.co.uk/9781134721047_sample_482197.pdf

Battan, L. J. (1973). *Radar observation of the atmosphere*. University of Chicago Press. doi: 10.1002/qj.49709942229

Berthet, C., Dessens, J., & Sanchez, J. (2011). Regional and yearly variations of hail frequency and intensity in France. *Atmospheric Research*, *100*(4), 391 - 400. (5th European Conference on Severe Storms) doi: 10.1016/j.atmosres.2010.10.008

Berthet, C., Wesolek, E., Dessens, J., & Sanchez, J. (2013). Extreme hail day climatology in southwestern France. *Atmospheric Research*, *123*, 139 - 150. (6th European Conference on Severe Storms 2011. Palma de Mallorca, Spain) doi: 10.1016/j.atmosres.2012.10.007

Bigg, E. (1990). Measurement of concentrations of natural ice nuclei. *Atmospheric Research*, *25*(5), 397 - 408. doi: 10.1016/0169-8095(90)90024-7

Bivand, R., Keitt, T., & Rowlingson, B. (2016). rgdal: Bindings for the geospatial data abstraction library [Computer software manual]. (R package version 1.1-10) Retrieved from https://CRAN.R-project.org/package=rgdal

Bluestein, H. B., & Parks, C. R. (1983). A synoptic and photographic climatology of low-precipitation severe thunderstorms in the southern plains. *Monthly Weather Review*, *111*(10), 2034-2046. doi: 10.1175/1520-0493(1983)111<2034:ASAPCO>2.0.CO;2

Borja, K., & Collins, M. (2004). *Oceanography and marine environment of the Basque country*. Elsevier. Retrieved from http://www.beck-shop.de/Borja-Collins-Oceanography-Marine-Environment-Basque-Country/productview.aspx?product=606882

Botzen, W., Bouwer, L., & van den Bergh, J. (2010). Climate change and hailstorm damage: Empirical evidence and implications for agriculture and insurance. *Resource and Energy Economics*, *32*(3), 341–362. doi: 10.1016/j.reseneeco.2009.10.004

Brenning, A. (2012). Spatial cross-validation and bootstrap for the assessment of prediction rules in remote sensing: The R package sperrorest. In *2012 IEEE International Geoscience and Remote Sensing Symposium* (p. 5372-5375).

Brooks, H. E., Lee, J. W., & Craven, J. P. (2003). The spatial distribution of severe thunderstorm and tornado environments from global reanalysis data. *Atmospheric Research*, *67-68*, 73 - 94. (European Conference on Severe Storms 2002) doi: 10.1016/S0169-8095(03)00045-0

Browning, K., Frankhauser, J., Chalon, J.-P., Eccles, P., Strauch, R., Merrem, F., … Sand, W. (1976). Structure of an evolving hailstorm part V: Synthesis and implications for hail growth and hail suppression. *Monthly Weather Review*, *104*(5), 603-610. doi: 10.1175/1520-0493(1976)104<0603:SOAEHP>2.0.CO;2

Camuffo, D., & Sturaro, G. (2001). The climate of Rome and its action on monument decay. *Climate Research*, *16*, 145-155. doi: 10.3354/cr016145

Cecil, D. J., & Blankenship, C. B. (2012). Toward a global climatology of severe hailstorms as estimated by satellite passive microwave imagers. *Journal of Climate*, *25*(2), 687-703. doi: 10.1175/JCLI-D-11-00130.1

Changnon, S. A. (1970). Hailstreaks. *Journal of the Atmospheric Sciences*, *27*(1), 109-125. doi: 10.1175/1520-0469(1970)027<0109:H>2.0.CO;2

Changnon, S. A. (1971a). Hailfall characteristics related to crop damage. *Journal of Applied Meteorology*, *10*(2), 270-274. doi: 10.1175/1520-0450(1971)010<0270:HCRTCD>2.0.CO;2

Changnon, S. A. (1971b). Note on hailstone size distributions. *Journal of Applied Meteorology*, *10*(1), 168-170. doi: 10.1175/1520-0450(1971)010<0169:NOHSD>2.0.CO;2

Changnon, S. A. (1977). The scales of hail. *Journal of Applied Meteorology*, *16*(6), 626-648. doi: 10.1175/1520-0450(1977)016<0626:TSOH>2.0.CO;2

Changnon, S. A., & Changnon, D. (2000). Long-term fluctuations in hail incidences in the United States.

Journal of Climate, *13*(3), 658-664. doi: 10.1175/1520-0442(2000)013<0658:LTFIHI>2.0.CO;2

Changnon, S. A., Changnon, D., & Steven, S. D. (2009). *Hailstorms across the nation: An atlas about hail and its damages.* Illinois State Water Survey. Retrieved from http://hdl.handle.net/2142/15156

Dardy, H. D. (1973). Rayleigh scattering: Orientational motion in highly anisotropic liquids. *The Journal of Chemical Physics*, *59*(8), 4491. doi: 10.1063/1.1680649

de la Torre, A., Pessano, H., Hierro, R., Santos, J., Llamedo, P., & Alexander, P. (2015). The influence of topography on vertical velocity of air in relation to severe storms near the southern Andes mountains. *Atmospheric Research*, *156*, 91 - 101. doi: 10.1016/j.atmosres.2014.12.020

Dessens, J. (1986). Hail in southwestern France i: Hailfall characteristics and hailstrom environment. *Journal of Climate and Applied Meteorology*, *25*(1), 35-47. doi: 10.1175/1520-0450(1986)025<0035:HISFIH>2.0.CO;2

Dessens, J. (1995). Severe convective weather in the context of a nighttime global warming. *Geophysical Research Letters*, *22*(10), 1241–1244. doi: 10.1029/95GL00952

Dessens, J., Berthet, C., & Sanchez, J. (2007). A point hailfall classification based on hailpad measurements: The ANELFA scale. *Atmospheric Research*, *83*(2-4), 132 - 139. doi: 10.1016/j.atmosres.2006.02.029

Dessens, J., Berthet, C., & Sanchez, J. (2015). Change in hailstone size distributions with an increase in the melting level height. *Atmospheric Research*, *158–159*, 245 - 253. doi: 10.1016/j.atmosres.2014.07.004

De Veaux, R., Velleman, P. F., & Bock, D. E. (2011). *Stats: Data and models* (3rd ed.). Addison-Wesley.

Edwards, R., & Thompson, R. L. (1998). Nationwide comparisons of hail size with WSR-88D vertically integrated liquid water and derived thermodynamic sounding data. *Weather and Forecasting*, *13*(2), 277-285. doi: 10.1175/1520-0434(1998)013<0277:NCOHSW>2.0.CO;2

Euskadi. (2013). *LiDAR based 25m digital elevation model of the Basque region.* Retrieved from ftp://ftp.geo.euskadi.net/lidar

Fawcett, T. (2003). ROC graphs: Note and practical considerations for data mining researchers [Computer software manual]. doi: http://www.hpl.hp.com/techreports/2003/HPL-2003-4.pdf

Fielding, A. H. (2007). *Cluster and classification techniques for the biosciences.*

Fitzmaurice, G. N., Laird, N. M., & Ware, J. H. (2004). *Applied longitudinal anaylsis.* Wiley-IEEE.

Fraile, R., Castro, A., & Sánchez, J. (1992). Analysis of hailstone size distributions from a hailpad network. *Atmospheric Research*, *28*(3), 311 - 326. doi: 10.1016/0169-8095(92)90015-3

Frisby, E. M., & Sansom, H. W. (1967). Hail incidence in the tropics. *Journal of Applied Meteorology*, *6*(2), 339-354. doi: 10.1175/1520-0450(1967)006<0339:HIITT>2.0.CO;2

Fujita, T. (1971). *Proposed characterization of tornadoes and hurricanes by area and intensity.* University of Chicago.

Ganuza, A., & Almendros, G. (2003). Organic carbon storage in soils of the Basque country (Spain): The effect of climate, vegetation type and edaphic variables. *Biol. Fertil. Soils*, *37*, 154-162. doi: 10.1007/s00374-003-0579-4

García-Ortega, E., Fita, L., Romero, R., López, L., Ramis, C., & Sánchez, J. (2007). Numerical simulation and sensitivity study of a severe hailstorm in northeast Spain. *Atmospheric Research*, *83*(2-4), 225 - 241. (European Conference on Severe Storms 2004ECSS 2004European Conference on Severe Storms 2004) doi: 10.1016/j.atmosres.2005.08.004

García-Ortega, E., Hermida, L., Hierro, R., Merino, A., Gascón, E., Fernández-González, S., … López, L. (2014). Anomalies, trends and variability in atmospheric fields related to hailstorms in north-eastern Spain. *International Journal of Climatology*, *34*(11), 3251–3263. doi: 10.1002/joc.3910

García-Ortega, E., López, L., & Sánchez, J. L. (2011). Atmospheric patterns associated with hailstorm days in the Ebro Valley, Spain. *Atmospheric Research*, *100*(4), 401 - 427. (5th European Conference on Severe Storms) doi: 10.1016/j.atmosres.2010.08.023

Geer, I. (1997). Glossary of weather and climate: With related oceanic and hydrologic terms. *Choice Reviews Online*, *34*(09), 34-4822. doi: 10.5860/choice.34-4822

Giaiotti, D., Nordio, S., & Stel, F. (2003). The climatology of hail in the plain of Friuli Venezia Giulia. *Atmospheric Research*, *67*, 247 - 259. (European Conference on Severe Storms 2002) doi: 10.1016/S0169-8095(03)00084-X

Glickman, T. S. (2000). *Glossary of meteorology.* American Meteorological Society, Boston.

Gravenhorst, G., & Corrin, M. (1969). Some further studies of 'doped' silver iodide as an ice nucleant. *Proceedings of the international conference on Condensation and ice nuclei, Prague and Vienna.*

Greene, D. R., & Clark, R. A. (1972). Vertically integrated liquid water - a new analysis tool. *Monthly Weather Review*, *100*(7), 548-552. doi: 10.1175/1520-0493(1972)100<0548:VILWNA>2.3.CO;2

Grenier, J.-C., & Zair, P. A. S. (1983). Hailstone growth trajectories in the dynamic evolution of a moderate hailstorm. *Journal of Climate and Applied Meteorology*, *22*(6), 1008-1021. doi: 10.1175/1520-0450(1983)022<1008:HGTITD>2.0.CO;2

Hamid, K., & Buelens, J. (2009). De uitzonderlijke onweerssituatie van 25-26 mei 2009. *Meteorologica*, *3*, 4-10. Retrieved from http://www.frankdeboosere.be/nieuws/news2009/extreme/20hagel/2025-26/20mei/202009/20HAMID/20en/20BUELENS.pdf

Hardaker, P. J., & Auer, A. H. (2007). The separation of rain and hail using single polarisation radar echoes and IR cloud-top temperatures. *Meteorological Applications*, *1*(3), 201–204.

doi: 10.1002/met.5060010301

Hastie, T., & Tibshirani, R. (1986, aug). Generalized additive models. *Statistical Science*, *1*(3), 297–310. doi: 10.1214/ss/1177013604

Hastie, T., Tibshirani, R., & Friedman, J. (2009). *The elements of statistical learning*. Springer.

Hastie, T. J. (1992). Generalized Additive Models. In J. Chambers & T. Hastie (Eds.), *Statistical models in S*. Wadsworth and Brooks/Cole.

Heimann, D., & Kurz, M. (1985). The Munich hailstorm of july 12, 1984: A discussion of the synoptic situation. *Beitr.Phys.Atmos.*, *58*, 528-544. Retrieved from `http://elib.dlr.de/64721/1/85-heimann.pdf`

Heymsfield, A. J., Jameson, A. R., & Frank, H. W. (1980). Hail growth mechanisms in a Colorado storm: Part II: Hail formation processes. *Journal of the Atmospheric Sciences*, *37*(8), 1779-1807. doi: 10.1175/1520-0469(1980)037<1779:HGMIAC>2.0.CO;2

Hijmans, R. J. (2016). raster: Geographic data analysis and modeling [Computer software manual]. (R package version 2.5-8) Retrieved from `https://CRAN.R-project.org/package=raster`

Hohl, R., Schiesser, H.-H., & Aller, D. (2002). Hailfall: the relationship between radar-derived hail kinetic energy and hail damage to buildings. *Atmospheric Research*, *63*(3–4), 177 - 207. doi: 10.1016/S0169-8095(02)00059-5

Holleman, I. (2001). *Hail detection using single-polarization radar* (Tech. Rep.). KNMI. Retrieved from `http://citeseerx.ist.psu.edu/viewdoc/download;jsessionid=0F97FB336768C4106CC116916A0A8265?doi=10.1.1.623.1934&rep=rep1&type=pdf`

Holleman, I., Wessels, H., Onvlee, J., & Barlag, S. (2000). First european conference on radar meteorology development of a hail-detection-product. *Physics and Chemistry of the Earth, Part B: Hydrology, Oceans and Atmosphere*, *25*(10), 1293 - 1297. doi: 10.1016/S1464-1909(00)00197-0

Horvath, A., Seres, A. T., & Nemeth, P. (2015). Radar-based investigation of long-lived thunderstorms in the Carpathian basin. *Idojaras*, *119*(1), 39-51. Retrieved from `https://www.scopus.com/inward/record.uri?eid=2-s2.0-84925439639&partnerID=40&md5=df46e43d2b296948c9fd9bb4a8de9bc0`

Höller, H., Hagen, M., Meischner, P. F., Bringi, V. N., & Hubbert, J. (1994). Life cycle and precipitation formation in a hybrid-type hailstorm revealed by polarimetric and Doppler radar measurements. *J. Atmos. Sci.*, *51*(17), 2500–2522. doi: 10.1175/1520-0469(1994)051<2500:lcapfi>2.0.co;2

Höller, H., & Reinhardt, M. E. (1986). The Munich hailstorm of july 12, 1984 - convective development and preliminary hailstone analysis. *Beitr.Phys.Atmos.*, *59*, 1-12.

IPCC. (2007). Summary for policymakers [Book Section]. In S. Solomon et al. (Eds.), *Climate Change 2007: The Physical Science Basis. Contribution of Working Group I to the Fifth Assessment Report of the Intergovernmental Panel on Climate Change* (p. 1–30). Cambridge, United Kingdom and New York, NY, USA: Cambridge University Press. doi: 10.1260/095830507781076194

IPCC. (2013). Summary for policymakers [Book Section]. In T. Stocker et al. (Eds.), *Climate Change 2013: The Physical Science Basis. Contribution of Working Group I to the Fifth Assessment Report of the Intergovernmental Panel on Climate Change* (p. 1–30). Cambridge, United Kingdom and New York, NY, USA: Cambridge University Press. doi: 10.1017/CBO9781107415324.004

Iturritxa, E., Mesanza, N., & Brenning, A. (2014). Spatial analysis of the risk of major forest diseases in Monterey pine plantations. *Plant Pathology*, *64*(4), 880–889. doi: 10.1111/ppa.12328

James, G., Witten, D., Hastie, T., & Tibshirani, R. (2013). *An introduction to statistical learning*. Springer.

Kapsch, M.-L., Kunz, M., Vitolo, R., & Economou, T. (2012). Long-term trends of hail-related weather types in an ensemble of regional climate models using a Bayesian approach. *Journal of Geophysical Research: Atmospheres*, *117*(D15), n/a–n/a. (D15107) doi: 10.1029/2011JD017185

Kaspar, M., & Mueller, M. (2009). Severe storm in Bavaria, the Czech Republic and Poland on 12-13 july 1984: A statistic- and model-based analysis. *Atmospheric Research*, *93*(1-3), 99 - 110. doi: 10.1016/j.atmosres.2008.10.004

Keraunos. (2009). *Les violents orages du 25 mai 2009 [in french]*. Retrieved from `http://www.keraunos.org/actualites/faits-marquants/2009/les-violents-orages-du-25-mai-2009.html`

Kessinger, C., Brandes, A., & Smith, J. W. (1995). A comparison of the NEXRAD and NSSL hail detection algorithms. *27th conference on Radar Meteorology, AMS*, 603-605. Retrieved from `http://www.rap.ucar.edu/staff/kessinge/cjk_faa1995.html`

Kitzmiller, D. H., McGovern, W. E., & Saffle, R. F. (1995). The WSR-88D severe weather potential algorithm. *Weather and Forecasting*, *10*(1), 141-159. doi: 10.1175/1520-0434(1995)010<0141:TWSWPA>2.0.CO;2

Knight, A., & Knight, N. (2001). Severe convectice storms. In C. A. Doswell III (Ed.), (p. 223 - 248). American Meteorological Society.

Kolkowska, K., & Lorenc, H. (2012). Klęski zywiołowe a bezpieczeństwo wewnętrzne kraju. *Instytut Meteorologii I Gospodarki Wodnej Państwowy Instytut Badawczy, Warszawa, pp. 80–97 Ch. Ryzyko wys-tępowania gradu w Polsce. [in Polish]*. Retrieved from `http://klimat.imgw.pl/wp-content/uploads/2013/01/tom3.pdf`

Kunz, M., Punge, H., Fluck, E., Schmidberger, M., Blahak, U., Handwerker, J., & Mohr, S. (2015). Characteristics and impacts of the severe hailstorm on 28 July 2013. In *Egu* *general assembly conference abstracts* (Vol. 17, p. 1626). Retrieved from `http://meetingorganizer.copernicus.org/EGU2015/EGU2015-1626.pdf`

Kunz, M., & Puskeiler, M. (2010, oct). High-resolution assessment of the hail hazard over complex terrain from radar and insurance data. *Meteorologische Zeitschrift*, *19*(5), 427–439. doi: 10.1127/0941-2948/2010/0452

Kunz, M., Sander, J., & Kottmeier, C. (2009). Recent trends of thunderstorm and hailstorm frequency and their relation to atmospheric characteristics in southwest Germany. *International Journal of Climatology*, *29*(15), 2283–2297. doi: 10.1002/joc.1865

Lachiver, M. (2000). *La gréle du 13 juillet 1788 [in french].* Retrieved from `http://asso.villejust.free.fr/revolution/tornade-1788.html`

Laing, A. G., & Fritsch, J. M. (2000). The large-scale environments of the global populations of mesoscale convective complexes. *Monthly Weather Review*, *128*(8), 2756-2776. doi: 10.1175/1520-0493(2000)128<2756:TLSEOT>2.0.CO;2

Laird, N. M., & Ware, J. H. (1982). Random-effects models for longitudlong data. *Biometrics*, *38*(4), 963-974.

Lenning, E., Fuelberg, H. E., & Watson, A. I. (1998). An evaluation of WSR-88D severe hail algorithms along the northeastern Gulf coast. *Weather and Forecasting*, *13*(4), 1029-1045. doi: 10.1175/1520-0434(1998)013<1029:AEOWSH>2.0.CO;2

Ludlam, F. H., & Macklin, W. C. (1959). Some aspect of a severe storm in southeast England. *Nubila*, *2*, 38-50. Retrieved from `www.scopus.com`

Mallafré, M. C., Ribas, T. R., del Carmen Llasat Botija, M., & Sánchez, J. (2009). Improving hail identification in the Ebro Valley region using radar observations: Probability equations and warning thresholds. *Atmospheric Research*, *93*(1-3), 474 - 482. (4th European Conference on Severe Storms4ECSS4th European Conference on Severe Storms) doi: 10.1016/j.atmosres.2008.09.039

Manzato, A. (2007). The 6h climatology of thunderstorms and rainfalls in the Friuli Venezia Giulia Plain. *Atmospheric Research*, *83*(2-4), 336-348. doi: 10.1016/j.atmosres.2005.08.013

Markowski, P., & Richardson, Y. (2010). *Mesoscale meteorology in midlatitudes.* Wiley Blackwell.

Marks, G., & Minko, G. (1974). The relationship between drought, Diplodia Pinea and dieback of Pinus Radiata. *Austral. Plant Pathol.*, *3*(1), 3. doi: 10.1071/app9740003c

Mason, B. (1971). *The physics of clouds.* Clarendon Press, Oxford UK.

Matheron, G. (1963). Principles of geostatistics. *Economic Geology*, *58*, 1246-1266.

Mezher, R. N., Doyle, M., & Barros, V. (2012). Climatology of hail in Argentina. *Atmospheric Research*, *114–115*, 70 - 82. doi: 10.1016/j.atmosres.2012.05.020

Michaelides, S. C., Savvidou, K., Nicolaides, K. A., Orphanou, A., Photiou, G., & Kannaouros, C. (2008). Synoptic, thermodynamic and agroeconomic aspects of severe hail events in Cyprus. *Natural Hazards and Earth System Sciences*, *8*(3), 461-471. doi: 10.5194/nhess-8-461-2008

Minko, G. (1979). Long term effects of hail damage on radiata pine. *Australian Forestry*, *42*(3), 168–171. doi: 10.1080/00049158.1979.10674222

Mohr, S., Kunz, M., & Keuler, K. (2015). Development and application of a logistic model to estimate the past and future hail potential in Germany. *Journal of Geophysical Research: Atmospheres*, *120*(9), 3939–3956. (2014JD022959) doi: 10.1002/2014JD022959

Moisselin, J. M., & Guillande, R. (2004). Development of intensity scales for a wide set of natural phenomena. *European Meteorological Society, Annual Meeting Abstracts, Nice*, *1*, 00134.

Morgan, G. M. (1973). A general description of the hail problem in the Po Valley of northern Italy. *Journal of Applied Meteorology*, *12*(2), 338-353. doi: 10.1175/1520-0450(1973)012<0338:AGDOTH>2.0.CO;2

National Climatic Data Center. (2016). Global summary of [the] day (GSOD) database: Product description [online accessed: 23/06/2016] [Computer software manual]. Retrieved from `ftp://ftp.ncdc.noaa.gov/pub/data/gsod/readme.txt`

Nelder, J. A., & Wedderburn, R. W. (1972). Generalized linear models. *Journal of the Royal Statistical Society*, *135*, 370-384.

Ninyerola, M., Pons, X., & Roure, J. (2005). *Atlas climático digital de lapenínsula ibérica. metodología y aplicaciones en bioclimatología y geobotánica.* Universidad Autónoma de Barcelona, Bellaterra.

Ninyerola, M., Pons, X., & Roure, J. M. (2000). A methodological approach of climatological modelling of air temperature and precipitation through GIS techniques. *International Journal of Climatology*, *20*(14), 1823–1841. doi: 10.1002/1097-0088(20001130)20:14<1823::AID-JOC566>3.0.CO;2-B

Nisi, L., Martius, O., Hering, A., Kunz, M., & Germann, U. (2016). Spatial and temporal distribution of hailstorms in the Alpine region: a long-term, high resolution, radar-based analysis. *Quarterly Journal of the Royal Meteorological Society*, *142*(697), 1590–1604. doi: 10.1002/qj.2771

Nyland, R. D. (2002). *Silviculture: Concepts and applications* (2nd ed.). Illinois: Waveland Press.

O'Sullivan, D., & Urwin, D. J. (2010). *Geographic information analysis* (2nd ed.). John Wiley & Sons, Ltd.

Pebesma, E. (2004). Multivariable geostatistics in S: the gstat package. *Computers & Geosciences*, *30*, 683-691.

Pebesma, E., & Bivand, R. (2005). Classes and methods for spatial data in R. *R News*, *5*(2). Retrieved from `http://cran.r-project.org/doc/Rnews/`

Perpiñán, O., & Hijmans, R. (2016). rasterVis [Computer software manual]. (R package version 0.40) Retrieved from `http://oscarperpinan.github.io/rastervis/`

Petrocchi, P. J. (1982). Automatic detection of hail by radar. *AFGL, Tech. Report 82-0277*.

Piani, F., Crisci, A., Chiara, G. D., Maracchi, G., & Meneguzzo, F. (2005, feb). Recent trends and climatic perspectives of hailstorms frequency and intensity in Tuscany and Central Italy. *Nat. Hazards Earth Syst. Sci.*, *5*(2), 217–224. doi: 10.5194/nhess-5-217-2005

Pinheiro, J., Bates, D., DebRoy, S., Sarkar, D., & R Core Team. (2016). nlme: Linear and nonlinear mixed effects models [Computer software manual]. (R package version 3.1-128) Retrieved from `http://CRAN.R-project.org/package=nlme`

Porras, I., Sairouni, A., & Aran, M. (2013). *Climatologia de la probalititat de calamarsa a Catalunya.* ([in Catalan]) Retrieved from `http://static-m.meteo.cat/wordpressweb/wp-content/uploads/2014/11/18130754/nota-estudi-climatologia-calamarsa-n74.pdf`

Pruppacher, H., & Klett, J. (2010). *Microphysics of clouds and precipitation*. Springer Netherlands. doi: 10.1007/978-0-306-48100-0

Punge, H., Bedka, K. M., Kunz, M., & Werner, A. (2014). A new physically based stochastic event catalog for hail in Europe. *Nat Hazards*, *73*(3), 1625–1645. doi: 10.1007/s11069-014-1161-0

Punge, H., & Kunz, M. (2016). Hail observations and hailstorm characteristics in Europe: A review. *Atmospheric Research*, *176–177*, 159 - 184. doi: 10.1016/j.atmosres.2016.02.012

Punkka, A.-J., & Bister, M. (2005). Occurrence of summertime convective precipitation and mesoscale convective systems in Finland during 2000-01. *Monthly Weather Review*, *133*(2), 362-373. doi: 10.1175/MWR-2854.1

Puskeiler, M. (2013). *Radarbasierte Analyse der Hagelgefährdung in Deutschland* (Doctoral dissertation, Institut für Meteorologie und Klimaforschung, Karlsruher Institut für Technologie (KIT)).

R Core Team. (2016). R: A language and environment for statistical computing [Computer software manual]. Vienna, Austria. Retrieved from `https://www.R-project.org/`

Rikken, M. G., & van Rijn, R. P. (1993). *Soil pollution with heavy metals - an inquiry into spatial variation, cost of mapping and the risk evaluation of copper, cadmium, lead and zinc in the floodplains of the Meuse west of Stein, the Netherlands.* Doctoraalveldwerkverslag, Dept. of Physical Geography, Utrecht University.

Rinker, T. W., & Kurkiewicz, D. (2015). pacman: Package management for R [Computer software manual]. Buffalo, New York. (version 0.4.1) Retrieved from `http://github.com/trinker/pacman`

RStudio Team. (2015). Rstudio: Integrated development environment for R [Computer software manual]. Boston, MA. Retrieved from `http://www.rstudio.com/`

Russ, G., & Brenning, A. (2010). Data mining in precision agriculture: Management of spatial information. In E. Hüllermeier, R. Kruse, & F. Hoffmann (Eds.), *Computational Intelligence for Knowledge-Based Systems Design: 13th International Conference on Information Processingand Management of Uncertainty, IPMU 2010, Dortmund, Germany, June 28 - July 2, 2010. Proceedings* (pp. 350–359). Berlin, Heidelberg: Springer Berlin Heidelberg. doi: 10.1007/978-3-642-14049-5$_3$6

Saa Requejo, A., Garcia Moreno, R., Diaz Alvarez, M. C., Burgaz, F., & Tarquis, M. (2011). Analysis of hail damages and temperature series for peninsular Spain. *Natural Hazards and Earth System Sciences*, *11*(12), 3415–3422. doi: 10.5194/nhess-11-3415-2011

Schiesser, H. H. (2003). Hail. In *Extreme events and climate change. organe consultatif sur les changements climatiques (OcCC)* (p. 65-69). Retrieved from `http://proclimweb.scnat.ch/portal/ressources/868.pdf`

Schleusener, R., & Jennings, P. (1960). An energy method for relative estimate of hail intensity. *Bulletin of the American Meteorlogical Society*, *41*(7), 372-376. Retrieved from `https://dspace.library.colostate.edu/bitstream/handle/10217/37628/0001_Bluebook.pdf?sequence=1`

Seres, A. T., & Horváth, A. (2015). Thunderstorm climatology in Hungary using Doppler radar data. *Idojaras*, *119*(2), 185-196.

Simeonov, P., & Georgiev, C. G. (2003). Severe wind/hail storms over Bulgaria in 1999-2001 period: Synoptic- and mesoscale factors for generation. *Atmospheric Research*, *67-68*, 629 - 643. (European Conference on Severe Storms 2002) doi: 10.1016/S0169-8095(03)00077-2

Sioutas, M. (2011). Hail occurrence in Greece. *6th European Conference on Severe Storms (ECCS 2011)*. Retrieved from `http://www.essl.org/ECSS/2011/programme/abstracts/224.pdf`

Smith, H., Wingfield, M., & Coutinho, T. (2002). The role of latent Sphaeropsis Sapinea infections in post-hail associated die-back of Pinus Patula. *Forest Ecology and Management*, *164*(1-3), 177–184. doi: 10.1016/s0378-1127(01)00610-7

Smith, R. B. (1979). The influence of mountains on the atmosphere. In B. Saltzman (Ed.), *Advances in Geophysics* (Vol. 21, p. 87 - 230). Elsevier. doi: 10.1016/S0065-2687(08)60262-9

Smyth, T. J., Blackman, T. M., & Illingworth, A. J. (1999). Observations of oblate hail using dual polarization radar and implications for hail-detection schemes. *Q.J Royal Met. Soc.*, *125*(555), 993–1016. doi: 10.1002/qj.49712555512

Snijders, T., & Bosker, R. (1991). *An introduction to basic and advanced multilevel modelling.* SAGE Publications Ltd, Thousand Oaks, CA.

Stumpf, G. J., Smith, T., & Hocker, J. (2004). New hail diagnostic parameters derived by integrating multiple radar and multiple sensors. *Preprints, 22nd Conf. on Severe Local Storms, Hyannis, MA, Amer. Meteor. Soc., p. 7.8. CD preprints.* Retrieved from http://cimms.ou.edu/~smith/pubs/sls2004_hail.pdf

Suwala, K., & Bednorz, E. (2013). Climatology of hail in central Europe. *Quaestiones Geographicae*, *32*(3), 99-110. doi: 10.2478/quageo-2013-0025

Swart, W. J., Wingfield, M. J., & Knox-Davies, P. (1987). Factors associated with Sphaeropsis Sapinea infection of pine trees in South Africa. *Phytophylactica*, *19*, 505-510.

Sánchez, J., Gil-Robles, B., Dessens, J., Martin, E., Lopez, L., Marcos, J., … García-Ortega, E. (2009). Characterization of hailstone size spectra in hailpad networks in France, Spain, and Argentina. *Atmospheric Research*, *93*(1), 641 - 654. (4th European Conference on Severe Storms4ECSS4th European Conference on Severe Storms) doi: 10.1016/j.atmosres.2008.09.033

Sánchez, J., López, L., García-Ortega, E., & Gil, B. (2013). Nowcasting of kinetic energy of hail precipitation using radar. *Atmospheric Research*, *123*, 48 - 60. (6th European Conference on Severe Storms 2011. Palma de Mallorca, Spain) doi: 10.1016/j.atmosres.2012.07.021

Tessier, H. A., Buache, J. N., & Leroy, J. B. (1790). *Rapport ou second mémoire sur l´orage a grgré du dimanche 13 juillet 1788. acad. roy. sci. paris 263-308 [in french].* Retrieved from https://www.archive.org/stream/mmoiresdelacad10acad/mmoiresdelacad10acad_djvu.txt

Tobler, W. (1970). A computer movie simulating urban growth in the Detroit region. *Economic Geography*, *46*(2), 234-240.

Tuovinen, J.-P., Punkka, A.-J., Rauhala, J., Hohti, H., & Schultz, D. M. (2009). Climatology of severe hail in Finland: 1930-2006. *Monthly Weather Review*, *137*(7), 2238-2249. doi: 10.1175/2008MWR2707.1

UK Met. Office. (2015). Days of hail - annual average 1971-2000 [online; accessed 03-06-2016] [Computer software manual]. Retrieved from http://www.metoffice.gov.uk/public/weather/climate/

van Delden, A. (1998). The synoptic setting of a thundery low and associated prefrontal squall line in western Europe. *Meteorology and Atmospheric Physics*, *65*(1), 113–131. doi: 10.1007/BF01030272

Venables, W. N., & Ripley, B. D. (2002). *Modern applied statistics with S* (Fourth ed.). New York: Springer. (ISBN 0-387-95457-0) Retrieved from http://www.stats.ox.ac.uk/pub/MASS4

Vinet, F. (2001). Climatology of hail in France. *Atmospheric Research*, *56*(1–4), 309 - 323. (Conference on European Tornadoes and Severe Storms) doi: 10.1016/S0169-8095(00)00082-X

Waldvogel, A., Federer, B., & Grimm, P. (1979). Criteria for the detection of hail cells. *Journal of Applied Meteorology*, *18*(12), 1521-1525. doi: 10.1175/1520-0450(1979)018<1521:CFTDOH>2.0.CO;2

Waldvogel, A., Federer, B., Schmid, W., & Mezeix, J. F. (1978). The kinetic energy of hailfall. part 2: Radar and hailpads. *J. Appl. Meteor.*, *17*, 1680-1693.

Waldvogel, A., Schmid, W., & Federer, B. (1978). The kinetic energy of hailfall. part 1: Hailstone spectra. *J. Appl. Meteor.*, *17*, 515-520.

Webb, J., Elsom, D., & Meaden, G. (2009). Severe hailstorms in Britain and Ireland, a climatological survey and hazard assessment. *Atmospheric Research*, *93*(1–3), 587 - 606. (4th European Conference on Severe Storms) doi: 10.1016/j.atmosres.2008.10.034

Webb, J., Elsom, D. M., & Meaden, G. T. (1986). The TORRO hailstorm intensity scale. *Journal of Meteorology, UK*, *11*(114), 337-339. Retrieved from http://www.ijmet.org/wp-content/uploads/2016/04/114.pdf

Webb, J. D. C., & Elsom, D. M. (1994). The great hailstorm of august 1843: The severest recorded in Britain? *Weather*, *49*(8), 266–273. doi: 10.1002/j.1477-8696.1994.tb06034.x

Wickham, H. (2009). *ggplot2: Elegant graphics for data analysis.* Springer-Verlag New York. Retrieved from http://ggplot2.org

Wickham, H. (2011). The split-apply-combine strategy for data analysis. *Journal of Statistical Software*, *40*(1), 1–29. Retrieved from http://www.jstatsoft.org/v40/i01/

Wickham, H. (2015). stringr: Simple, consistent wrappers for common string operations [Computer software manual]. (R package version 1.0.0) Retrieved from https://CRAN.R-project.org/package=stringr

Wickham, H., & Francois, R. (2016). dplyr: A grammar of data manipulation [Computer software manual]. (R package version 0.5.0) Retrieved from https://CRAN.R-project.org/package=dplyr

Wickham, H., Francois, R., & Müller, K. (2016). tibble: Simple data frames [Computer software manual]. (R package version 1.1) Retrieved from https://CRAN.R-project.org/package=tibble

Wilke, C. O. (2016). cowplot: Streamlined plot theme and plot annotations for 'ggplot2' [Computer software manual]. (R package version 0.6.2) Retrieved from https://CRAN.R-project.org/package=cowplot

Witt, A., Eilts, M. D., Stumpf, G. J., Johnson, J. T., Mitchell, E. D. W., & Thomas, K. W. (1998). An enhanced hail detection algorithm for the WSR-88D. *Weather and Forecasting*, *13*(2), 286-303. doi: 10.1175/1520-0434(1998)013<0286:AEHDAF>2.0.CO;2

Wood, S. (2003). Thin plate regression splines. *Journal of the Royal Statistical Society*, *65*(1), 95-114.

Wood, S. (2006). *Generalized additive models: An introduction with R.* Chapman and Hall/CRC.

World Meteorological Organization. (2008). *Technical regulations* (Tech. Rep. No. WMO-No. 49 vol. ii,). Meteorological Service for International Air Navigation. Retrieved from http://www.wmo.int/pages/prog/hwrp/publications/technical_regulations/WMO_N49_TechnReg_Vol2.pdf

World Meteorological Organization. (2016). *National Climatic Data Center (NCDC): Global summary of day (GSOD) database [online accessed: 15/06/2016]*. Retrieved from http://www7.ncdc.noaa.gov/CDO/cdoselect.cmd?datasetabbv=GSOD&countryabbv=&georegionabbv=

Wright, J. P., & Marks, G. C. (1970). Loss of merchantable wood in radiata pine associated with infection by Diplodia pinea. *Australian Forestry*, *34*(2), 107–119. doi: 10.1080/00049158.1970.10675516

Xie, B., Zhang, Q., & Wang, Y. (2008). Trends in hail in China during 1960–2005. *Geophysical Research Letters*, *35*(13), n/a–n/a. (L13801) doi: 10.1029/2008GL034067

Xie, Y. (2016). knitr: A general-purpose package for dynamic report generation in R. R package version 1.13. [Computer software manual].

Zuur, A. F., Ieno, E. N., & Smith, G. M. (2007). *Analysing ecological data*. Springer.

Zuur, A. F., Ieno, E. N., Walker, N. J., Saveliev, A. A., & Smith, G. M. (2008). *Mixed effects models and extensions in ecology with R*. Springer.

Zwolinski, J. B., Swart, W., & Wingfield, M. (1995). Association of Sphaeropsis sapinea with insect infestation following hail damage of Pinus radiata. *Forest Ecology and Management*, *72*(2-3), 293–298. doi: 10.1016/0378-1127(94)03459-a

Zwolinski, J. B., Swart, W. J., & Wingfield, M. J. (1990). Economic impact of a post-hail outbreak of dieback induced by Sphaeropsis sapinea. *Forest Pathol*, *20*(6-7), 405–411. doi: 10.1111/j.1439-0329.1990.tb01155.x

APPENDIX A

CONDITIONAL DENSITY PLOTS OF HAIL OCCURENCE OF BILBAO AND SAN SEBASTIAN

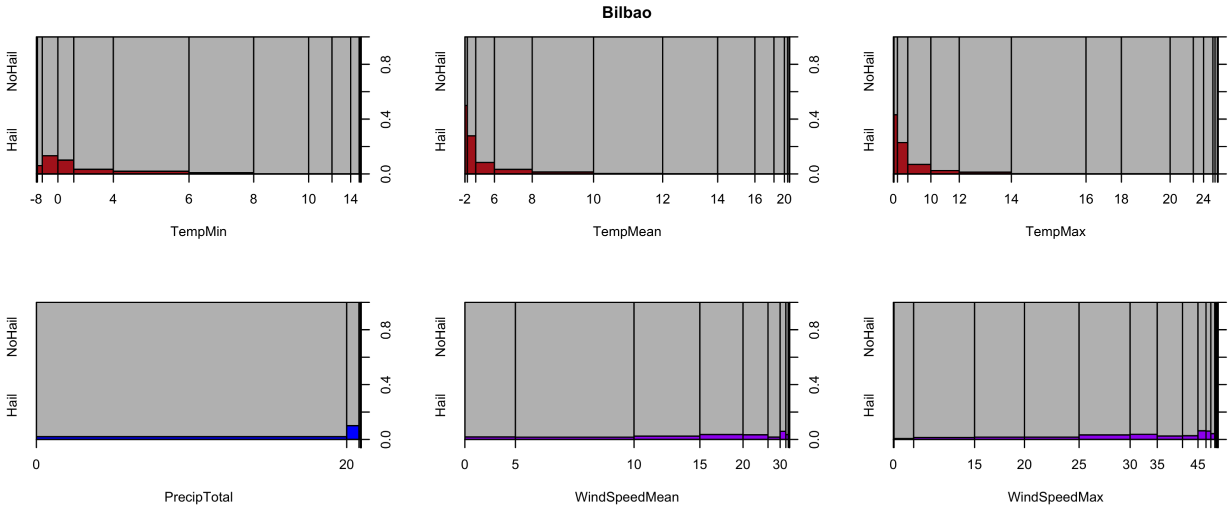

Figure A.1.: Conditional density plots (spinograms here) of hail occurence in relation to various climatic variables for the time period of 1973 - 2015 (November - April) of Bilbao. Y-axis shows the probability of hail occurence for a given group of x. X-axis grouping according to histogram distribution of x.

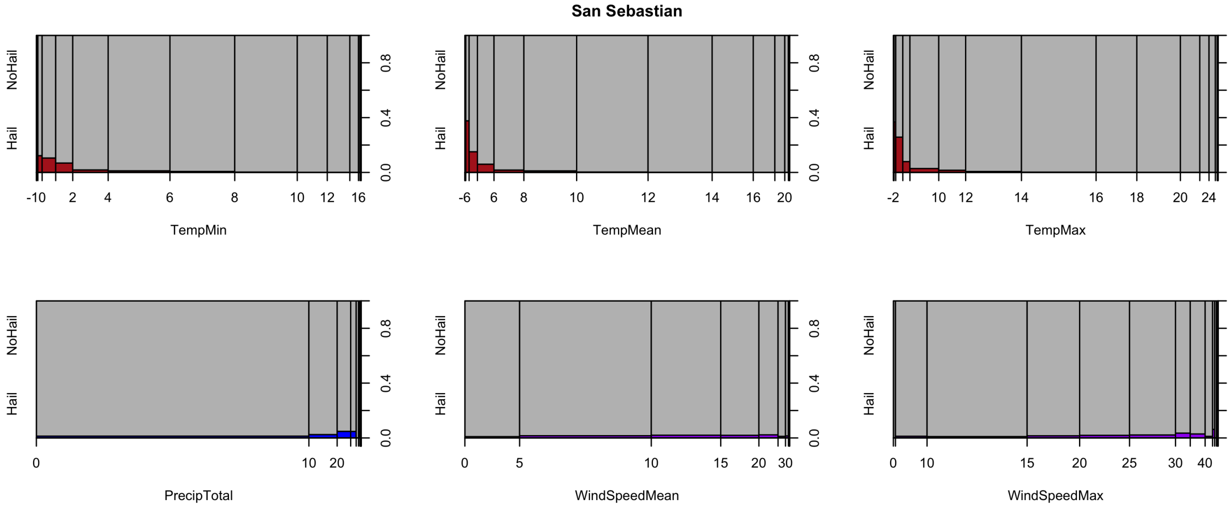

Figure A.2.: Conditional density plots (spinograms here) of hail occurence in relation to various climatic variables for the time period of 1973 - 2015 (November - April) of San Sebastian. Y-axis shows the probability of hail occurence for a given group of x. X-axis grouping according to histogram distribution of x.

APPENDIX B

USAGE OF WEATHER-RADAR INFORMATION IN HAIL APPLICATIONS

As direct measurements of hail using hailpads or other sources are highly expensive and limited to small areas (subsection 2.1.1), weather radar information is frequently used nowadays in studies dealing with hail (Battan, 1973). Since the 1970s, radars are commonly used and different algorithms have been developed to detect storm cells bearing hail. One of the first and most popular approaches goes back to Waldvogel et al. (1979), who categorised storm cells in three subclasses being "Strong Rain Cell", "Weak Hail Cell" and "Strong Hail Cell", using the heigth difference in km of the clouds 0°C and -45°C temperature levels. However, only about 50% of detected hail cells produced hail which also reached the ground. Other hail detection approaches are described in Auer (1994); Witt et al. (1998); Hardaker and Auer (2007) and will be explained in the following chapter in more detail.

Today, techniques using dual-polarization radar data are often used (if available) to distinguish between rain (non-spherical droplets) and hail (spherical droplets). Dual-polarization radars measure in horizontal (Z_H) and vertical polarization (Z_V). With this information, one can compute the ratio between both reflectivities (Z_{DR}) using the following equation:

$$Z_{DR}(dB) = 10^{10} log(\frac{Z_H}{Z_V}) \tag{B.1}$$

For rain, Z_{DR} never becomes negative (varies between 0 and 4 dB) and is correlated with Z_H while for hail Z_{DR} ranges around 0 dB and is uncorellated to Z_H. With this approach, Aydin, Seliga, and Balaji (1986) studied major hailstorms in Colorado. Other studies which used dual-polarization radar information to derive information of hail properties are Höller, Hagen, Meischner, Bringi, and Hubbert (1994); Smyth, Blackman, and Illingworth (1999). However, as most weather radars only feature one polarization, most hail detection methods focus on using information of single-polarization radars.

B.1. Hail Detection Algorithms Using Single-Polarization Radar

B.1.1. CAPPI Method

The Constant Altitude Plan-Position Indicator (CAPPI) method uses single-polarization radar information "based on a Plan-Position Indicator (PPI) of the radar reflectivity at constant altitude" (Holleman, 2001). The assumption is made that the diameters (D_i) of scattering particles present in atmosphere are smaller than the wavelength of the radar (most often C- or S-band), which equals the physical process called *Rayleigh scattering* (Dardy, 1973). Hence, radar reflectivity Z can be expressed as:

Table B.1.: Radar reflectivity Z in dBZ and the approximate rainfall rate R on the ground (Holleman, 2001)

Z [dBZ]	7	15	23	31	39	47	55
R [mm/h]	0.1	0.3	1	3	10	30	100

$$Z = \sum_i n_i \times D_i^6 \tag{B.2}$$

where n_i refers particle count per unit volume with a diameter D_i. Due to the fact of hailstones having a large diameter compared to rain drops and other atmospheric particles, radar reflectivity increases largely with the presence of hail in the cloud. While rain droplets reach a maximum of 6.5 mm in diameter and the mean being much lower, hailstones can reach values of 10 cm and larger (Holleman, 2001). According to Auer (1994), a reflectivity value of 54 dBZ corresponds to hailstones with a diameter of around 10 mm with the assumption of hailstones being distributed over the entire radar beam (Table B.1). A commonly used threshold for distinguishing between severe rain and hail using the CAPPI approach is 55 dBZ, introduced by Mason (1971).

B.1.2. Maximum Reflectivity (ZMAX) Method

This method, also refered to as "ZMAX", simply takes the maximum reflectivity value at every angle instead of taking the reflectivity value at a constant altitude as done in the CAPPI method. The received value, also refered to as "maxPPI", is then applied on a scale with average precipitation expectations like the one shown for CAPPI (Table B.1). Using this method ensures not to miss certain clouds which are located at higher altitudes as the chosen altitude of the CAPPI method. Contratry, the radar operates on different altitudes, depending on the angles, which may lead to biased results (Holleman, 2001).

B.1.3. VIL Method

Greene and Clark (1972) proposed the use of the Vertically Integrated Liquid (VIL) variable in hail prediction algorithms as well as for hydrological applications. Combining VIL and CAPPI/ZMAX information one is able to retrieve information on the three-dimensional characteristics of a hailstorm cell. First, VIL needs to be calculated by converting reflectivity to liquid water content (M) utilizing a semi-empirical relation betwen Z [mm^6/m^3] and M [g/m^3]:

$$M = 3.44 \times 10^{-3} Z^{4/7} \tag{B.3}$$

After that, the retrieved liquid water value at each location is vertically integrated:

$$VIL = \int_0^{H_{top}} M \times dh = 3.44 \times 10^{-3} \int_0^{H_{top}} Z^{4/7} dh \tag{B.4}$$

where VIL is calculated in kg/m^2 or in mm of "potential rainfall" in combination with the height in kilometer (Holleman, 2001). Next, the three-dimensional information is converted to a vertical plane of liquid water present starting at a specific altitude. According to Kitzmiller, McGovern, and Saffle (1995), VIL is a function of updraft and cloud depth due to the fact of precipitation formation rate being "roughly proportional to updraft velocity".

It was found that a high VIL value shows a good correlation with the appearance of severe (hail)storms. On the existence of stratiform cloud situations, VIL hardly exceeds a value of 10 kg/m^2 whereas in thunderstorms the observed value is much higher. However, no general warning threshold exists for hail detection using VIL information. Refering to Lenning, Fuelberg, and Watson (1998), a common method used in the USA is to take the VIL value of the first hail storm which occured on a specific day.

B.1.4. VIL-Density

Attempting to get rid of the threshold problems regarding the VIL method, Amburn and Wolf (1997) proposed a normalization of the VIL value utilizing echotop heights at a certain reflectivity threshold, for example 7 dBZ. According to the authors, this would pick up the problem that some high-topped storms do not produce hail although they show a high VIL value and some low-topped ones instead produce hail while showing a low VIL value. The "VIL-density" method is defined as follows:

$$VIL - density = \frac{VIL}{H_{top}} \tag{B.5}$$

where VIL-density is calculated in g/m^3 with VIL given in kg/m^2 and H_{top} in km. Amburn and Wolf (1997) finally proposed a VIL-density value of 3.5 g/m^3 as a threshold for occuring hail. However, the advantage if the VIL-density method over the VIL-method was refuted by several studies. One examples is the work of Edwards and Thompson (1998), who received the same results using a VIL threshold of 38 kg/m^2 and the proposed VIL-density threshold with the additional remark that hail is always observed after exceeding a value of 43 kg/m^2, regardless of echotop height.

B.1.5. Method of Auer

Auer (1994) utilized radar reflectivity at low altitude in combination with cloud-top temperatures to detect hail and seperate it from heavy rain. Cloud-top temperatures can be derived by the infrared band of geostationary satellites, e.g. Meteosat. Observing more than 100 hail and rain cases during all seasons of a year in New Zealand, a very good differentiation between hail and heavy rain was achieved by Auer (1994) (Figure B.1). The best threshold for CAPPI reflectivity (Z_{Th}) as a function of cloud-top temperature (T_{top}) was defined in Hardaker and Auer (2007) as follows:

$$Z_{Th} = \begin{cases} -0.38 \times (T_{top} - 85.0) & \text{if } T_{top} \leq -11°C \\ 1.33 \times (T_{top} - 38.8) & \text{if } T_{top} > -11°C \end{cases} \tag{B.6}$$

where the first function presented in the first line ($T_{top} > -11°C$) refers to the dashed line of Figure B.1 and the second line expresses the case of $T_{top} > -11°C$.

Depending on cloud-top temperature (-11°C to -55°C), the optimum threshold ranges between 36 and 53 dBZ for discrimantion of hail and rain. The method was tested over all seasons and showed a much better performance than the standard CAPPI method (Holleman, 2001). In addition, Hardaker and Auer (2007) successfully seperated the parts of hail and rain which contribute to the total reflectivity signal (Figure B.1) by attributing the part of the radar reflectivity to hail which exceeds the warning threshold at a certain cloud-top temperature and the lower part to rain, respectively. Subsequently, it is feasible to determine the maximum possible precipitation rate based on cloud-top temperature.

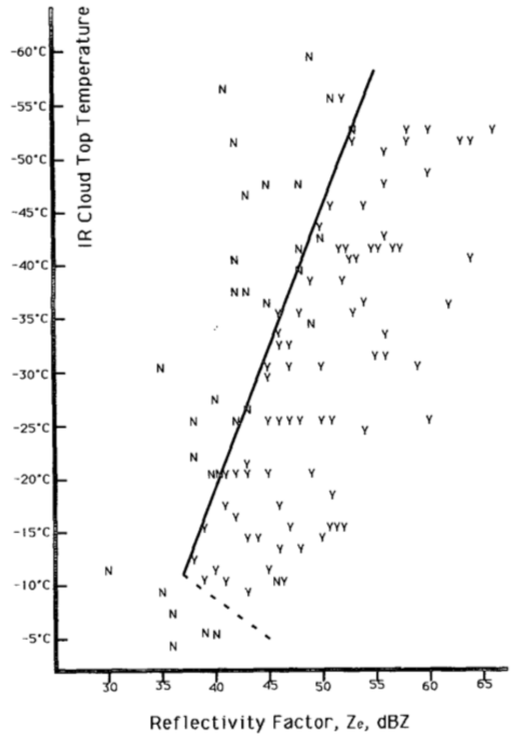

Figure B.1.: The distribution of hail (Y) or rain (no hail) (N) events as a function of low-level CAPPI reflectivity and convective cloud-top temperature, Auer (1994)

B.1.6. NEXRAD

B.1.6.1. Hail Detection Algorithm

Within the Next-Generation Radar (NEXRAD) network of the USA, also known as WSR-88D which stands for "Weather Surveillance Radar, 1988, Doppler", several hail detection algorithms were developed. Kessinger, Brandes, and Smith (1995) compared different algorithms which were developed within the NEXRAD framework. Nowadays, two versions of the NEXRAD exist, the "old" and the "new" NEXRAD hail detection algorithm.

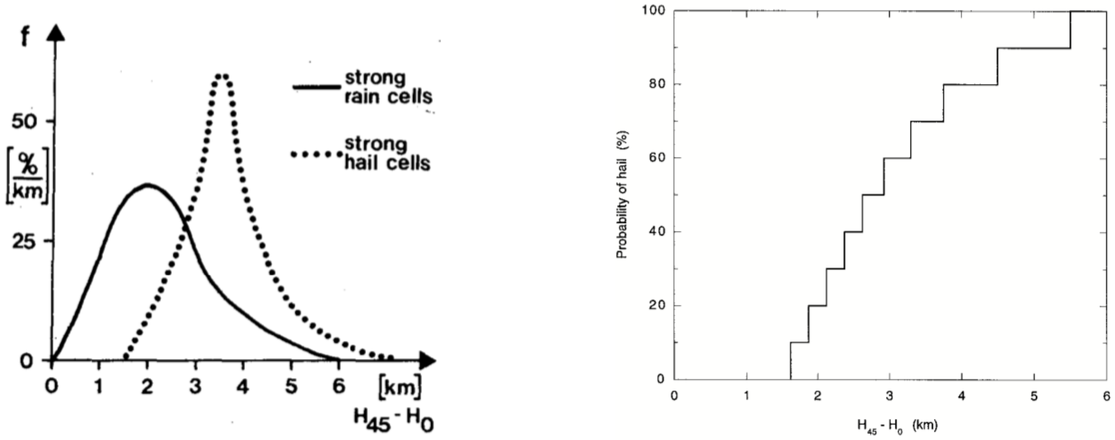

(a) The normalized frequency distributions of the parameter ($H_{45} - H_o$) for the strong rain cells (SRC) and strong hail cells (SHC), Waldvogel et al. (1979)

(b) Probability of hail at the ground as a function of $H_{45} - H_o$. Here H_{45} is the height of the 45-dBZ echo above radar level and H_o is the height of the melting level, Witt et al. (1998)

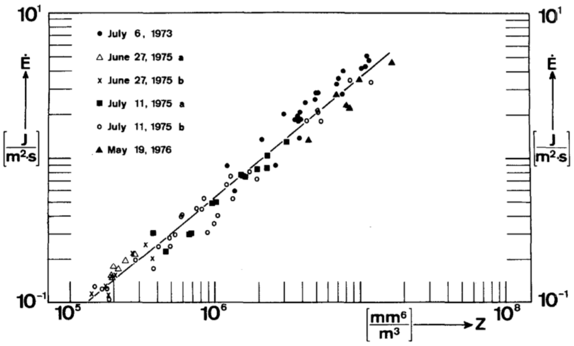

Figure B.3.: The real $Z - E$ relations from four different hailstorms measured at six different measuring sites; 86 correlations points of the hailstone spectra each having an E value > 0.1 J $m^{-2}s^{-1}$ are plotted. The regression line is given as a straight line, Waldvogel, Schmid, and Federer (1978)

The original ("old") version goes back to Petrocchi (1982) and uses several indicators: "Presence of reflictivity core of 50 dBZ or higher somehwere between five and 12 km altitude and the presence of radar echotops higher than 8 km" in combination with "a mid-level overhang of more than 4 km" Holleman (2001). Applying different weights to these hail indicators, four different hail indices were recieved: hail, probable hail, no hail and insufficient data.

However, this algorithm was replaced by the "new" NEXRAD algorithm developed by Witt et al. (1998). The new algorithm is said to be more straightforward while also showing a better performance than the "old" one (Kessinger et al., 1995). It produces a probability output of hail and is based on the work of Waldvogel et al. (1979). The latter study simply concluded to use the height difference between the freezing level (H_{T0}) and the altitude at which a reflictivity value of 45 dBZ (H_{Z45}) is measured. If this height difference exceeds a value of 1.4 kilometer, the presence of hail starts to become likely. Waldvogel et al. (1979) used radiosonde data back then to retrieve the freezing level height. Today though, this variable is determined using numerical weather prediction models (Holleman, 2001). Since Waldvogel et al. (1979) provided only a frequency distribution of the parameter ($H_{45} - H_0$) (Figure B.2a), the NEXRAD algorithm converted this parameter value into a probability of hail, starting with a 10% probability at a height difference of 1.6 km and ending at 6 km (100% likeliness) (Figure B.2b).

B.1.6.2. Hail Severity Algorithm

The NEXRAD algorithm is also capable of estimating the severity of hail Witt et al. (1998). This algorithm is sometimes refered to as the Probability of Severe Hail (POSH) algorithm. A semi-empirical relationship of kinetic energy flux of hail stones (E) and radar reflectivity was found by Waldvogel, Schmid, and Federer (1978); Waldvogel, Federer, Schmid, and Mezeix (1978). Throughout these two studies, four severe hail storms at six different sites were observed and the relationship between E and Z investigated (see Figure B.3). The observed regression line is as follows:

$$E(Z) = 5.0 \times 10^{-6} Z^{0.84} \tag{B.7}$$

On the base of this kinetic energy flux as a function of hail, the Severe Hail Index (SHI) was proposed by "vertically integrating the obtained flux weighted with a reflectivity-based $W(Z)$ and a temperature-based $W_T(H)$ function (Holleman, 2001):

$$SHI = \frac{1}{10} \int_{0}^{H_{top}} W(Z(h)) \times W_T(h) \times E(Z(h)) dh \tag{B.8}$$

where the reflectivity-based weighting function $W(Z)$ is defined as:

$$W(Z) = \begin{cases} 0 & \text{for } Z \leq Z_L \\ \frac{Z-Z_L}{Z_U-Z_L} & \text{for } Z_L < Z < Z_U \\ 1 & \text{for } Z \geq Z_U \end{cases} \tag{B.9}$$

and the temperature-based weighting function $W_T(H)$ as:

$$W_T(H) = \begin{cases} 0 & \text{for } H \leq H_{T0} \\ \frac{H-H_{T0}}{H_{Tm20}-H_{T0}} & \text{for } H_{T0} < H < H_{Tm20} \\ 1 & \text{for } H \geq H_{Tm20} \end{cases} \tag{B.10}$$

with the reflectivity cut-off values Z_L and Z_U set at 40 and 50 dBZ and H_{T0} (H_{Tm20}) being the height of the 0°C (-20°C) temperature level, respectively. With this setting, the SHI is mainly sensitive to high reflectance values at temperatures around -20°C and colder. This is prefered as hail mainly originates at such temperatures. Depending on the freezing level, a warning threshold is determined utilizing an empirical relationship and a probability value of severe hail occurence is calculated. In the "hail algorithm comparison study" of Kessinger et al. (1995) it was found that the SHI is able to detect "large" hail, i.e. hail with a diameter larger than 13 mm, "somewhat better than the normal NEXRAD hail detection algorithm" (Holleman, 2001).

B.2. State-of-the-Art Hail Research in Europe

In the following subsection, a summary of recent studies covering hail(-frequency) questions are presented. Paper selection and regional grouping of this section mostly refers to the work of Punge and Kunz (2016).

Kunz et al. (2009) investigated the convective activity during 1974-2003 in the state of Baden-Würtemmberg in southwest Germany using different datasets, i.e. thunderstorm days at synoptic stations, hail damage data from a building insurance company, large scale circulation and weather pattern, and convective indices derived from radiosonde observations at 12:00 UTC. The research question was to clarify about possible changes of total thunderstorm days, hail damage and reflectivity during the years. Almost no change was observed in the yearly number of thunderstorm days. However, hail damages and hail days significantly increased during those thirty years. The authors attributed these increases to an increase in occurence of specific circulation patterns being associated with hail origination.

In Switzerland, Nisi, Martius, Hering, Kunz, and Germann (2016) utilized 13 years of volumetric (3D) radar data to feed two hail detection algorithms, namely the Probability of Hail (POH) and the Maximum Expected Severe Hail Size (MESHS). A comprehensive hail distribution map was created, highlighting both local-and regional scale hail characteristics. Regarding the spatial distribution of hail days per year, several maximas at the northern and southern foothills, respectively, and over the Jura mountains were found. Minima of hail frequency were found directly over the Alps.

Punge et al. (2014) presented a hail probability map for central Europe using a homogeneous source which consisted of Overshooting Cloud Tops (OT) information derived from the MSG-SEVIRI IRW band in combination with ESWD reports. Up to this point, only local hail risk estimations existed for some european contries featuring a high variety of used algorithms. The study revealed high risk areas in southern and central Europe with peaks over mountainous regions like the Alps or the Pyrenees but also over central Eastern Europe.

Seres and Horváth (2015) observed a period from 2004-2012 in Hungary utilizing the CAPPI method on Doppler radar data provided by the Hungarian Meteorological Service. Using grouping thresholds at 40, 50 and 55 dBZ, 42 severe storm events were found for the highest group for all years. Maximums were found in eastern Hungary with values of up to 2.3 severe storm days (> 55 dBZ) per year and in the SW (2d/y). The average values of all observed areas ranged between 0.3 - 1.5 hail days per year.

Due to the existence of the ANELFA scale, more than 20 years of hailpad data exist for SW france, making it one of the best investigated areas regarding hail. Berthet, Dessens, and Sanchez (2011) used this information to undertake a detailed time series analysis on hail variations for the years 1989-2009. While the annual frequency did not change over the years, the observed intensity increased by 70%. Due to a bi-modal monthly distribution of hail with maximums appearing in May and July, it was concluded that at least two different major meteorological flow events are responsible for hail origination in this area. Furthermore, a relationship between the increase of hail intensity and minimum surface temperature was observed, pointing to a possible influence of global warming.

Besides the southwest of France, Spain is one of the most affected countries by severe hail. One of the most threatened area is the Ebro Valley in the Northeast. García-Ortega et al. (2014) investigated anomalies in (local) low/mid atmospheric flow conditions to gain more knowledge on the high occurence of hail days within this region. Several special synoptic configurations were compared with results showing a positive trend of temperatures at 850 hPa and geopotential height. It was concluded that the long term characteristic synoptic circulation since 1950 has changed towards a low-level thermodynamic environment which favours hailstorm origination in northeastern Spain.

Sánchez et al. (2013) used both C-and S band radar data in combination with hailpad information in the province of Zaragoza (NE Spain) and Mendoza (Argentina) to investigate the relationship of kinetic energy of hail and several observed radar variables. A logistic regression approach was used to gain a deeper understanding of this relationship. Kinetic energy information was split in two groups, namely low energy (< 20 jm^{-2}) and high energy (> 20 Jm^{-2}). High uncertainties were observed for C-band radar. Contrary, S-band radar results showed a detection probability of (non)-severe hail of 85.7% with an explained model variance of 61.2%. To be able to link the statistical retrieved results to meteorological effects, a Principal Component Analysis (PCA) was undertaken previously by the authors.

While some studies in Europe (Berthet et al., 2011; Dessens, 1995) proposed a relation between summer mean temperature and hail severity (derived from hail-related parameters for insurance processes), american studies (Changnon & Changnon, 2000) concluded that a significant correlation between these two variables is not feasible seen on the high variance of worldwide climate. On this base, Saa Requejo et al. (2011) investigated 47 Spanish provinces with all kind of different environmental settings. Crop insurance data from 1981 to 2007 was utilized. The authors could not find a relation between hail damage and mean minimum temperature. This finding, and the relationship of temperature and hail severity in general, is intensively discussed in this work.

APPENDIX C

THE TORRO HAILSTORM INTENSITY SCALE

Table C.1.: The TORRO hailstorm intensity scale, adapted from J. Webb et al. (1986)

H - Scale Number	Diameter (cm)	Hailstone size description (largest)	Effects
0	0.5 - 1	Pea	True hail of pea size but no damage
1	0.5 - 2	Mothball, bean, hazelnut	Leaves holed, flowers damaged
2	0.5 - 3	Large marble, large grape, walnut	Leaves stripped from trees and plants, vegetables shredded, fruit and crops bruised and scarred
3	1.1 - 4.5	Chestnut, pigeon´s egg, table-tennis ball, golf ball, squash ball	Some panes in glasshouses/skylights broken, wood (fences) scroed, Caravan bodywork dented, Canvas and perspex holed, Stems of crops severed, seeds threshed
4	1.6 - 6	Hen´s egg, small peach, small apple	Some house windows, vehicle windscreens broken, glasshouses shattered, some felt roofs pierced, paint scaped off walls, small branches broken from trees, ground pitted, unprotected birds ands poultry killed
5	2.1 - 8	Large peach, large apple, small-medium orange, tennis ball, cricket ball, baseball	Some roof tiles/slates broken, many windows smashed, plate-glass roofs broken, brick walls pitted, car bodywork visibly dented, strips of bark torn from trees, large branches broken down, risk of serious or fatal injuries to small animals
6	3.1 - 10	Large orange, grapefruit	Plate/reinforced glass windows, mant roof tiles/slates broken, concrete walls/pavements pitted, corrugated iron and some other metal roofs holed, light aircraft damaged
7	4.6 - 12.5	Melon	Roofs severly cut up, windows frames carried away, bodywork of cars and light aircrafts severely damaged, ground deeply indented and scoured
8	6.1 - > 12.5	Coconut, etc.	Bodywork of cars and light aircraft destroyed, severe damage to commerical aircraft small tree-trunks split apart, risk of serious injury to persons out in the open
9	8.1 - > 12.5	Coconut, etc.	Large tree-trunks brought down, severe structural damage to most buildings, some homes (e.g. mobile homes) destroyed, risk of fatal injury to persons caught in the open
10	10.1 - > 12.5	Coconut, etc.	Wooden houses destroyed, brickhouses and concrete sturctures very severely damaged, extreme danger to persons without special protection